The Dissertation Committee for Kyle Nicholas Knust certifies that this is the approved version of the following dissertation:

Bipolar Electrochemistry for Enrichment, Separations, and Membraneless Electrochemically Mediated Desalination

Committee:

Richard M. Crooks, Supervisor

Jason B. Shear

C. Buddie Mullins

Lauren J. Webb

Keith J. Stevenson

Bipolar Electrochemistry for Enrichment, Separations, and Membraneless Electrochemically Mediated Desalination

by

Kyle Nicholas Knust, B.S.

Dissertation

Presented to the Faculty of the Graduate School of

The University of Texas at Austin

in Partial Fulfillment

of the Requirements

for the Degree of

Doctor of Philosophy

The University of Texas at Austin

August, 2015

Dedication

To Kenny and Gail,

Alyse,

and family

Acknowledgements

I thank my parents, Kenny and Gail, for without their unconditional support, I would not have pursued my interest in science. I thank my wife, Alyse, for her support and ability to provide the balance necessary to accomplish my goals.

I thank the often overlooked supporters of my research endeavors, UT Austin staff, especially Angie Missildine and Tim Hooper, for their assistance.

I thank my previous research colleagues, particularly Matt Foley and Dennis Peters for instilling the foundation to my scientific and professional future.

I thank the Crooks Group, past and present, for their continued camaraderie and support. Special thanks to Eoin Sheridan and Robbyn Anand for their invaluable instruction and mentoring.

Finally, I would like to thank my research advisor, Prof. Richard M. Crooks, for the opportunity to explore science both in the lab and away from the bench at conferences. Through your guidance, I have improved as a communicator, thinker, and scientist.

Bipolar Electrochemistry for Enrichment, Separations, and Membraneless Electrochemically Mediated Desalination

Kyle Nicholas Knust, Ph.D.

The University of Texas at Austin, 2015

Supervisor: Richard M. Crooks

Developments in bipolar electrochemistry for the simultaneous separation and enrichment of charged species and membraneless electrochemically mediated desalination (EMD) are presented. Each of these techniques requires an electrochemically generated local electric field within a microchannel and control over bulk fluid flow. In addition to bipolar electrochemical studies, investigations of ion depletion zone formation and EMD in a two-electrode microelectrochemical cell are presented.

The dual-channel bipolar electrode (BPE) configuration is employed for the simultaneous enrichment and separation of anions and cations within a single microchannel at an ion depletion zone generated by buffer neutralization. Moreover, this experimental design is also used to generate an ion depletion zone and associated electric field gradient by Cl^-

oxidation, where we demonstrate partial seawater desalination without the need for a physical membrane.

Expanding upon the fundamentals of BPE focusing, we demonstrate proof-of-concept biomolecule separation and enrichment. Moreover, without the need for a direct external electrical connection, one hundred BPEs are operated simultaneously in parallel to enrich multiple analyte bands. Metal deposition at a BPE is used to mediate BPE focusing.

Ion depletion zones arising from Cl^- oxidation are investigated by making axial electric field measurements while varying key experimental parameters affecting ion depletion zone formation, location, and strength. We investigate the capabilities of EMD by modifying the electrode design to increase the local electric field strength in an effort to increase the percentage of salt rejection. We also examine the possibility to lower, or even eliminate the electrical energy requirements of EMD by driving Cl^- oxidation photoelectrochemically. Lastly, on-line capacitively coupled contactless conductivity measurements are presented to rapidly and reliably quantify ion separation for EMD.

Table of Contents

List of Tables

List of Figures

List of Illustrations

Chapter 1: Introduction

Bipolar Electrochemistry

Fundamentals

A bipolar electrode (BPE) is a conductive material that simultaneously drives oxidations and reductions without requiring a direct electrical connection to a power source.[1-3] Scheme 1.1 depicts the simplest configuration for a BPE experiment. In this example, a BPE is immersed in electrolyte solution with a driving electrode on either end of the cell. When a sufficiently high potential bias is applied across the BPE embedded within the fluidic cell, simultaneous oxidations and reductions occur at the BPE poles.

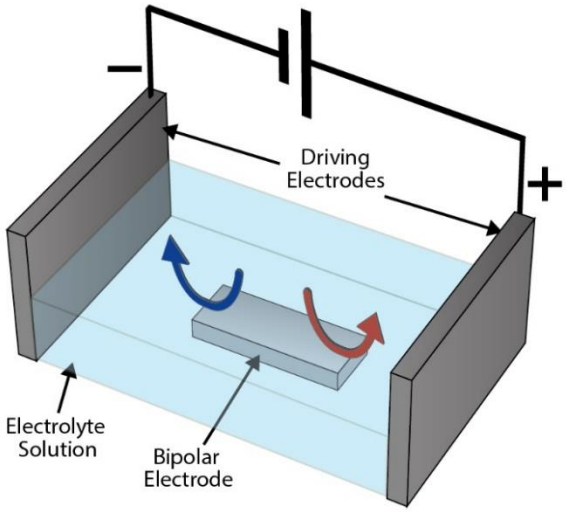

Scheme 1.1:

Schematic illustrating a simple BPE cell configuration.

Throughout this dissertation, we'll be working with BPEs embedded in microchannels, such as that depicted in Scheme 1.2a (not to scale). The microfluidic channel has a height of 2-20 µm, a width of 10-100 µm, and a length of 5-6 mm. Let us now examine in more detail the principles driving faradaic reactions at the BPE poles. A key point for understanding wireless bipolar electrochemistry is that the BPE poles are oriented in the opposite polarity of the driving electrodes (Scheme 1.2a). Potential contaminants electrogenerated at the driving electrodes do not interfere with the BPE in this design because of the macroscale channel length.

The voltage applied between the two driving electrodes (E_{tot}) results in a uniform electric field in solution that causes the BPE to float to an equilibrium potential (E_{elec}) dependent on its position in the field and the composition of the electrolyte solution (Scheme 1.2b). Because the electrode is a conductor, E_{elec} is the same (or nearly so) everywhere on its surface. However, the interfacial potential difference between the BPE and the solution varies along its length due to the presence of an electric field in solution.

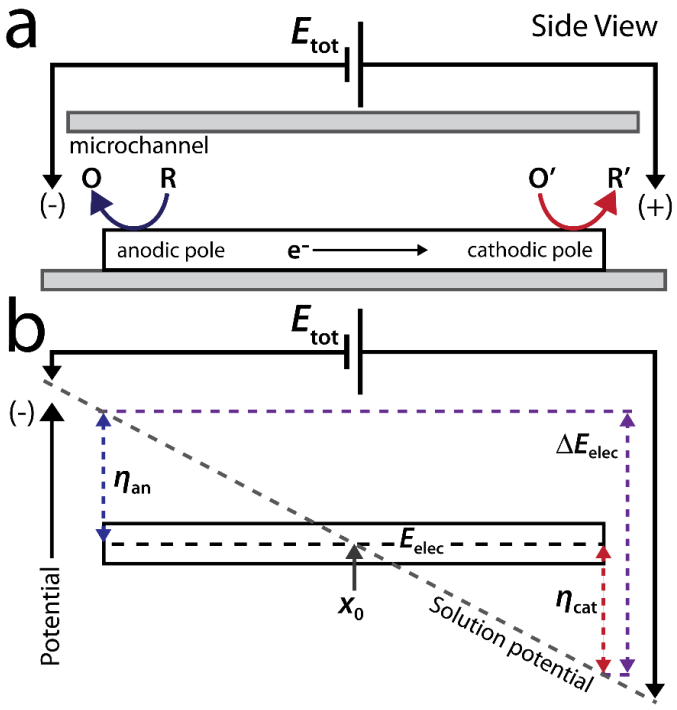

Scheme 1.2:

(a) Schematic illustrating a BPE embedded in a microchannel between two driving electrodes (not to scale). (b) The potential distribution for the cell depicted in (a).

These anodic and cathodic overpotentials,[4] η_{an} and η_{cat}, respectively, drive electrochemical reactions at the BPE poles. The interfacial potential difference between the solution and BPE is highest at the ends of the electrode, so faradaic processes are always observed there first. Scheme 1.2b shows that the magnitudes of the overpotentials depend on just two experimental variables: the magnitude of E_{tot} and the length of the BPE. Therefore, if E_{tot} is sufficiently high, faradaic electrochemical reactions result at the anodic (blue

arrow) and cathodic (red arrow) BPE poles. The location on the BPE that defines the boundary between its two poles, and therefore itself has zero overpotential with respect to the solution, is defined as x_0. Although x_0 is represented as being at the center of the BPE in Scheme 1.2b, its actual location depends on the nature of the faradaic processes occurring at the poles.[4]

While the magnitudes of the overpotentials vary along the length of a BPE, conversely, the working electrode in a traditional three-electrode cell configuration has a uniform interfacial potential difference (although this depends on how the cell is designed, the placement of the three electrodes relative to one another, and the resistivity of the electrolyte solution).[5] In either case, however, it is this interfacial potential difference that drives electrochemical reactions.[6] Importantly, the non-uniformity of the interfacial potential differences along the length of a BPE can be beneficial for certain applications.

Modifying the Electric Field and Current Paths

The nature of the electric field formed between the driving electrodes in a bipolar electrochemical experiment depends on the cell geometry and the conductivity of the electrolyte solution. As previously described, a linear electric field is generated by restricting the cross-

sectional area of the solution between the driving electrodes, thereby increasing its resistance. This can be achieved by embedding the BPE in a microchannel having a small cross-sectional area (e.g., Scheme 1.2a).

The parameters affecting a BPE experiment include E_{tot}, the distance separating the driving electrodes, $l_{channel}$, and the length of the BPE, l_{elec}. The fraction of E_{tot} that is dropped over a BPE, which we refer to as ΔE_{elec}, can be estimated using eq 1.1.[1,6,7]

$$\Delta E_{elec} = E_{tot}\left(\frac{l_{elec}}{l_{channel}}\right) \quad (1.1)$$

The value of ΔE_{elec} is a critical parameter for analyzing electrochemical processes at BPEs. The simple relationship expressed in eq 1.1 incorporates a number of assumptions that may be possible to ignore for a particular system, but not others. For example, it assumes that an active BPE does not significantly affect the electric field in the solution, which is often not the case.

The aforementioned point can be understood in terms of the equivalent circuits shown in Scheme 1.3, which are reasonable approximations of the resistances present in the type of cell shown in Scheme 1.2a. In the absence of a BPE, the current flowing between the driving electrodes is entirely ionic (Scheme 1.3a).[8] The magnitude of the ionic

current moving through the electrolyte is then governed by the magnitude of the applied potential (E_{tot}) and the resistance of the solution (R_S). When faradaic reactions occur at a BPE, a second path for current, in the form of electrons moving through the BPE, is available (Scheme 1.3b).

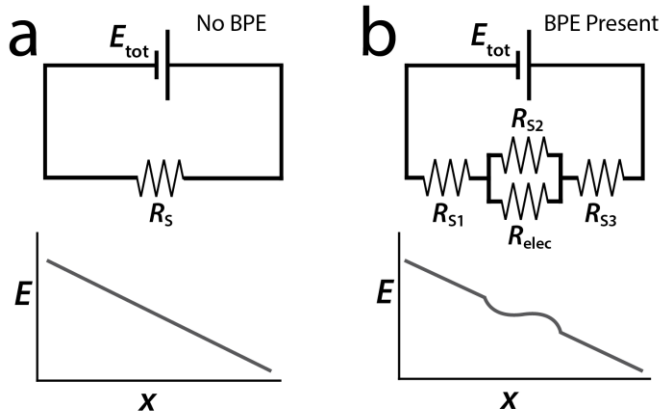

Scheme 1.3:

Equivalent circuit diagrams and potential (E) vs distance plots of an electrolyte filled microchannel with a potential bias applied across the channel without (a) and with (b) an embedded BPE.

We now define the parameter R_{elec}, which is the total resistance to electronic current posed by the BPE, hence, incorporating the charge transfer resistance (R_{ct})[8] and relevant aspects of mass transfer. If the resistance of the solution above the BPE (R_{S2}) is much lower than R_{elec}, then most of the current in the cell passes through the solution rather than the BPE. In this case, the electric field is not

significantly perturbed by the BPE. However, when $R_{S2} > R_{elec}$, which can be achieved by lowering the electrolyte concentration, substantial current flows through the BPE. This alters the local electric field in solution, which is proportional to $I_{tot}R_{S2}$ (I_{tot} is the total current flowing in the cell), thus resulting in a nonlinear electric field in the solution above the BPE. This effect is called faradaic depolarization, and its magnitude depends on the strength of the electric field, the concentration of the supporting electrolyte, and the electrochemical properties of the electroactive species in the system.[9-13] It is also important to note that eq 1.1 does not account for any potential dropping at the driving electrodes. The fractional loss of E_{tot} within the electrochemical double layers can, under some circumstances, be substantial.[4]

BPE Configurations

Thus far, we have focused on open BPEs, where current can flow through both the electrolyte and the BPE. These types of devices are defined by the existence of two possible current paths: electronic and ionic. However, as will be discussed throughout this dissertation, there are several interesting uses for closed BPEs (Scheme 1.4a).[14-16] In a closed BPE system, the solutions contacting the BPE anode and cathode are physically separated from one another, and

therefore the only current path between the two half cells is through the BPE (Scheme 1.4b).

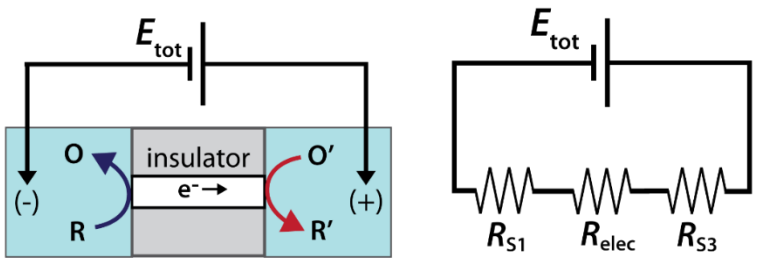

Scheme 1.4:

(a) Schematic illustrating a closed BPE with poles in contact with two physically separated electrolyte solutions. (b) Equivalent circuit diagram for a closed BPE system.

Applications

With this fundamental background, we now turn to a discussion of several interesting applications of bipolar electrochemistry. BPEs have found numerous applications because they do not require a direct external electrical connection, making them well-suited for both nanoscale electrochemistry applications, where it might be difficult to make such a connection, and for high-density electrode array applications, where it would be impractical to make thousands or millions of individual electrode connections.

BPEs were first employed in the 1960s as fluidized bed electrodes, where a voltage applied between two driving electrodes enabled electrochemical reactions at discrete conductive particles.[17-22] Since these early studies, bipolar

fluidized bed electrodes have been used in applications ranging from improving the efficiency of electrosynthesis,[23-25] to photoelectrochemical cells,[26,27] and even batteries.[28] Bipolar plate technology, where the plates form a series of BPEs, is critical for polymeric-electrolyte-membrane (PEM) fuel cells.[29,30] Closed BPEs are commonly used in bioelectrochemical applications.[31,32] Bipolar electrochemistry has also been utilized for logic gates.[33] More recently, bipolar electrochemical reactions have been shown to induce motion of microscale BPEs by propulsion through the electrochemical generation of H_2 or O_2 bubbles.[34-37] Compositional gradients of chemicals (e.g. SAMs), polymers, and metals have been synthesized on BPEs by taking advantage of the interfacial potential differences along the length of a BPE.[38-42] BPE arrays have been employed for electrocatalyst screening[43-45] and a variety of sensing applications, including chemical[46-48] and DNA sensors.[49-51]

BPE Focusing And Separation

Principles of BPE Focusing

While the principles of bipolar electrochemistry have been employed for numerous applications, in this dissertation, we'll focus on their use for charged analyte enrichment and separations. Due to small sample volumes and

low absolute numbers of molecules present within microfluidic devices, the detection of analytes in such systems often requires a preconcentration step prior to analysis. Our group, together with our collaborators, Dr. Ulrich Tallarek and Dr. Dzmitry Hlushkou from Philipps-Universität Marburg, have shown BPEs can be employed to address this issue by enriching charged analytes along a locally generated electric field gradient.[52] We call this method BPE focusing, and it is a member of a family of analyte enrichment techniques based on the principle of electrokinetic equilibrium. More specifically, BPE focusing is a counter-flow gradient focusing[53] (CFGF) technique in which charged analytes enrich when electromigration (EM) is balanced against bulk fluid flow.

The key to this technique involves generation of a local electric field gradient near a BPE. With a sufficiently high E_{tot} applied across a microchannel having an embedded BPE (Scheme 1.5a), water electrolysis may proceed at the BPE poles following eqs 1.2 and 1.3, respectively.

(1.2) $2H_2O + 2e^- \leftrightarrow H_2 + 2OH^-$

(1.3) $2H_2O - 4e^- \leftrightarrow O_2 + 4H^+$

(1.4) $TrisH^+ + OH^- \leftrightarrow Tris + H_2O$

For anionic enrichment, electrogenerated OH^- at the BPE cathode may neutralize a positively charged buffer, such as protonated tris(hydroxymethyl)aminomethane ($TrisH^+$) (eq 1.4), thereby forming an ion depletion zone near the BPE (Scheme 1.5b). The increased solution resistivity within the ion depletion zone causes a large proportion of E_{tot} to be dropped in this region, thus causing an increase in the local electric field strength. It is this electric field gradient that allows the local enrichment of charged analyte in the presence of a counter-flow. Other groups have reported the use of BPEs for enrichment by either generating pH gradients or non-uniform EOF.[54,55]

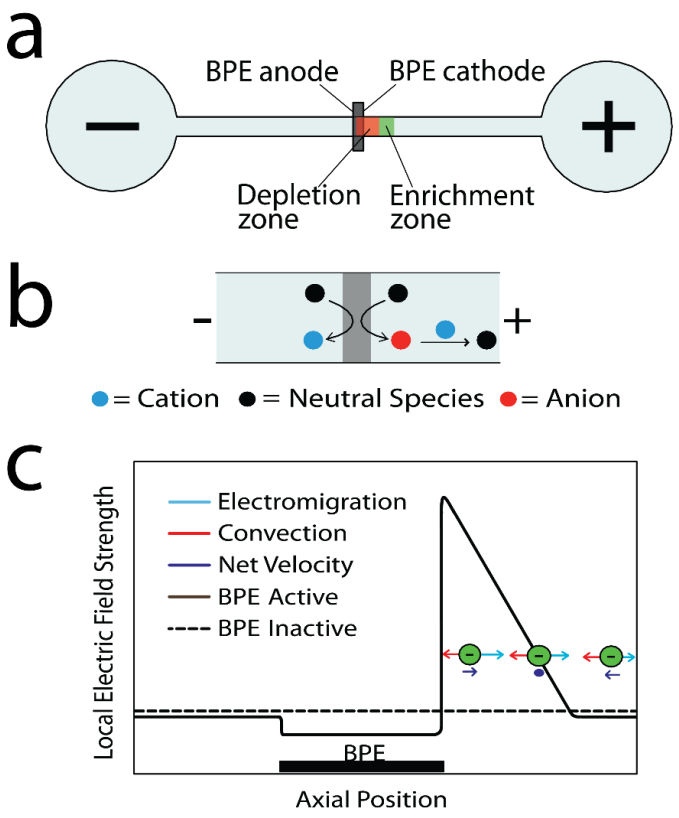

Scheme 1.5:

(a) Schematic illustrating the location of an ion depletion and enrichment zone near a BPE embedded in a microchannel. (b) Schematic depicting water electrolysis at a BPE and the subsequent formation of an ion depletion zone by cationic buffer neutralization. (c) The local electric field strength vs distance near a BPE embedded in a microchannel showing anion enrichment *via* a CFGF mechanism.

Electrokinetics and Mass Transport

The transport of charged analytes during a BPE focusing experiment is controlled by bulk fluid flow (electroosmotic flow, EOF + pressured driven flow, PDF) and EM. A cathodic EOF develops when a potential bias is applied across the negatively charged walls of a polydimethylsiloxane (PDMS) /

glass microchannel. In addition to EOF, bulk solution flow can be controlled by PDF, which is initiated by creating a solution height differential in the reservoirs at the channel ends by simply adding or removing solution.

When exposed to an electric field, charged analytes undergo EM toward the oppositely charged driving electrode. The electrophoretic velocity (u_{ep}) of a charged analyte in an electric field is dictated by eq 1.5, where μ_{ep} is the electrophoretic mobility and V_l is the local electric field strength.

$$u_{ep} = \mu_{ep} V_l \tag{1.5}$$

$$\mu_{ep} = \frac{DZ}{k_B T} \tag{1.6}$$

The μ_{ep} of an analyte is set by eq 1.6, where D is the diffusion coefficient, Z is the charge, k_B is the Boltzmann constant, and T is the absolute temperature. Consequently, ions with a higher diffusion coefficient and charge have a larger u_{ep} and therefore migrate more quickly at any given V_l.

As anions enter the microchannel and approach the BPE, they experience an increasing u_{ep} as the V_l increases. Enrichment occurs when u_{ep} and bulk flow are equal in magnitude and opposite in direction (Scheme 1.5c). Because the location of enrichment depends on μ_{ep} (eq 1.6), analytes having different μ_{ep} may be simultaneously separated and enriched at

unique locations in the channel. Figure 1.1a shows the separation and enrichment of three negatively charged tracers having different μ_{ep} as a plot of enrichment factor (EF, ratio of the concentration in the enriched band to the initial concentration) vs distance from the BPE.

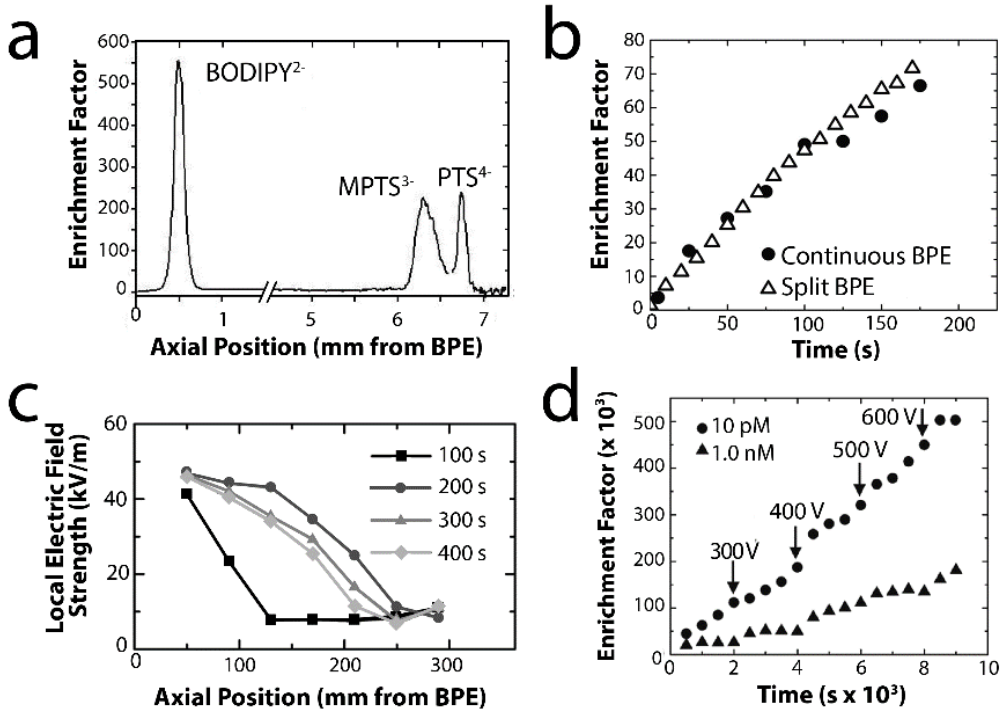

Figure 1.1:

(a) Plot of EF vs axial distance from the BPE cathode showing the enrichment and separation of $BODIPY^{2-}$, $MPTS^{3-}$, and PTS^{4-} in 5.0 mM $TrisH^+$ with E_{tot} = 40.0 V in a 12 mm-long, Pluronic-coated channel. (b) Comparison of the EF as a function of time for $BODIPY^{2-}$ at split and continuous BPEs with E_{tot} = 35.0 V in 5.0 mM $TrisH^+$. (c) Experimentally determined local axial electric field strength as a function of position and time with E_{tot} = 35.0 V in 5.0 mM $TrisH^+$. (d) Plot of EF vs time for 10.0 pM (circles) and 1.0 nM (triangles) $BODIPY^{2-}$ in pH 8.1, 100 mM $TrisH^+$. Initially, E_{tot} = 200 V, but it was periodically raised at the indicated times.

Guidelines for Enrichment

The formation and stability of the electric field gradient near a BPE has been investigated in several fundamental studies. For example, we measured the current flowing through a split BPE (two microbands connected externally *via* a jumper wire) to show that a significant change to the local electric field gradient results only after a large percentage (~80%) of the total current passes through the BPE.[56] In other words, only when there is a significant degree of faradaic depolarization is a locally enhanced electric field observed. There are three additional aspects of BPE focusing worth mentioning. First, split and continuous BPEs lead to local electric fields having similar characteristics, and hence result in the same degree of enrichment (Figure 1.1b).[56] Second, an array of microband electrodes embedded within a microchannel can be used to directly measure the axial electric field, and this type of experiment (Figure 1.1c) confirms the shape of the local electric field illustrated in Scheme 1.5c. Third, the electric field gradient has been shown to be stable for > 2.5 h.[57,58]

To better understand the interplay between forces necessary for BPE focusing, our collaborators have performed simulations[52,56,57,59-61] to aid in optimizing the extent and rate of enrichment. As a general guiding principle, steeper

electric field gradients lead to more compact and highly enriched bands, although shallower gradients are better for separating mixtures of charged analytes. Steeper gradients are achieved by using higher ionic strength buffers because this leads to a larger difference in electrolyte concentration between the ion depletion zone and the bulk concentration of the buffer. As discussed earlier, however, lowering R_S decreases the current flowing through the BPE, which adversely affects the ion depletion zone. Moreover, high ionic strength buffers result in higher current densities at the BPE poles and gas bubble production, which is detrimental to enrichment. Fortunately, this seeming contradiction can be resolved by reducing the cross-sectional area of the fluidic channel.[58] The bottom line is that high buffer concentrations and small cross-sectional areas lead to EFs of >500,000 (Figure 1.1d).[58]

Interestingly, lower initial analyte concentrations typically lead to higher EFs. This is because enrichment of the analyte occurs within the ion depletion layer, and because the analyte itself is a charge carrier, it increases the local conductivity of the solution. As the concentration of the enriched band approaches that of the background buffer, enrichment ceases.[59]

Although many analytical methods have been described in the literature for enriching anions, far fewer are available

for cations. This is because cationic enrichment often requires an anodic EOF. BPE focusing can be adapted to enrich cations by coating the microchannel walls with a positively charged polymer, thereby reversing the direction of EOF from cathodic to anodic.[62] In addition, the positively charged buffer used for anion enrichment must be replaced with one that is negatively charged such as HCO_3^-. The latter is neutralized by H^+ produced at the BPE anode, and therefore enrichment of cations occurs at the anodic pole of the BPE, rather than at the cathodic pole.[62]

Dual-Channel BPE Focusing

Thus far, we have only discussed BPE focusing studies in which the BPE is embedded within a single channel (Scheme 1.5a). However, we have shown that there are some compelling reasons to consider the dual-channel configuration illustrated in Scheme 1.6a.[58,63] The basic operating principles of the dual-channel approach are analogous to those of a single-channel device. Specifically, ΔE_{elec} must exceed the potential required for water oxidation and reduction. If this condition is met, water oxidation (eq 1.3) will lead to H^+ formation at the anodic BPE pole in the bottom channel, while water reduction (eq 1.2) generates OH^- at the cathodic pole in the top channel. If an appropriately charged buffer capable of being neutralized by the products of water

electrolysis is placed in either channel, an ion depletion zone and electric field gradient results. For example, in the top channel, $TrisH^+$ may be neutralized by OH^-, or, in the bottom channel, acetate buffer may be neutralized by H^+ (Scheme 1.6b) to produce an electric field gradient that is suitable for enrichment.

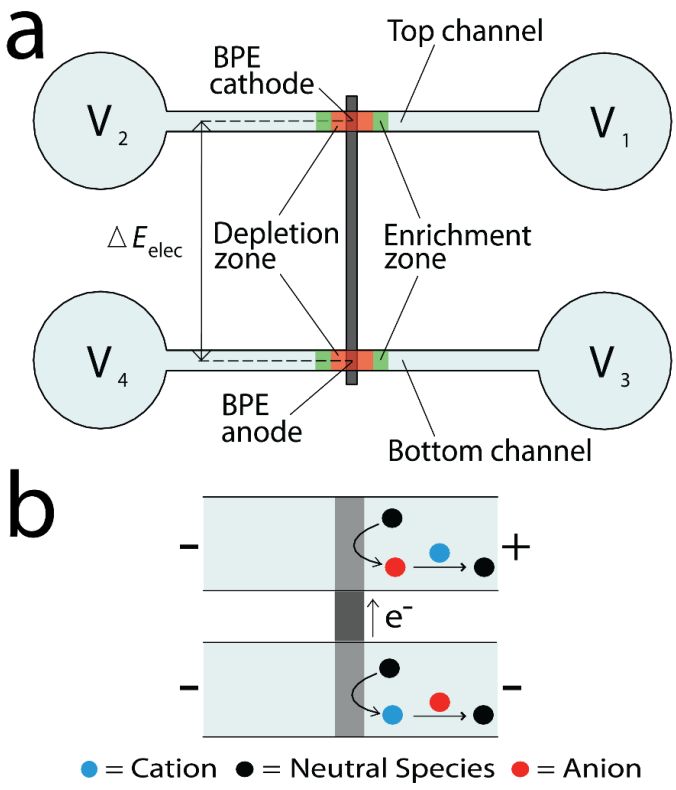

Scheme 1.6:

(a) Schematic illustrating the location of two possible ion depletion and four enrichment zones near the poles of a BPE electrically connecting two microchannels. (b) Schematic depicting water electrolysis and the subsequent formation of two ion depletion zones by buffer neutralization near a BPE in a dual-channel configuration.

Using the dual-channel device, we have achieved EFs of up to 142,000-fold at rates as high as 71 fold/s. These excellent figures of merit are achievable because this configuration decouples E_{tot} and ΔE_{elec}. This means higher values of E_{tot} may be applied without generating gas bubbles at the BPE. Moreover, higher E_{tot} values increase the rate at which the analyte is transported from the channel reservoirs to the enrichment zone, while simultaneously steepening the local electric field gradient. As discussed previously, the latter situation leads to a narrower and more highly enriched analyte band. As will be discussed in more detail in Chapter 2, a combination of interesting electric field gradients and mass transport conditions can be achieved using the dual-channel configuration to simultaneously separate and enrich anions and cations present in the same channel.

BPE Focusing Applications

Beyond enrichment and separation, we have also shown manipulating the V_1 with a BPE is useful for a variety of other applications.[64] For example, we have shown charged buffer electrolytes can be replaced with KCl to form an asymmetric electric field when faradaic reactions at a BPE result in a redistribution of ions. In this case, a strong ion depletion zone no longer forms, but rather an asymmetric electric field gradient results. This unique electric field

profile allows for depletion and membraneless filtration of charged analytes from neutral analytes.

The local electric field gradient can be used to concentrate and direct the flow of charged analytes.[65] As previously discussed, enrichment occurs when EM balances convection. This means that the forward movement of an analyte ceases when its u_{ep} is greater than or equal to the opposing convective velocity. Using these principles, we have demonstrated the controlled transport and selective delivery of two charged analytes by employing a microfluidic design having two microband BPEs embedded near the split of a Y-shaped microchannel (Scheme 1.7). In this configuration, the BPEs act as on/off switches for an electric field gradient. Specifically, when both BPEs are activated using an external switch, the V_1 is high and analytes enrich and separate in the main channel (Scheme 1.7) as discussed earlier in the context of Figure 1.1a. Then, when one BPE is disconnected and the PDF is increased from right to left (Scheme 1.7b), both enriched bands move toward the intersection. By carefully controlling when the gating BPEs are active, the anionic fluorescent tracer closest to the intersection (green ball) is delivered into the lower secondary channel. This occurs because the V_1 in this region of the channel has been lowered, leading to a lower u_{ep} and the dominance of PDF. After this delivery, the first BPE is reconnected and the

second is disconnected, thus allowing the other fluorescent tracer (blue ball), to be delivered into the upper secondary channel by PDF (Scheme 1.7c). Finally, we have recently shown that a dual-channel BPE configuration can be used to partially desalinate seawater using the separation principles presented.[66] These results will be discussed in greater detail in Chapter 4.

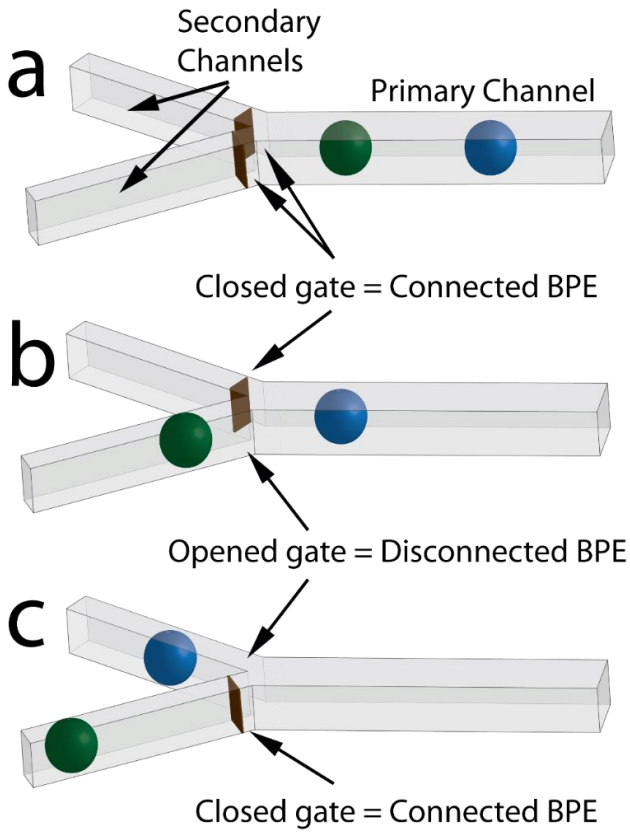

Scheme 1.7:

(a-c) Schematic illustrating the enrichment and permanent separation of two charged analytes near two BPEs and a bifurcated microchannel.

Desalination

Fresh water is required to sustain life. However, the world is facing a global challenge to reliably supply its population with safe water due to shortages stemming from population growth,[67] climate change,[68] contamination of available fresh water supplies,[69] and public policy.[70,71] Presently, the United Nations estimates one-third of the world's population (~2.4 billion people) is living in water stressed regions,[72] meaning the annual water supply is <1,700 m^3 per person.[73] Even more alarming, this number is expected to approach two-thirds of the world's population by 2025. Water shortages are not just limited to those living in arid or developing regions; the effects are now being acutely felt by those living in fresh water-rich environments.[71]

Increasing the availability of fresh water is a complex problem that does not have one simple solution. Consequently, technological developments providing a synergy of solutions will likely be required to address the world's water challenges. The first step toward ensuring water for all is the efficient use and conservation of currently available fresh water supplies. Encouragingly, there are examples in the developed world of per-capita water use decreasing due to more efficient agricultural, industrial, and personal practices.[74] Nevertheless, similar to petroleum reserves, continued economic development of populous countries like

China and India will exert new stresses on world-wide water resources.[75]

The available amount of water on Earth is relatively constant due to the hydrological cycle.[76] However, supplies vary with time and location, therefore making localized water shortages commonplace. Table 1.1 shows that only ~2.5% of water available on Earth is fresh water (<0.05% salts by weight).[77] Of this amount, more than half is locked in glaciers and permanent ice, while remaining supplies are increasingly being contaminated with difficult-to-remove impurities.[78,79] Importantly, ~97.5% of the world's water supply is contained in easily accessible saline reservoirs, with ~1.0% being brackish groundwater (0.05-3.0% salts) and the remaining ~96.5% being seawater (3.0-5.0% salts). This suggests that the vast amounts of saline water could provide a nearly unlimited fresh water supply if coupled to an energy-efficient desalination technology.

Global Water Distribution

Source	Volume (10^{15} m^3)	Percentage
Oceans	1338.0	96.5
Glaciers / permanent snow	24.1	1.74
Saline groundwater	12.9	0.94
Fresh groundwater	10.5	0.76
Ground ice / permafrost	0.3	0.022
Freshwater lakes	0.091	0.007
Saline lakes	0.085	0.006
Rivers / swamps / other	0.015	0.001
Atmosphere	0.013	0.001

Table 1.1:

Table showing estimates for the global distribution of water adapted from reference 77.

Desalination and Energy

Beyond sustaining life, water pervades many other facets of human life: agriculture, industry, and personal wellness; however, no sector is more interdependent with water than energy.[80-82] With the exception of some renewable forms of energy, including solar and wind, most energy sources require water for production. For example, hydraulic fracturing,[83,84] often known as fracking, a relatively new technology for extracting hydrocarbons, not only requires vast amounts of desalted water, but, reports also suggest waste effluents contaminate existing drinking water reservoirs.[85] Likewise, the production of clean, fresh water, whether by desalination or other means, is an energy-intensive process. For example, each of the five main components of desalination: intake,

pre-treatment, separation, post-treatment, and concentrate discharge, has an associated energy requirement. Furthermore, the transport and distribution of desalted water requires energy.

The minimum energy required to drive the separation of salt and water during the desalination process is dictated by the second law of thermodynamics.[86,87] Importantly, this minimum energy requirement is independent of the process or pathway employed for desalination. The theoretical minimum energy is dependent upon the feed water salinity, amount of salt rejection, percent recovery of desalted water, and temperature. Percent recovery is defined as the percentage of desalted water produced relative to the quantity of feed water.

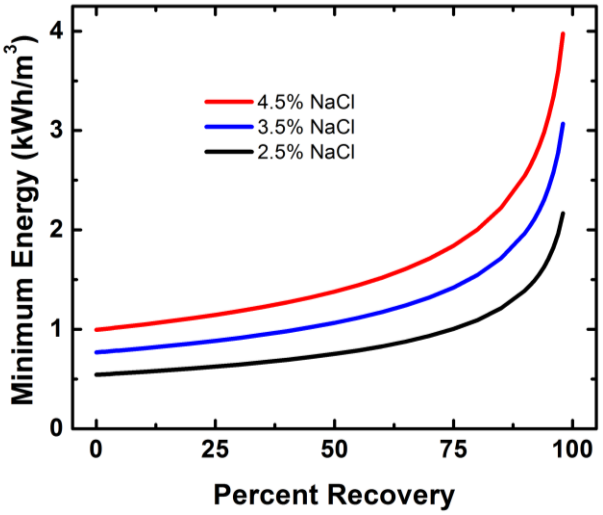

Figure 1.2:

Plot of the theoretical minimum energy required to fully desalinate water (containing the indicated percentages of NaCl) vs the percentage of fresh water recovered.

Figure 1.2 is a plot of the theoretical minimum energy required to fully desalinate water (containing the indicated percentages of NaCl) vs the percentage of fresh water recovered.[86,87] The average seawater on Earth contains 3.5% (35 g/L) salts.[88] The theoretical minimum energy required to produce completely desalted water from a 3.5% NaCl feed at 50% recovery is ~1 kWh/m^3 (Figure 1.2). Several important trends are represented in Figure 1.2. First, more complete salt removal increases the energy demand. Therefore, feed waters with higher salt concentrations will have higher energy requirements for a given percent recovery. Second, increasing the percent recovery, and hence the total salt

rejection, raises the energy requirements. As 100% recovery is approached, the minimum energy required for separation increases exponentially. Consequently, most desalination techniques operate near 50% recovery. Finally, if less than 100% salt rejection is required, the theoretical energy for desalination is lower than the values plotted in Figure 1.2.

Due to differences in infrastructure, feed water, and the required extent of desalination, it is difficult to directly compare desalination techniques. However, the separation process of all desalination strategies can be compared by dividing the actual operating energy efficiency by the theoretical minimum energy needed for the given separation process. Even with this figure of merit, however, there still may be considerable differences in intake, pre-treatment, post-treatment, and concentrate discharge requirements that are excluded from the fundamental efficiency calculation.

Thermal Desalination

The first widely used desalination technique was thermal distillation, which involves heating water until it vaporizes, thus separating the water vapor from salts left behind in the liquid phase. The vapor is then condensed and collected.[89] This basic concept, which became commercially available in the 1950s, is now employed in modern-day

multiple-effect distillation (MED), multi-stage flash distillation (MSF), and mechanical vapor compression (MVC) facilities.[90] The minimum energy required to drive thermal desalination is directly related to the heat of vaporization of water, which is substantially higher than that of other desalination techniques. Consequently, large-scale thermal desalination is limited to geographical regions, such as the Middle East, rich in the energy resources required to drive the process and poor in natural fresh water sources. Although the energy costs are high, ~13 kWh/m^3 for seawater desalination at a 45% recovery,[91] thermal desalination accounts for ~40% of desalinated water production[92] largely due to its reliability and minimal pre-treatment requirements.[93] For these reasons, thermal desalination has a role to play in addressing the world's water needs, but improvements in energy efficiency are required if the method is to remain competitive. For example, solar[91,94] and waste thermal energy from industrial processes[95] are being implemented to lower desalination costs.

Membrane Desalination

Especially in the developed world, there is a preference for desalination methods that are less energy-intensive than thermal desalination, leading to increased use of membrane-based approaches depicted in Scheme 1.8.[96] Reverse osmosis

(RO),[97] first introduced at scale in the 1960s, has become the dominant water purification technique in recent decades and now accounts for ~51% of desalinated water production.[92] RO is induced when a pressure differential greater than the osmotic pressure of the feed water is applied across a semi-permeable membrane. The minimum energy required for RO is therefore directly related to the salt concentration of the feed water. Currently, most RO facilities employ ~100 nm thick polyamide membranes on a polysulfone/fabric support. Hydrated ions are unable to penetrate through the polyamide matrix, while water molecules pass *via* a solution-diffusion mechanism.[98,99] This means water molecules first partition into the polyamide membrane, and then diffuse through due to the concentration gradient resulting from the pressure differential across the membrane.

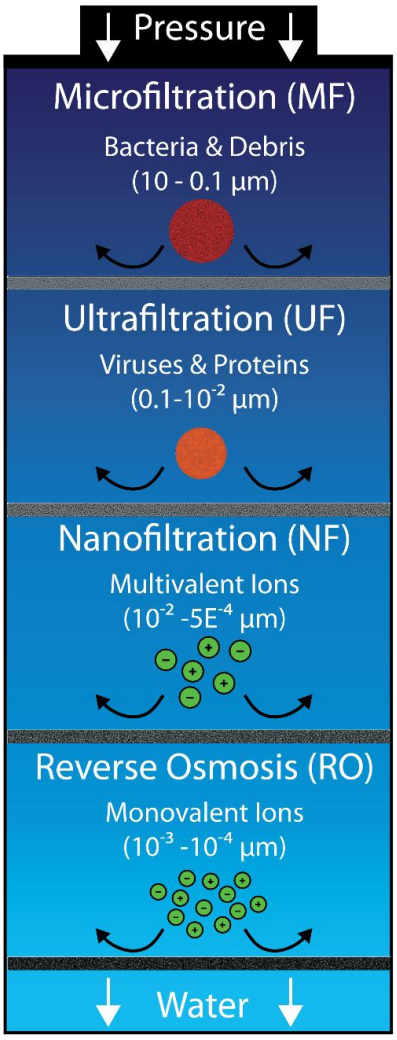

Scheme 1.8:

Schematic illustrating membrane-based separation methods and the size of particulates that are separated.

With advances in membrane technology[100] and energy recovery devices,[101] RO can operate at ~2.0 kWh/m^3 for seawater desalination at a 50% recovery, which is about twice the theoretical minimum efficiency for 100% desalination. This is the best value for any commercialized method.[87] However,

RO is now considered a mature technology with future membrane materials resulting in only incrementally better energy efficiencies. This is due to a trade-off between membrane permeability and salt rejection, meaning further increases in permeability will likely result in less salt rejection.[102] Consequently, enhancements in energy efficiency will likely not be achieved through the development of more permeable membranes, such as those based on carbon nanotubes[103] and aquaporins.[104] Even so, RO is the benchmark for comparison of all other desalination technologies.

Importantly, RO requires intensive pre-treatment of the feed seawater due to membrane fragility. These energy requirements are generally excluded from comparison with theoretical minimums. For example, costly chlorination is required to kill microorganisms that cause bio-film growth and membrane fouling, which in turn results in decreased permeability and thus higher driving pressures.[96] Unfortunately, the chlorine added for disinfection degrades the polyamide membrane so a dechlorination step is also required prior to separation. If the product water is intended for consumption, the desalted water must then be chlorinated again after desalination to ensure disinfection. Moreover, many of the pre-treatment steps required for thermal desalination, such as filtration and the addition of anti-scaling chemicals, are also required for RO to prevent

membrane fouling. Accordingly, future cost decreases for RO will largely result from reductions in pre-treatment, post-treatment, and infrastructure rather than from increased efficiency in the actual separation of salt from water. One way of achieving these goals is through the development of chlorine-resistant membranes.[105,106]

Another membrane-based technique, which relies on electrochemistry, is electrodialysis (ED).[107] Scheme 1.9 shows that ED utilizes a series of perm-selective membranes (typically hundreds) placed between an electrode pair. When a potential bias is applied, cations and anions in the feed stream migrate through a cation- or anion-selective membrane, respectively, thus leaving behind desalted water. ED is most often employed for the desalination of brackish and other lower salinity waters, because the electrical current required for ED is proportional to the amount of salt removed. Consequently, the energy requirements for ED scale directly with salt rejection. Although not practical for seawater desalination, ED is competitive and often advantageous for brackish water desalination when compared to RO. Currently, ED accounts for ~4% of desalinated water production.[92] ED requires only a moderate amount of pre-treatment and employs chlorine-resistant membranes. Moreover, membrane fouling can be prevented by reversing the electrode polarities in a process called electrodialysis reversal (EDR). As a result

of these benefits, ED/EDR has an important role to play in brackish water desalination.

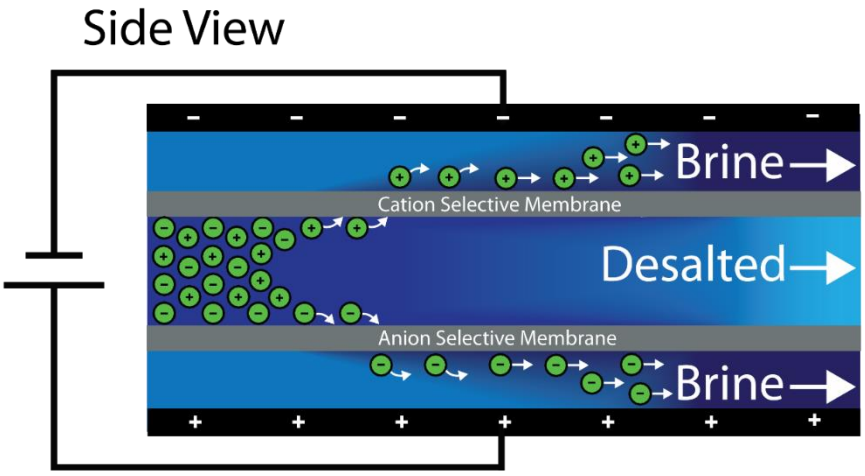

Scheme 1.9:

Schematic illustrating the operation of a pair of electrodialysis membranes under an external potential bias.

Membraneless Electrochemical Desalination

The most developed, yet still largely considered an emerging electrochemical desalination strategy, capacitive deionization (CDI), sometimes referred to as capacitive desalination, was first introduced in the 1960s.[108] The technique separates ions from water using two highly porous electrodes, such as carbon aerogels, to capacitively adsorb ions into the electrical double layer, thereby removing them from solution (Scheme 1.10). Once the ionic capacity of the electrodes saturates, the polarity is reversed to release the ions, and the cycle is repeated.[109] Because CDI is

intrinsically a batch process relying on polarity reversal, it has proven difficult to implement in a continuous process.[110] Similar to ED, the electrical current flowing during CDI is dependent on the amount of salt removal. Therefore, CDI is also more suitable for desalination of brackish water than seawater. However, because CDI is capacitive, the sequestered ions represent a source of energy. If this energy could be effectively recovered, reports suggest more concentrated salt solutions, including seawater, could be competitively desalted.[110] However, engineering a truly continuous and energy efficient CDI separation for seawater remains a challenge.

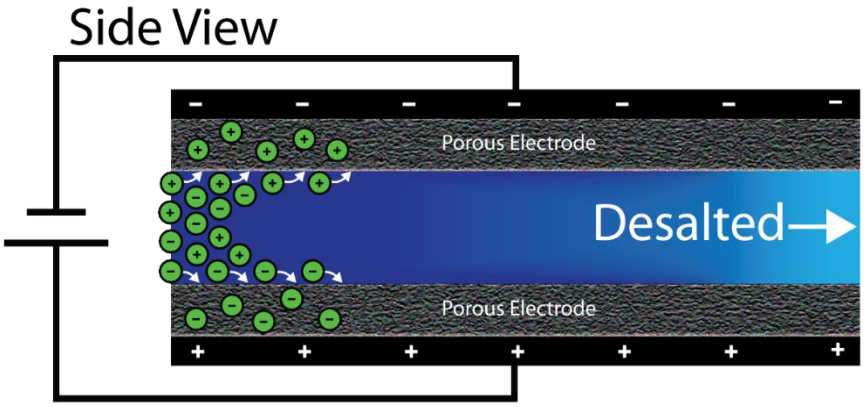

Scheme 1.10:

Schematic illustrating the operation of a capacitive deionization cell with porous membranes under an external potential bias.

Continuous separations are possible using another electrochemical desalination technique based on a phenomenon called ion concentration polarization (ICP).[111] ICP generates an ion depletion zone (region of high solution resistivity) when a potential bias applied across two fluidic channels causes a large proportion of ionic current to be carried by either anions or cations through a perm-selective material (e.g. Nafion) or a nanochannel that exhibits electrical double layer overlap. The resulting ion depletion zone creates a local conductivity gradient and electric field where ions can be directed by a combination of migration and convection. This approach was adapted to seawater desalination for a small-scale system,[112] but it was later found that the energy efficiency of the system is significantly lower than originally reported.[113] Even so, efforts are being made to increase the scale of this technology.[114]

Dissertation Overview

This dissertation examines the use of bipolar electrochemistry and an electrochemically generated local electric field within a microchannel for the enrichment and separation of charged analytes. The locally elevated electric field is initially, Chapters 2-3, generated from the products

of water electrolysis neutralizing buffer in solution, but later, Chapters 4-6, generated directly by the oxidation of Cl^-.

Chapter 2 details the use of the dual-channel BPE configuration for the simultaneous enrichment and separation of anions and cations within a single microchannel at an ion depletion zone generated by buffer neutralization. The local electric field gradient that results from these reactions is shown to have both positive and negative components, thus allowing both positive and negative ions to enrich and separate.

Chapter 3 expands upon the fundamentals of BPE focusing to demonstrate biomolecule separation and enrichment. Moreover, without the need for a direct external electrical connection, one hundred BPEs are operated simultaneously in parallel to enrich multiple analyte bands. Metal deposition at a BPE is used to mediate BPE focusing.

Chapter 4 introduces the ability to generate an ion depletion zone and concomitant electric field gradient by Cl^- oxidation. Using this elevated V_1, we demonstrate partial seawater desalination without the need for a physical membrane. Using a simple power supply in the dual-channel BPE configuration, ions are continuously separated near the ion depletion zone where their increased u_{ep} counters bulk flow such that ions are directed into a branching microchannel.

Chapter 5 investigates EMD, which relies on Cl^- oxidation to generate an ion depletion zone and elevated V_1. The V_1 is measured while varying key experimental parameters affecting ion depletion zone formation, location, and strength. We show the voltage necessary to form an elevated V_1 corresponds to the onset of Cl^- oxidation. Moreover, we establish bulk flow plays an important role in the stability and maintenance of the depletion zone. We also demonstrate the effect Cl^- concentration has on the V_1, showing elevated electric fields in brine solutions.

Chapter 6 explores the capabilities of EMD. The electrode design is modified in an effort to increase the magnitude of V_1 and percentage of salt rejection. We examine the possibility to lower, or even eliminate the electrical energy requirements of EMD by driving Cl^- oxidation photoelectrochemically. Lastly, on-line capacitively coupled contactless conductivity measurements are presented to rapidly and reliably quantify ion separation for EMD.

Chapter 2: Dual-Channel Bipolar Electrode Focusing: Simultaneous Separation and Enrichment of Both Anions and Cations

Synopsis

In this paper we show that a microelectrochemical cell comprising two parallel microchannels spanned by a single bipolar electrode can be used to simultaneously enrich and separate both anions and cations within a single microchannel. This is possible because reduction and oxidation of water at the cathodic and anodic poles of the bipolar electrode, respectively, leads to ion depletion zones. Specifically, $TrisH^+$ is neutralized by OH^- at the cathodic pole, while acetate buffer is neutralized by H^+ at the anodic pole. This action creates a local electric field gradient having both positive and negative components, hence positive and negative ions follow their respective field gradients leading to separation. In the presence of an opposing counter-flow (pressure driven flow in this case), enrichment also occurs. In addition to separation and enrichment in a single channel, it is also possible to simultaneously enrich cations in one microchannel and anions in the other. Enrichment is achieved by controlling experimental parameters, including the type of buffer and the direction and magnitude of the opposing counter-flow.

Introduction

Detection of analytes within microfluidic devices often requires a preconcentration step prior to analysis. This is a consequence of small solution volumes and low concentrations resulting in small absolute numbers of molecules. We recently introduced an electrochemical technique, bipolar electrode (BPE) focusing, to address this issue.[1,52,56,57,59-61] BPE focusing is based upon balancing convective flow, which is nearly uniform in a incompressible liquid, against electromigration (EM), which can be controlled locally along an electric field gradient. Here, we demonstrate that a dual-channel BPE focusing configuration can enrich and separate both anions and cations simultaneously. This is important, because a single platform may now be implemented for both cationic and anionic separation and enrichment.

We have previously shown that BPE focusing can separate and enrich anions in a single microchannel (Scheme 2.1).[1,52,56,57,59-61] In addition, our group has demonstrated the use of BPEs for depletion and membraneless filtration.[64] More recently, by adjusting the direction of electroosmotic flow (EOF), we have demonstrated enrichment of cations within a single-channel device.[62]

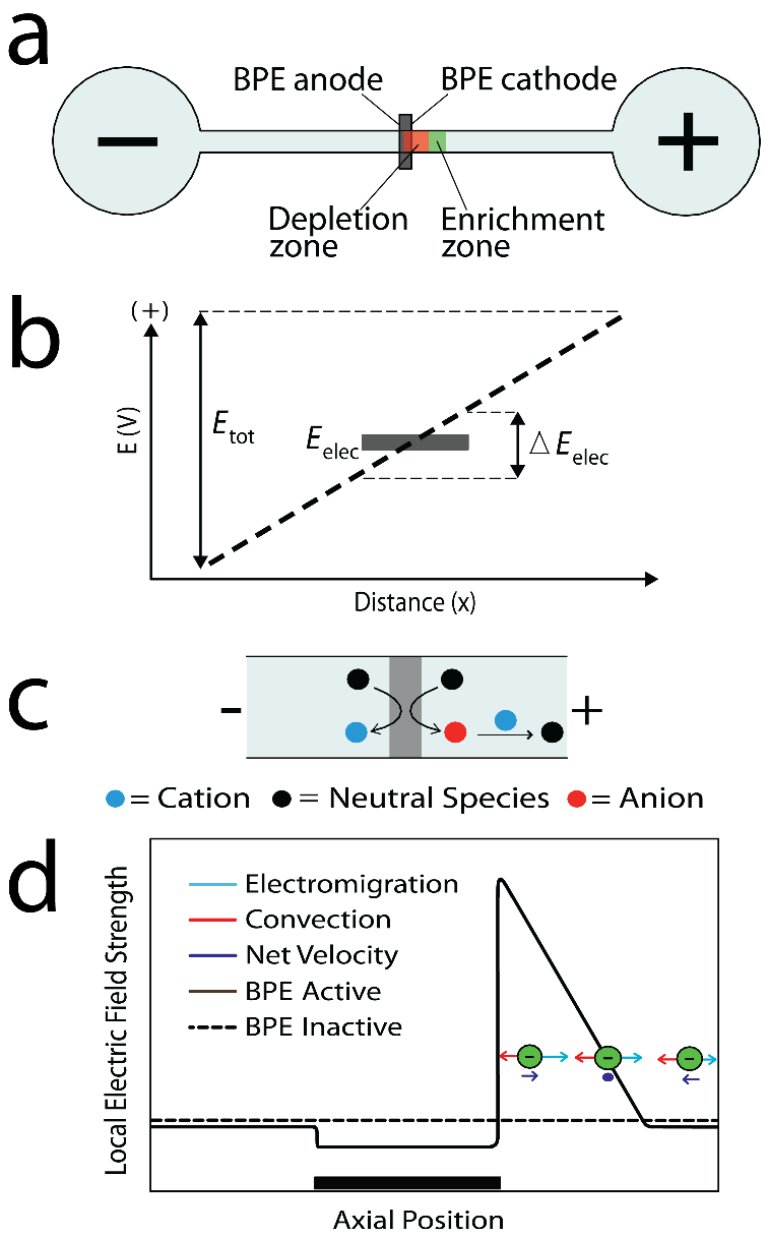

Scheme 2.1:

(a) Schematic illustrating a single channel BPE focusing device. (b) Schematic illustrating the voltage drop across the channel and BPE. (c) Schematic illustrating water electrolysis and buffer neutralization near a BPE. (d) Schematic illustrating the direction of convection, EM, and net velocity of tracer during a focusing experiment.

Analogous to our single-channel studies, we have reported a dual-channel configuration (Scheme 2.2) that has some distinct advantages for enriching anions.[58] Here, we show that this same device configuration is a versatile platform for depletion, separation, and enrichment of charged analytes. The important new result is that it enables the simultaneous enrichment and separation of a mixture of anions and cations, which was unachievable in simple, single-channel fluidic devices.

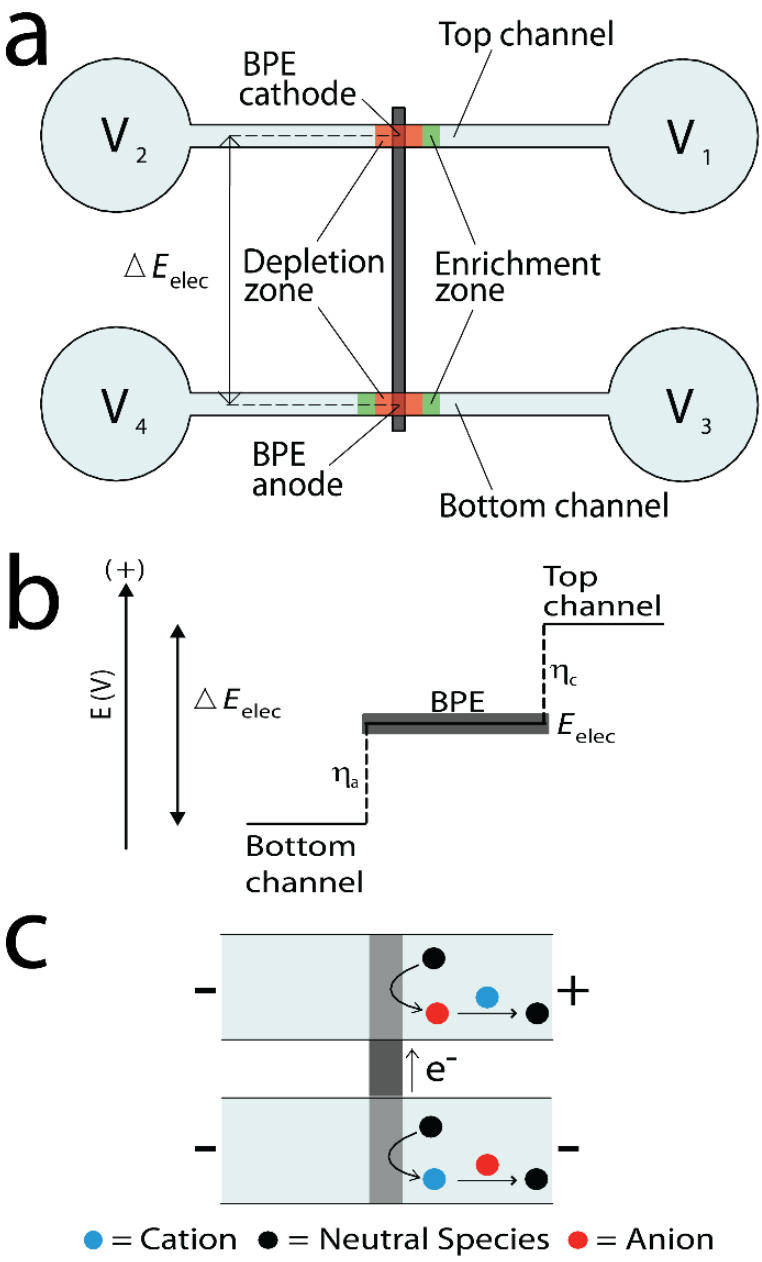

Scheme 2.2:

(a) Schematic illustrating a dual-channel BPE focusing device. (b) Schematic illustrating the voltage drop across the channels and BPE. (c) Schematic illustrating water electrolysis and buffer neutralization near a BPE.

BPE focusing is a member of a family of analyte enrichment techniques that is based on the principle of electrokinetic equilibrium. Methods in this family include counter-flow gradient focusing (CFGF),[53,115] isoelectric focusing (IEF),[116,117] field amplified sample stacking (FASS),[118,119] and isotachophoresis (ITP).[120,121] BPE focusing lies within the subfamily of CFGF methods, which also includes dynamic field gradient focusing (DFGF),[122,123] electric field gradient focusing (EFGF),[124,125] and temperature gradient focusing (TGF).[126,127] In all of these CFGF techniques, a local electric field is established within a fluidic channel, and used to control the electrophoretic velocity of a charged analyte. The electrophoretic force is then balanced against convective flow, and at the location where the forces sum to zero the analyte stops and enriches. The differences between CFGF methods depends primarily on how the local field is generated. In BPE focusing, it is produced electrochemically. Several of these electrokinetic equilibrium techniques have been used for the simultaneous separation and enrichment of analytes.[60,127-130] Ivory et al. recently reported an especially relevant example of DFGF which resulted in the separation and enrichment of cations and anions.[131] They accomplished this using a platform consisting of acrylic, ceramic, and membrane layers, along with a purge channel to remove electrolysis products. The effect was to produce a multi-component

electric field with EM of charged analytes in multiple directions, which are requirements for simultaneously separating and enriching cations and anions. To the best of our knowledge, Ivory's DFGF is the only other reported example of simultaneous anion and cation separation and enrichment.

BPE focusing in the dual-channel configuration is analogous to another enrichment technique known as ion concentration polarization (ICP).[58] ICP produces an ion depletion zone when a potential bias applied across two compartments causes a large proportion of ionic current to be carried by either anions or cations through a perm-selective material such as Nafion or a nanochannel that exhibits overlap of the electrical double layer.[132,133]

The dual-channel device presented in Scheme 2.2 avoids complex fabrication methods, but still enables separation and enrichment of $BODIPY^{2-}$ and $[Ru(bpy)_3]^{2+}$ by more than 100-fold.[62,131] Electric field measurements reveal that faradaic reactions occurring at a BPE spanning two microfluidic channels generate two ion depletion and three enrichment zones. Specifically, $TrisH^+$ is neutralized by OH^- in the top channel, while in the bottom channel acetate buffer is neutralized by H^+. Under focusing conditions, the strength of the axial electric field was measured in discrete segments along both the top and bottom channels. These measurements

demonstrate that stable enrichment is dependent upon the formation of an ion depletion zone and subsequent electric field gradient. In contrast to previous studies in which enrichment was limited to a region adjacent to one end of the BPE, tracer in the dual-channel scheme can enrich on either side of the BPE because the voltage drop creates unique mass transport conditions.[1,52,56,57,59-62] Electric field gradients in the bottom channel were also shown to contain multiple components which allow enrichment of $BODIPY^{2-}$, $[Ru(bpy)_3]^{2+}$, or both in a single microchannel.

EXPERIMENTAL

Chemicals

The fluorescent tracers, 4,4-Difluoro-1,3,5,7,8-pentamethyl-4-bora-3a,4a-diaza-s-indacene-2,6-disulfonic acid ($BODIPY^{2-}$, Invitrogen, Carlsbad, CA) and 98% Tris (2,2'-bipyridyl) ruthenium (III) Cl^- hexahydrate ($[Ru(bpy)_3]^{2+}$, Strem Chemicals, Newburyport, MA), were used for enrichment experiments. Poly(dimethylsiloxane) (PDMS) channels were prepared using a silicone elastomer and curing agent (Sylgard 184) from K.R. Anderson, Inc. (Morgan Hill, CA). A 0.5 M stock solution of Tris-$HClO_4$ (pH 8.1) was prepared from reagent grade Tris(hydroxymethyl)aminomethane (Sigma-Aldrich, St. Louis, MO) by dissolution in deionized water (18

MΩ·cm, Milli-Q Gradient System, Millipore, Bedford, MA) and titration with 2.0 N $HClO_4$ (Ricca Chemical Co., Arlington, TX). This stock solution was then diluted to 40.0 mM (pH 8.1) and used as background electrolyte. A 0.5 M stock solution of acetate buffer (pH 4.8) was prepared from reagent grade sodium acetate (trihydrate, EMD Chemicals, Gibbstown, NJ) by dissolution in 18 MΩ·cm deionized water (Millipore) and titration with 0.5 M HPLC-grade glacial acetic acid (Fisher Scientific, Fair Lawn, NJ). This stock solution was then diluted to 40.0 mM (pH 4.8) and used as background electrolyte.

Device Fabrication

The procedure for assembling the PDMS/glass microfluidic devices has been previously published.[134] Briefly, 100 nm-thick and 250 µm-wide Au electrodes with no adhesion layer (Evaporated Metal Films, Ithaca, NY) were patterned on glass slides using AZ P4620 photoresist (AZ Electronic Materials, Somerville, NJ) and standard photolithographic techniques. These BPEs were fabricated with continuous and split poles.[56] Two PDMS microchannels (6.0 mm-long, 50 µm-wide, and 8.7 µm-tall) were fabricated from a SU-8 5 (MicroChem, Newton, MA) mold patterned on a silicon wafer (University Wafer, South Boston, MA). The separation between the parallel channels was 9.0 mm (center-to-center). The PDMS channels were rinsed with

ethanol and dried under N_2, then the PDMS and glass surfaces were exposed to an O_2 plasma (10.5 W, model PDC-32G, Harrick Scientific, Ossining, NY) for 15 s, and finally the two parts were bound together with the BPE aligned at the channel center. The PDMS/glass microfluidic device was then placed in an oven at 65° C for 5 min to promote irreversible bonding.

Concentration Enrichment Experiments

Prior to each experiment, the microfluidic channels were rinsed using electroosmosis for 5 min with either 40.0 mM $TrisH^+$ buffer (pH 8.1) or 40.0 mM acetate buffer (pH 4.8) by applying 10.0 V to V_1 and V_3 while grounding V_2 and V_4 (Scheme 2.2a). Because EOF is somewhat suppressed at pH 4.8, pressure driven flow (PDF) was used to rinse the channels.[135] Next, the rinse buffer was removed from the microchannels and replaced with 60.0 µL of 40.0 mM buffer containing 1.0 µM $BODIPY^{2-}$, 10.0 µM $[Ru(bpy)_3]^{2+}$, or a mixture of 1.0 µM $BODIPY^{2-}$ and 10.0 µM $[Ru(bpy)_3]^{2+}$.

Using a custom-built power supply incorporating a C-series voltage source (Ultra Volt, Ronkonkoma, NY), 30.0 V was applied to V_1, with V_2, V_3, and V_4 grounded. The driving electrodes were coiled Au wires immersed in each of the four reservoirs. Enrichment of fluorescent tracer was observed using an inverted epifluorescence microscope (Eclipse TE 2000-U, Nikon, Tokyo, Japan) fitted with a CCD camera

(Cascade 512B, Photometrics, Tucson, AZ). PDF was initiated by creating a solution height differential in the reservoirs at the ends of the channel by adding or removing buffer. Measurements of PDF were estimated by tracking the movement of enriched bands after the 30.0 V driving potential was turned off, in which case all mass transport was due to PDF.

Images were collected and analyzed with image processing software (V++ Precision Digital Imaging, Auckland, New Zealand). A calibration of fluorescence intensities vs concentration was used to determine the enrichment factor (EF) by dividing the maximum tracer concentration in the enriched band by the initial tracer concentration, with all measurements being corrected for background fluorescence intensity.

Electric Field Profile and Voltage Measurements

All axial electric field measurements in the bottom channel were performed with the device depicted in Scheme 2.3 (not to scale). A Au BPE having a continuous and split pole was used to bring two PDMS microchannels (6 mm-long, 50 µm-wide, and 8.7 µm-high) into electrical contact. To collect the axial electric field profiles along the entire length of the 6.0 mm microchannel, eleven Au microbands (50 µm-wide) were spaced 495 µm apart (center-to-center). The two distal electric field measurements were made vs the coiled Au

electrodes placed in the reservoirs. As depicted in Scheme 2.3, microband number 7 was centered between the split portion of the BPE with the remaining microbands spaced evenly toward the reservoirs. Because of the manner the SDMM collects data, positive and negative electric fields were measured in the bottom channel. A similar finding was reported by Ivory and coworkers in their related simulations and experiments.[131,136]

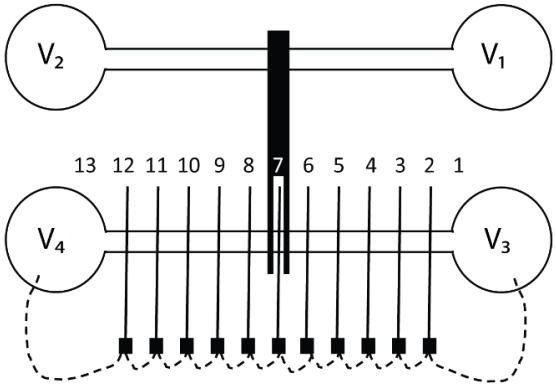

Scheme 2.3:

Schematic illustrating the microbands and dual-channel device used to measure the axial electric field strength in the bottom channel.

The microbands extended from below the PDMS monolith to expose a contact pad allowing connection to a breakout board and SDMM. The procedure for making these measurements has been previously reported.[57,61] The SDMM was turned on and began collecting potential difference measurements between driving

electrode 1 and microband 2 (Scheme 2.3). Next, the potential difference between microbands 2 and 3 was measured. The SDMM continued to sequentially measure the potential difference between each set of microbands until a measurement between microband 12 and driving electrode 13 was completed (Scheme 2.3). The acquisition time for each voltage measurement was ~0.1 s, and the voltage between pairs of microbands was recorded every 2.0 s. After ~5 measurements of the axial electric field across the entire microchannel with no voltage applied, 30.0 V was applied to V_1, with V_2, V_3, and V_4 grounded. Now, under enrichment conditions, the SDMM continued to collect electric field data for the remainder of each experiment.

When collecting measurements from 1 to 13 (Scheme 2.3), the electric field in the region from 1-7 is negative. Because voltage in the bottom channel is highest at the channel center and drops to 0 V at the grounded reservoirs, voltage at the first microband measured is lower than the voltage at the second microband. This means the difference between these measurements is negative, hence resulting in a negative electric field. Conversely, in the region from 7-13, the electric field is positive because the voltage at the first microband measured is higher than the voltage at the second microband. If the axial electric field were measured from 13 to 1 (Scheme 2.3), rather than from 1 to 13, the opposite

regions would have positive or negative electric fields. The voltage dropped across both the top and bottom channels was obtained from the axial electric field measurements by adding together each voltage measurement made between microbands.

Measurement of E_{elec}

The floating potential of the BPE, E_{elec}, was measured using a hand-held, digital multimeter equipped with PC-Link software (VA18B, Sinometer Instruments, Shenzhen, China). The potential difference between a microband extending from the BPE (Scheme 2.4) and the driving electrode (V_1) was assigned to E_{elec}. For all measurements of the BPE floating potential, the microchannels were initially filled with either 40.0 mM $TrisH^+$ buffer (pH 8.1) or 40.0 mM acetate buffer (pH 4.8) and rinsed by applying 10.0 V to V_1 and V_3, while grounding V_2 and V_4 (Scheme 2.2a). This voltage was applied for 5 min to allow electroosmosis to rinse the channel. Because EOF is somewhat suppressed at pH 4.8, pressure driven flow (PDF) was also used to rinse the channel.[135] Next, the rinse buffer was removed from each reservoir and replaced with 60.0 µL of 40.0 mM buffer containing 1.0 µM $BODIPY^{2-}$, 10.0 µM $[Ru(bpy)_3]^{2+}$, or a mixture of 1.0 µM $BODIPY^{2-}$ and 10.0 µM $[Ru(bpy)_3]^{2+}$.

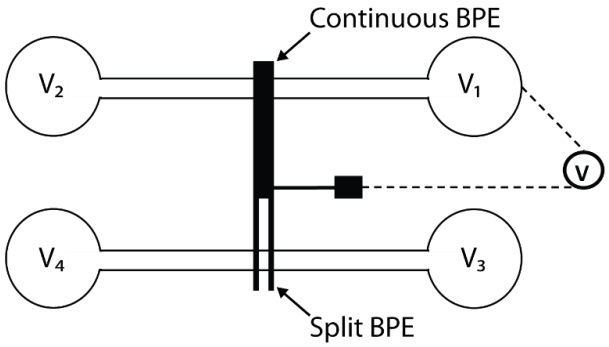

Scheme 2.4:

Schematic illustrating the device design used to measure E_{elec}.

The device design used to measure the floating potential of the BPE is depicted in Scheme 2.4 (not to scale). A Au BPE with a continuous and split pole was used to bring two PDMS microchannels (6 mm-long, 50 µm-wide, and 8.7 µm-high) into electrical contact.[56] A Au contact pad extending from the BPE was used to make a connection between the BPE, a hand-held voltmeter ("V" in Scheme 2.4), and the coiled Au driving electrode in reservoir V_1. A 30.0 V potential was applied to V_1 with respect to the grounded V_2, V_3, and V_4 reservoirs. The potential difference between the BPE and V_1 was recorded on a personal computer using PC-Link software (Sinometer Instruments, Shenzhen, China).

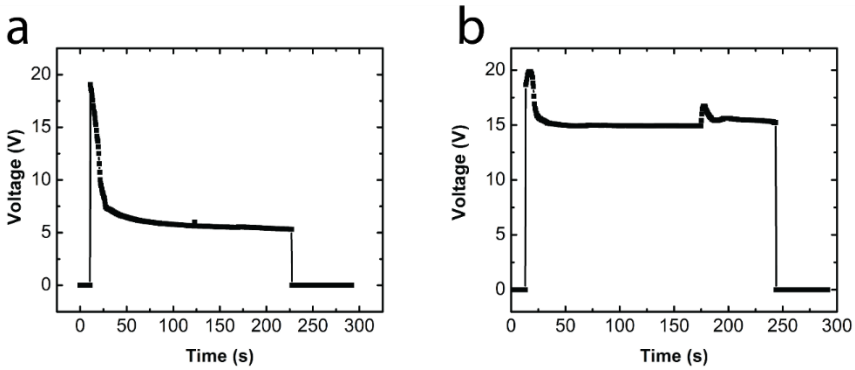

Figure 2.1:

(a) Plot of the floating BPE voltage vs time with both the top and bottom channels filled with 40.0 mM $TrisH^+$ buffer. (b) Plot of the floating BPE voltage vs time with the top channel filled with 40.0 mM $TrisH^+$ buffer and the bottom channel filled with 40.0 mM acetate buffer. During each of these experiments, 30.0 V was applied to V_1, while V_2, V_3, and V_4 were grounded.

Figure 2.1a shows a representative measurement of E_{elec} before, during, and after 30.0 V was applied to V_1. During this experiment, both the top and bottom channels were filled with 40.0 mM $TrisH^+$ buffer. At t = 0, E_{elec} = 0, but at later times (29 s - 227 s) it achieved a value of ~6 V before dropping again to 0 V at 228 s when the power source was turned off. The key finding is that E_{elec} attains a relatively constant value throughout the entire experiment. In Figure 2.1b, with the top channel filled with 40.0 mM $TrisH^+$ buffer and the bottom channel filled with 40.0 mM acetate buffer, the voltage of the BPE floats to a higher value of E_{elec} (~15 V). This result is due to a depletion region forming adjacent

the BPE anode when acetate buffer is neutralized in the bottom channel by electrogenerated H^+.

Results and Discussion

Basic Principles of Dual-Channel Enrichment

Most of our previous studies of BPE focusing have been directed toward BPEs embedded within a single microchannel (Scheme 2.1a).[1,52,56,57,59-62,64] If a sufficiently large voltage (E_{tot}) is applied across a buffer-filled microchannel containing a BPE, faradaic reactions, such as water oxidation and reduction, may occur at the poles of a BPE (Schemes 2.1b,c). These redox processes may lead to neutralization of the buffer, and in this case an ion depletion zone forms causing a sharp, local increase in solution resistance and hence an electric field gradient. Charged analytes then concentrate along this locally generated electric field gradient when convective flow is balanced against EM (Scheme 2.1d).

The basic operating principles of the dual-channel configuration (Scheme 2.2) are similar to those of the single-channel device. Specifically, ΔE_{elec}, which is the potential difference between the poles of the BPE, must exceed the redox potential for water oxidation and reduction (Scheme 2.2b).[1]

(2.1) $2H_2O - 4e^- \leftrightarrow O_2 + 4H^+$

(2.2) $2H_2O + 2e^- \leftrightarrow H_2 + 2OH^-$

(2.3) $TrisH^+ + OH^- \leftrightarrow Tris + H_2O$

(2.4) $CH_3CO_2^- + H^+ \leftrightarrow CH_3CO_2H$

If this condition is met, then water oxidation (eq 2.1) may proceed at the BPE anode to generate H^+ and electrons. Once water oxidation occurs, to maintain charge neutrality within the BPE, electrons shuttle through the BPE to reduce water (eq 2.2) and generate OH^- in the top channel. If an appropriately charged buffer capable of being neutralized by the products of water electrolysis is placed in either channel, an ion depletion zone, and thus an electric field gradient, should result. For example, in the top channel, $TrisH^+$ may be neutralized by OH^- (eq 2.3) or acetate buffer may be neutralized by H^+ (eq 2.4) in the bottom channel (Scheme 2.2c). Upon neutralization, counterions of the buffers are transported by a combination of convection and EM to the reservoirs where they charge pair with the products of water electrolysis.[59] The important point is that buffer neutralization and the formation of an ion depletion zone results in an electric field gradient where charged analytes may be enriched when convective flow balances EM.

Dual-Channel Focusing with $TrisH^+$ Buffer in the Top and Bottom Channels

To correlate the shape of the ion depletion zone to the local electric field within each microchannel, the axial electric field was measured. Figure 2.2a shows the device configuration used for these experiments. Figure 2.2b is an optical micrograph of the channel center. It shows two microbands, labeled BPE, that (when connected external to the channel) comprise the split BPE, and three additional microbands used for measuring the electric field. Note, we have previously shown that split and continuous BPEs are equivalent.[56] The microchannel, outlined in red, runs perpendicular to the microband electrodes. For all experiments within this subsection, the top and bottom channels were filled with 40.0 mM $TrisH^+$ buffer (pH 8.1) containing 1.0 µM $BODIPY^{2-}$. All dual-channel experiments were carried out with V_1 at 30.0 V, and V_2, V_3, and V_4 grounded (Scheme 2.2a).

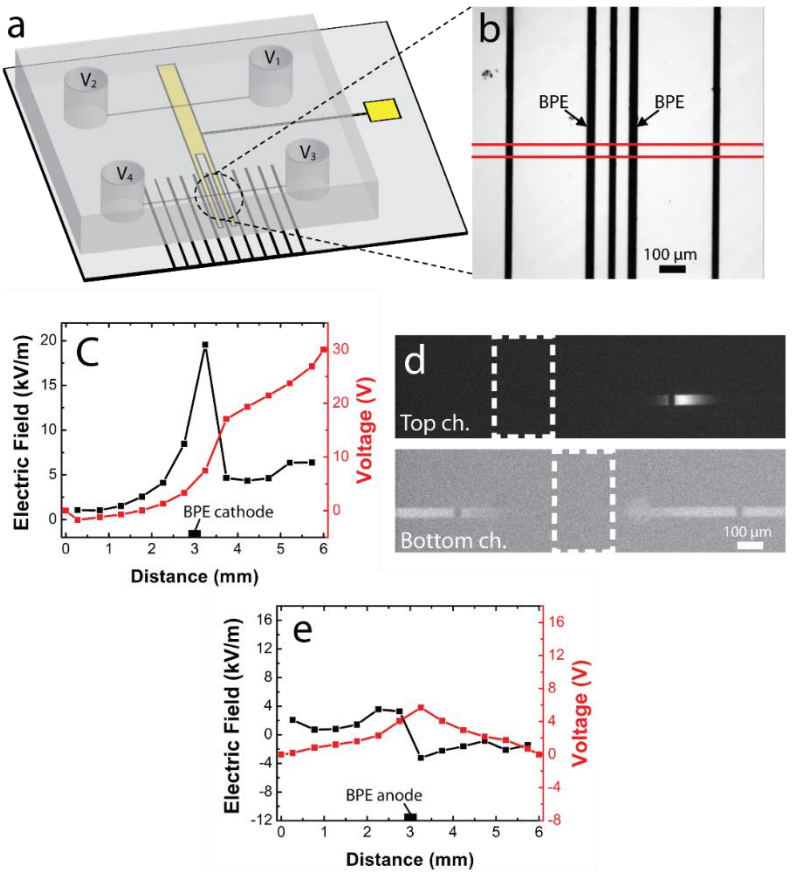

Channel	Solution Composition
top	40 mM $TrisH^+$ (pH 8.1), 1 µM $BODIPY^{2-}$
bottom	40 mM $TrisH^+$ (pH 8.1), 1 µM $BODIPY^{2-}$

Figure 2.2:

(a) Graphic illustrating the device used to measure the axial electric field gradient. (b) Optical micrograph showing a close-up of a split BPE and flanking microband electrodes used to measure the electric field. (c) Plot of the axial electric field (black trace) and voltage drop (red trace) in the top channel. (d) Fluorescence micrographs of enriched $BODIPY^{2-}$ bands in the top and bottom channels. The location of the BPE is indicated by dashed white lines. (e) Plot of the axial electric field (black trace) and voltage drop (red trace) in the bottom channel. The top and bottom channels were filled with 40.0 mM $TrisH^+$ buffer (pH 8.1) containing 1.0 µM $BODIPY^{2-}$. V_1 = 30.0 V and V_2, V_3, and V_4 were grounded.

In order to show that a steep electric field gradient forms in the bottom channel only in the presence of buffer capable of being neutralized by electrogenerated H^+, we perfomed the following control experiments. The red trace of Figure 2.2c shows the 30.0 V potential difference between reservoirs V_1 and V_2 in the top channel deviates from linearity as a result of water reduction and corresponding neutralization of $TrisH^+$ (eqs 2.2 and 2.3, respectively). This creates an ion depletion zone and causes the formation of a subsequent electric field gradient (Figure 2.2c black trace). Analyte enriches along the electric field gradient *via* the CFGF mechanism. Accordingly, an enriched band of the anionic tracer, $BODIPY^{2-}$, is observed in Figure 2.2d (top image) with an EF of 767-fold (1.6-fold/s).

Although enrichment in the top channel is not greatly influenced by the composition in the bottom channel, enrichment in the bottom channel is a strong function of its solution composition. With the bottom channel filled with $TrisH^+$ buffer, a shallow electric field gradient (Figure 2.2e, black trace) results that is unable to support a significant degree of enrichment. $BODIPY^{2-}$ accumulates adjacent to the BPE (Figure 2.2d, bottom image). The EF in the bottom channel is lower (58-fold, 0.2-fold/s) than in the top channel as a consequence of the shallow electric field gradient and lack of convective flow.

We attempted to generate a compact enriched band of $BODIPY^{2-}$ in the bottom channel by introducing PDF, but this was unsuccessful. Because the faradaic reaction at the BPE anode results in formation of H^+ (eq 2.1), there is no neutralization of $TrisH^+$ buffer and no depletion region forms. The key point is that with $TrisH^+$ buffer present in both the top and bottom channels, an ion depletion zone forms in the top channel which supports enrichment, while in the bottom channel, the absence of an ion depletion zone prevents enrichment.

Dual-Channel Focusing and Depletion with $TrisH^+$ Buffer in the Top Channel and Acetate Buffer in the Bottom Channel

For all experiments within this subsection, the top channel was filled with 40.0 mM $TrisH^+$ buffer (pH 8.1) containing 1.0 µM $BODIPY^{2-}$, and the bottom channel was filled with 40.0 mM acetate buffer (pH 4.8) containing either 1.0 µM $BODIPY^{2-}$ or 10.0 µM $[Ru(bpy)_3]^{2+}$. All dual-channel experiments were carried out with V_1 at 30.0 V, and V_2, V_3, and V_4 grounded (Scheme 2.2a). Under these conditions, the potential difference between the solution and the BPE poles (ΔE_{elec}, Scheme 2.2b) is sufficiently large to drive water electrolysis at each end of the BPE. As depicted in the red trace of Figure 2.3a, the 30.0 V potential difference between reservoirs V_1 and V_2 deviates from linearity as a result of water reduction and corresponding neutralization of $TrisH^+$ in

the top channel (eqs 2.2 and 2.3, respectively). This leads to a decrease in the number of charge carriers and induces the ion depletion zone shown in Scheme 2.2a. That is, because the resistivity in this region is much higher than elsewhere in the channel, a disproportionate percentage of E_{tot} drops here (Figure 2.3a, red trace from ~3-4 mm) and a corresponding electric field gradient forms (Figure 2.3a, black trace). Analyte enriches along the electric field gradient, *via* the CFGF mechanism described earlier, wherein EOF (in this case) balances EM. Accordingly, an enriched band of the anionic tracer, $BODIPY^{2-}$, is observed in Figure 2.3b (top image) with an EF of 264-fold (1.5-fold/s).

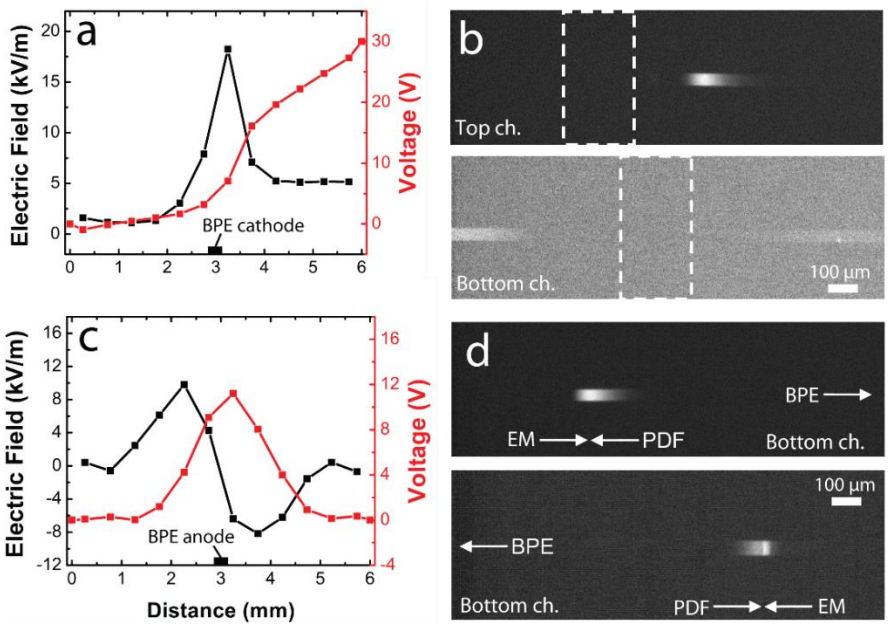

Channel	Solution Composition
top	40 mM $TrisH^+$ (pH 8.1), 1 µM $BODIPY^{2-}$
bottom	40 mM acetate (pH 4.8), 1 µM $BODIPY^{2-}$

Figure 2.3:

(a) Plot of the axial electric field (black trace) and voltage drop (red trace) in the top channel. (b) Fluorescence micrographs of enriched $BODIPY^{2-}$ bands in the top and bottom channels with the location of the BPE indicated by dashed white lines. (c) Plot of the axial electric field (black trace) and voltage drop (red trace) in the bottom channel. (d) Fluorescence micrographs of enriched $BODIPY^{2-}$ bands in the bottom channel with PDF = ~30 µm/s from right to left and left to right. The solution conditions are provided in the figure. V_1 = 30.0 V and V_2, V_3, and V_4 were grounded.

The BPE floats to an equilibrium potential, E_{elec}, that depends on the voltage difference applied across the top and bottom channels. Moreover, because the BPE is a conductor, E_{elec} is the same in both the top and bottom channel (Scheme

2.2b).[1] Because the reservoirs in the bottom channel are grounded, it follows that a potential difference exists between the BPE anode and reservoirs (Figure 2.3c, red trace). Clearly, E_{elec} plays a key role in determining the degree of enrichment in both channels and is important to measure.

We now turn to processes occurring in the bottom channel. When filled with acetate buffer, a steep electric field gradient is observed as a result of electrogenerated H^+ neutralizing acetate buffer (eqs 2.1 and 2.4) and the resulting formation of an ion depletion region and subsequent electric field gradient (Figure 2.3c, black trace). The electrochemical and chemical processes that lead to this effect are illustrated in Scheme 2.2c. Previously, we demonstrated that when the bottom channel is filled with $TrisH^+$ buffer, a steep electric field gradient capable of supporting a significant degree of enrichment does not form because $TrisH^+$ buffer may not be neutralized by H^+ generated at the BPE anode. The key point is that with $TrisH^+$ buffer present in the bottom channel, an ion depletion zone does not result, therefore preventing enrichment. However, with acetate buffer in the bottom channel, an ion depletion zone does form, which supports enrichment *via* the CFGF mechanism.

As shown in Figure 2.3c (red trace), the voltage in the bottom channel is highest at the channel center and decreases

to 0 V at each grounded reservoir. Interestingly, this causes $BODIPY^{2-}$ to migrate toward the channel center, leading to tracer accumulation (Figure 2.3b, bottom image) that is weak (51-fold, 0.3-fold/s) due to a lack of convective flow. There is no EOF in the bottom channel because the only possible direction for EOF would be from the channel center toward each of the grounded reservoirs. This would require the formation of a liquid-free zone, which is clearly not possible. It's also worth noting that there is no electric field directly above the BPE anode, and therefore $BODIPY^{2-}$ does not accumulate there. If $BODIPY^{2-}$ is replaced with cationic $[Ru(bpy)_3]^{2+}$ in the bottom channel, the direction of tracer EM reverses, thus resulting in $[Ru(bpy)_3]^{2+}$ depletion.

Tracer enrichment is quite different when convection, in the form of PDF (~30 μm/s), is introduced in the bottom channel. In this case, a compact enriched band of $BODIPY^{2-}$ forms (Figure 2.3d, top image, EF = 357-fold, 1.0-fold/s). Enrichment occurs because PDF counters EM along the electric field gradient. If the PDF (~30 μm/s) is in the opposite direction, an enriched $BODIPY2^{-}$ band is observed only on the opposite side of the BPE anode (Figure 2.3d, bottom image, EF = 154-fold, 0.9-fold/s).

The location of $BODIPY^{2-}$ enrichment can be altered because EM is in opposite directions on either side of the BPE anode. This behavior is not possible in a single-channel

device because the direction of EM is uniform throughout the channel.[52,59,60] Moreover, single-channel devices produce a strong electric field gradient along only one edge of the BPE, similar to that observed in the top channel of the dual-channel device, Figure 2.3a. However, with a multi-component electric field gradient in the bottom channel of the dual-channel scheme, the enrichment location may be determined by simply adjusting the direction of PDF.

With PDF in the bottom channel, the ion depletion regions shift, and hence the electric field gradients also change position.[57] Figure 2.4a shows the electric field gradient with PDF (~30 μm/s) from right to left. During the course of this experiment, acetate electromigrates toward the channel center, while H^+ (produced at the BPE) electromigrates toward the channel reservoirs. This means that with PDF from right to left, the H^+ concentration in the 0 to 3 mm region of the microchannel increases, the neutralization reaction occurs to a greater extent, and therefore the slope of the electric field increases. Conversely, the electric field gradient in the 3 mm to 6 mm region is shallower under these conditions. When the PDF is increased 4-fold, to ~120 μm/s, these effects are even more pronounced (Figure 2.4b).

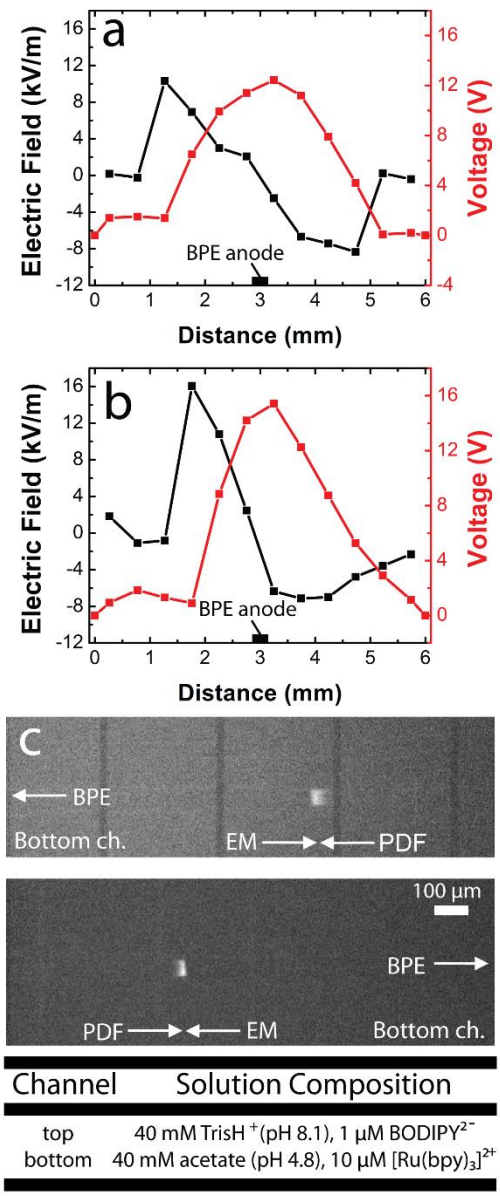

Figure 2.4:

Plot of the axial electric field (black trace) and voltage drop (red trace) in the bottom channel with PDF = ~30 µm/s (a) and PDF = ~120 µm/s (b) from right to left. (c) Fluorescence micrographs of enriched $[Ru(bpy)_3]^{2+}$ bands in the bottom channel with PDF = ~90 µm/s from right to left and left to right. The solution conditions are provided in the figure. V_1 = 30.0 V and V_2, V_3, and V_4 were grounded.

Figure 2.4c shows that the location of $[Ru(bpy)_3]^{2+}$ enrichment can also be controlled by changing the direction of PDF (~90 µm/s in this case) in the bottom channel. Note, however, that for a particular direction of PDF, the enriched band of $[Ru(bpy)_3]^{2+}$ is on the opposite side of the BPE compared to that observed for $BODIPY^{2-}$. This is because EM is in opposite directions (within the same region of the microchannel) for differently charged tracers. Another interesting point is that the rate of enrichment for $[Ru(bpy)_3]^{2+}$ is lower than that of $BODIPY^{2-}$ (1-fold/s vs 0.6-fold/s, respectively). This is because $[Ru(bpy)_3]^{2+}$ is transported by PDF from just one reservoir to the enrichment zone, while $BODIPY^{2-}$ is transported to the enrichment zone from both reservoirs by PDF and EM.

Simultaneous Separation and Enrichment of Anions and Cations

For all experiments within this subsection, the top channel was filled with 40.0 mM $TrisH^+$ buffer (pH 8.1) containing 1.0 µM $BODIPY^{2-}$, and the bottom channel was filled with 40.0 mM acetate buffer (pH 4.8) containing 1.0 µM $BODIPY^{2-}$ and 10.0 µM $[Ru(bpy)_3]^{2+}$. All experiments were carried out with V_1 at 30.0 V, and V_2, V_3, and V_4 grounded (Scheme 2.2a).

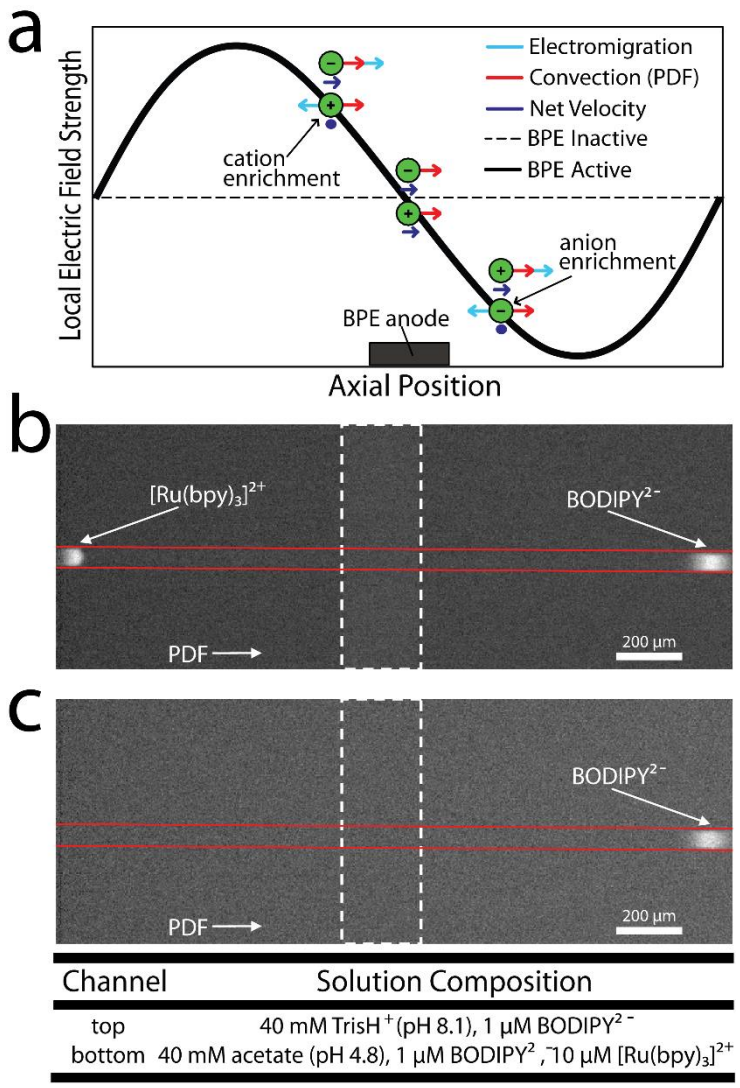

Figure 2.5:

(a) Schematic illustrating the direction of convection, EM, and net velocity of tracer in the bottom channel. (b) Fluorescence micrograph of enriched bands of $BODIPY^{2-}$ and $[Ru(bpy)_3]^{2+}$ in the bottom channel with PDF (~90 µm/s) from left to right. The location of the BPE is indicated by dashed white lines. (c) Fluorescence micrograph collected 3 seconds after (b) using a filter set capable of detecting only $BODIPY^{2-}$ showing an enriched $BODIPY^{2-}$ band only to the right of the BPE. The solution conditions are provided in the figure. V_1 = 30.0 V and V_2, V_3, and V_4 were grounded.

Thus far we have shown that the enrichment location of both $BODIPY^{2-}$ and $[Ru(bpy)_3]^{2+}$ can be controlled in the bottom channel because the voltage profile leads to EM in opposite directions in each half of the microchannel. Accordingly, with the multi-component electric field gradient in the bottom channel, it should be possible to separate and enrich mixtures of oppositely charged analytes. Figure 2.5a summarizes the situation. Here, PDF is directed from left to right, and the direction of EM depends on the charge on the tracer. At the channel center, where there is no electric field strength, ions experience no EM; therefore, their net velocity is dictated exclusively by convection. Moreover, because there is no EOF in the bottom channel, convection depends only on PDF. To the left of the BPE anode, anions move toward the channel center by both EM and PDF. In the same region, cations also experience PDF toward the channel center, but EM is in the opposite direction so enrichment occurs. An analogous argument can be made on the right side of the BPE anode for anion enrichment. In principle, then, if the right magnitude of PDF (left to right) is chosen, cations will enrich to the left of the BPE anode and anions will enrich to its right.

In Figure 2.5b, PDF (~90 μm/s) is directed from left to right. To the left of the BPE anode (indicated by dashed lines), $[Ru(bpy)_3]^{2+}$ (EF = 136-fold, 0.5-fold/s) enriches,

while $BODIPY^{2-}$ (EF = 113-fold, 0.4-fold/s) enriches to the right. This fluorescence micrograph was collected using a filter set capable of detecting both $BODIPY^{2-}$ and $[Ru(bpy)_3]^{2+}$. Three seconds after Figure 2.5b was collected, another fluorescence micrograph (Figure 2.5c) was recorded using a filter set capable of detecting only $BODIPY^{2-}$. In this micrograph, $BODIPY^{2-}$ enrichment occurs only to the right of the BPE anode, thereby confirming the identity of the two enriched bands. Importantly, the dual-channel microfluidic configuration leads to the simultaneous separation and enrichment of both anions and cations.

Although the EF for $[Ru(bpy)_3]^{2+}$ is greater than that of $BODIPY^{2-}$, as the experiment progresses, $BODIPY^{2-}$ continually enriches while $[Ru(bpy)_3]^{2+}$ enrichment plateaus. This is because $BODIPY^{2-}$ is transported to the enrichment region by both PDF and EM, while $[Ru(bpy)_3]^{2+}$ is transported to its enrichment location only by PDF. With $BODIPY^{2-}$ enriching at a steeper electric field gradient than $[Ru(bpy)_3]^{2+}$, this result is also consistent with previous discussions showing changes in the electric field gradient with respect to the magnitude of PDF.

Simultaneous Separation and Enrichment of Anions and Cations in the Top Channel

In addition to simultaneously separating and enriching both anions and cations in the bottom channel, an analogous

result may be achieved in the top channel by changing the voltage configuration. The top channel was filled with a solution of 1.0 µM $BODIPY^{2-}$, 10.0 µM $[Ru(bpy)_3]^{2+}$, and 40.0 mM $TrisH^+$ buffer (pH 8.1). The bottom channel was filled with a solution of 1.0 µM $BODIPY^{2-}$, 10.0 µM $[Ru(bpy)_3]^{2+}$, and 40.0 mM acetate buffer (pH 4.8). With V_1 and V_2 at 30.0 V and V_3 and V_4 grounded (Scheme 2.2a), $BODIPY^{2-}$ and $[Ru(bpy)_3]^{2+}$ were seen to simultaneously separate and enrich in the bottom channel with the addition of PDF from left to right. Simultaneous separation and enrichment was also observed in the top channel with PDF from right to left.

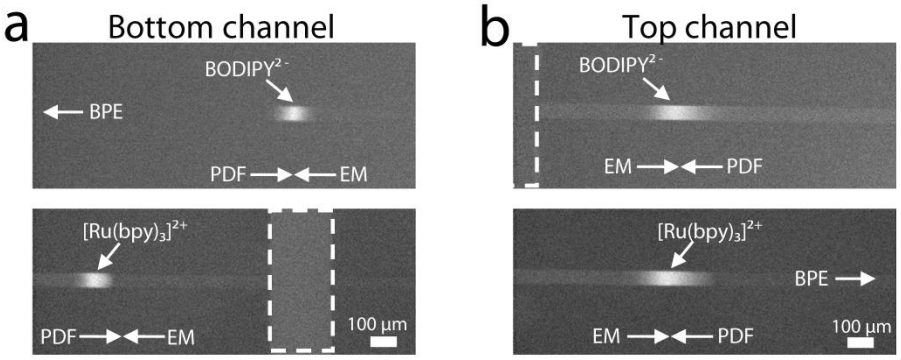

Figure 2.6:

(a) Fluorescence micrographs of enriched bands of $BODIPY^{2-}$ and $[Ru(bpy)_3]^{2+}$ in the bottom channel with PDF from left to right. The location of the BPE is indicated by dashed white lines or an arrow. (b) Fluorescence micrographs of enriched bands of $BODIPY^{2-}$ and $[Ru(bpy)_3]^{2+}$ in the top channel with PDF from right to left. The solution composition in the top channel was 1.0 µM $BODIPY^{2-}$, 10.0 µM $[Ru(bpy)_3]^{2+}$, and 40.0 mM $TrisH^+$ (pH 8.1) with the bottom channel composed of 1.0 µM $BODIPY^{2-}$, 10.0 µM $[Ru(bpy)_3]^{2+}$, and 40.0 mM acetate (pH 4.8). V_1, V_2 = 30.0 V and V_3, V_4 were grounded.

Figure 2.6a shows that, in the bottom channel, $BODIPY^{2-}$ enriches to the right of the BPE anode (indicated by white dashed lines or an arrow), while $[Ru(bpy)_3]^{2+}$ enriches to its left with PDF from left to right. Roughly 15 s after Figure 2.6a was collected, two additional fluorescence micrographs (Figure 2.6b) were recorded showing that in the top channel $BODIPY^{2-}$ enriches to the right of the BPE cathode (indicated by white dashed lines or an arrow), while $[Ru(bpy)_3]^{2+}$ enriches to its left with PDF from right to left. These results qualitatively demonstrate that with V_1 and V_2 at 30.0 V and V_3 and V_4 grounded (Scheme 2.2a), the voltage drop and electric field gradient in the top channel are likely similar to that observed in the bottom channel with the difference being that voltage drops from the reservoirs toward the channel center where the ion depletion zone and region of high resistivity forms.

SUMMARY AND CONCLUSIONS

The key finding reported in this paper is that the dual-channel BPE focusing scheme can be used to produce multiple ion depletion and enrichment zones. Moreover, the unique mass transport properties and multi-component electric field gradient that forms in the bottom channel provides a means to simultaneously separate and enrich anions and cations in

a single microchannel. This result was previously unachievable in single-channel, BPE fluidic devices. The dual-channel microelectrochemical platform requires only simple fabrication procedures and facilitates enrichment of cations, anions, or both, all while controlling the enrichment location. Therefore, with the capability of enriching and transporting anions and cations on an inclusive platform, the analysis of complex mixtures of charged analytes may be realized.

Chapter 3: Explorations in Bipolar Electrochemistry

Synopsis

Bipolar electrode focusing is a technique for enriching and separating charged analytes in a microchannel near an ion depletion zone and concomitant elevated electric field. Enrichment occurs when electrophoretic velocity balances bulk fluid flow. Analytes enrich at different points along the elevated electric field gradient due to differences in their electrophoretic mobility and hence electrophoretic velocity at a given field strength. Here, we demonstrate proof-of-concept biomolecule separation and enrichment. Moreover, BPE focusing is used to enrich analytes in parallel with one hundred BPEs simultaneously. Lastly, metal deposition at a BPE cathode is demonstrated to mediate BPE focusing.

Experimental

Chemicals and Materials

Poly(dimethylsiloxane) (PDMS) channels were prepared using a silicone elastomer and curing agent (Sylgard 184) from K.R. Anderson, Inc. (Morgan Hill, CA). Tris-$HClO_4$ (pH 8.1) buffer solutions were prepared from reagent grade Tris(hydroxymethyl)aminomethane (Sigma-Aldrich, St. Louis, MO) by dissolution in deionized (DI) water (18 MΩ·cm, Milli-Q Gradient System, Millipore, Bedford, MA) and titration with

2.0 N $HClO_4$ (Ricca Chemical Co., Arlington, TX). The fluorescent tracer, 4,4-Difluoro-1,3,5,7,8-pentamethyl-4-bora-3a,4a-diaza-s-indacene-2,6-disulfonic acid ($BODIPY^{2-}$, Invitrogen, Carlsbad, CA) was used for enrichment experiments. Cyanine5 (Cy5) labeled 12-base and Cyanine3 (Cy3) labeled 38-base single stranded DNA (ssDNA) oligonucleotides were purchased from Integrated DNA Technologies (Coralville, IA). The ssDNA was received as lyophilized pellets and rehydrated in $TrisH^+$ buffer. Cy3 labeled streptavidin protein was purchased from Jackson ImmunoResearch (West Grove, PA). Cy3 labeled 18-base single stranded peptide nucleic acid (ssPNA) was purchased from Cambridge Research Biochemicals (Billingham, United Kingdom).

Device Fabrication

Experiments were performed with a PDMS/glass microfluidic device with a 100.0 nm-thick and 100.0 µm-wide Au BPE with no adhesion layer (Evaporated Metal Films, Ithaca, NY) patterned on a glass slide using AZ P4620 photoresist (AZ Electronic Materials, Somerville, NJ) and standard photolithographic techniques. The microchannel (6.0 mm-long, 10.0 µm-wide, and 1.8 µm-tall) was fabricated from a SU-8 2002 (MicroChem, Newton, MA) mold patterned on a silicon wafer (University Wafer, South Boston, MA). The PDMS

channel was rinsed with ethanol and dried under N_2, then the PDMS and glass surfaces were exposed to an O_2 plasma (10.5 W, model PDC-32G, Harrick Scientific, Ossining, NY) for 15 s, and finally the two parts were bound together with the BPE aligned at the channel center. The PDMS/glass microfluidic device was then placed in an oven at 65° C for 5 min to promote irreversible bonding. For parallel focusing experiments, multiple BPEs and channels, as described above, were present on a single device.

Biomolecule Enrichment and Separation

Thus far, all the BPE focusing studies described in this dissertation have utilized fluorescent tracers to monitor enrichment and separation. However, a primary interest for on-chip enrichment and separations is biomolecule applications that include enhancing hybridization kinetics of DNA[137] and lowering analyte detection limits.[138] Therefore, our goal was to demonstrate proof-of-concept biomolecule enrichment and separation by BPE focusing.

Biomolecule enrichment experiments were performed as follows. Prior to each experiment, the microfluidic channel was filled and rinsed using electroosmosis for 5 min with 100.0 mM $TrisH^+$ buffer (pH 8.1) by applying 20.0 V across the microchannel. Next, the rinse buffer was removed from the

microchannel and replaced with 100.0 mM buffer containing 1.0 µM Cy5 labeled 12-base ssDNA. Using a custom-built power supply incorporating a C-series voltage source (Ultra Volt, Ronkonkoma, NY), 200.0 V was applied across the microchannel. The driving electrodes were coiled Au wires dipped into each of the two reservoirs. Enrichment of the ssDNA was observed using an inverted epifluorescence microscope (Eclipse TE 2000-U, Nikon, Tokyo, Japan) fitted with a CCD camera (Cascade 512B, Photometrics, Tucson, AZ). Images were collected and analyzed with image processing software (V++ Precision Digital Imaging, Auckland, New Zealand).

Upon application of the 200.0 V potential bias, water electrolysis proceeds at the BPE poles. OH^- produced at the BPE cathode neutralizes $TrisH^+$ buffer and therefore generates an ion depletion zone and locally elevated electric field gradient where fluorophore labeled DNA is enriched. Figure 3.1a shows a fluorescence micrograph of 12-base ssDNA enriching upstream of the BPE cathode, thereby demonstrating biomolecule enrichment by BPE focusing. To demonstrate biomolecule separation, an identical experiment was performed with 100.0 mM buffer, 1.0 µM Cy5 labeled 12-base, and 1.0 µM Cy3 labeled 38-base ssDNA filling the microchannel. The two fluorescence micrographs of Figure 3.1b depict the outcome of this experiment with the 38-base and 12-base DNA strands enriched and separated from one another. These fluorescence

micrographs were collected using two filter sets capable of detecting only Cy3 or Cy5, thereby confirming the identity of the enriched ssDNA bands. Full baseline separation was not achieved in these preliminary studies, but the enriched bands were fully resolved. Compared to Figure 3.1a, the 12-base DNA strand in Figure 3.1b (top image) enriches in a much larger region of the microchannel. This is because, as described previously, the ionic strength of the depletion zone increases as the two DNA strands enrich, thus causing the local electric field gradient to become more shallow.[57] Consequently, the ssDNA enriches in a larger region of the microchannel.

Next, to demonstrate protein enrichment and separation, 19 nM Cy3 labeled streptavidin and 1.0 μM $BODIPY^{2-}$ filled the microchannel. Upon application of a 200.0 V bias, streptavidin and $BODIPY^{2-}$ enriched and separated from one another with baseline resolution (Figure 3.1c). The two fluorescence micrographs were collected using two filter sets capable of detecting only Cy3 or $BODIPY^{2-}$, thereby confirming the identity of the enriched protein and small molecule bands. The larger separation distance achieved in Figure 3.1c compared to Figure 3.1b is because of the large difference in μ_{ep} between the 52 kDa protein and 466 g/mol molecule. Together, these results demonstrate proof-of-concept biomolecule enrichment and separation for future application.

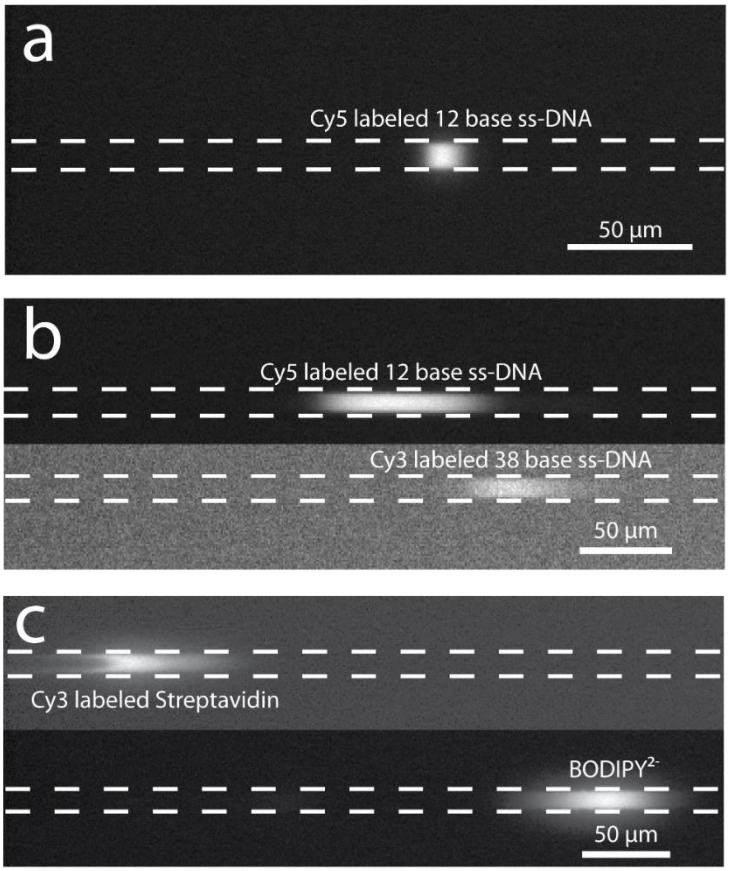

Figure 3.1:

For all experiments, the microchannel was 10.0 µm-wide, 6.0 mm-long, and 1.8 µm-tall and filled with 100.0 mM $TrisH^+$ buffer. A 100.0 µm-wide Au BPE was embedded at the channel center and a 200.0 V bias was applied across the microchannel. The white dashed lines represent the channel walls. (a) Fluorescence micrograph showing enrichment of 1.0 µM Cy5 labeled 12-base ssDNA. (b) Two fluorescence micrographs collected ~3 s apart using two filter sets to visualize Cy5 labeled 12-base and Cy3 labeled 38-base ssDNA enriching and separating in a single microchannel. The initial concentration of each ssDNA was 1.0 µM. (c) Two fluorescence micrographs collected ~3 s apart using two filter sets to visualize Cy3 labeled streptavidin protein and $BODIPY^{2-}$ tracer enriching and separating in a single microchannel. The initial concentration of protein was 19 nM and $BODIPY^{2-}$ was 1.0 µM.

A final experiment was performed with Cy3 labeled 18-base ssPNA. PNA is a neutral species and therefore cannot be enriched by BPE focusing. However, the Cy3 label contains two sulfonic acid functional groups that provide negative charge. We wanted to examine if a neutral species with a charged label could be enriched by BPE focusing. Therefore, the microchannel was filled with 0.6 µM Cy3 labeled ssPNA with 100.0 mM $TrisH^+$ buffer. With application of 200.0 V bias, the ssPNA enriched near the BPE cathode (Figure 3.2a). Unlike previous studies, upon completion of the ~10 min enrichment experiment, the enriched band remained after the 200.0 V bias was turned off. Without the bias, the locally elevated electric field collapses and the enriched band is expected to disperse. However, the localized fluorescence persists after the experiment. Because PNA is a neutral molecule with low solubility,[139] we hypothesize the enriched band of PNA does not entirely disperse because it has partially precipitated from solution. Figure 3.2b is an optical micrograph showing an enhanced view of the microchannel region adjacent the BPE cathode where the PNA was enriched. Interestingly, there is debris at this location in the microchannel, possibly precipitated PNA. These experiments demonstrate that neutral species may be enriched by BPE focusing when labeled with a charged tracer.

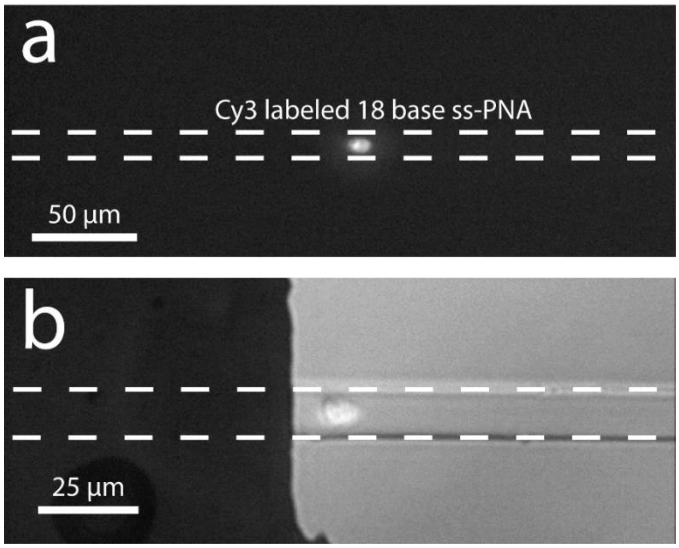

Figure 3.2:

For all experiments, the microchannel was 10.0 µm-wide, 6.0 mm-long, and 1.8 µm-tall and filled with 100.0 mM $TrisH^+$ buffer. A 100.0 µm-wide Au BPE was embedded at the channel center and a 200.0 V bias was applied across the microchannel. The white dashed lines represent the channel walls. (a) Fluorescence micrograph showing enrichment of 0.6 µM Cy3 labeled 18-base PNA. (b) Optical micrograph collected after the experiment in (a) showing debris in the channel region adjacent the BPE cathode where the PNA was enriching.

PARALLEL FOCUSING

BPEs do not require a direct external electrical connection making them well-suited for both microscale electrochemistry applications, where it might be difficult to make such a connection, and for high-density electrode array applications, where it would be impractical to make thousands or millions of individual electrode connections. In fact, our group has previously demonstrated sensing arrays

consisting of one thousand BPEs can be operated with only a single pair of driving electrodes.[49,50] Here, we exploit this aspect of bipolar electrochemistry to demonstrate ion depletion zone formation and subsequent analyte enrichment in parallel. Ion concentration polarization (ICP) has been previously employed for parallel enrichment, but complex fabrication of Nafion interconnections was required.[140] However, with BPE focusing, only a simple conductive BPE and power supply is required to initiate parallel enrichment.

Figure 3.3a shows a schematic illustration of a device containing five BPEs and channels to generate five separate ion depletion and enrichment zones in parallel. Figure 3.3b is an image of a five channel microelectrochemical BPE device used for parallel enrichment. Each of the microchannels has a 100.0 μm-wide BPE embedded at the channel center. Devices with as many as 100 microchannels have been prepared and operated. The principles for parallel enrichment in 100 microchannels is identical to that of a single channel, but parallel focusing takes advantage of the fact that BPEs do not require an external electrical connection to operate.

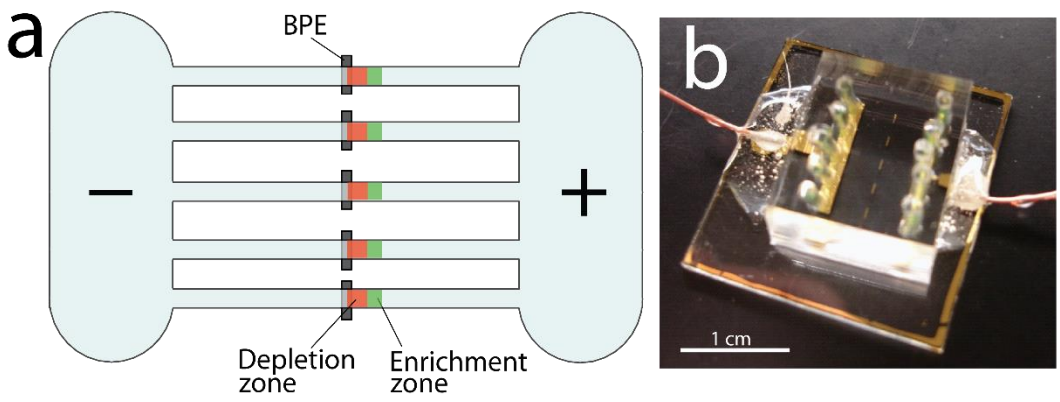

Figure 3.3:

(a) Schematic illustrating parallel enrichment at five BPEs embedded between a single pair of driving electrodes. (b) Photograph of a device for parallel enrichment containing five Au BPEs embedded at the center of 5 microchannels.

Parallel BPE focusing experiments in devices containing 100 microchannels proceeded as follows. First, the microfluidic channels were rinsed using electroosmosis for 5 min with 100.0 mM $TrisH^+$ buffer (pH 8.1) by applying 20.0 V across the microchannels. Next, the rinse buffer was removed from the microchannels and replaced with 100.0 mM buffer containing 1.0 μM $BODIPY^{2-}$. The driving electrodes were microfabricated Au contact pads at the base of the two communal reservoirs shared amongst the 100 channels. Figure 3.4a is an optical micrograph showing 8 of the 100 Au BPEs embedded at the center of each microchannel. Enrichment of fluorescent tracer was observed using an inverted epifluorescence microscope fitted with a CCD camera.

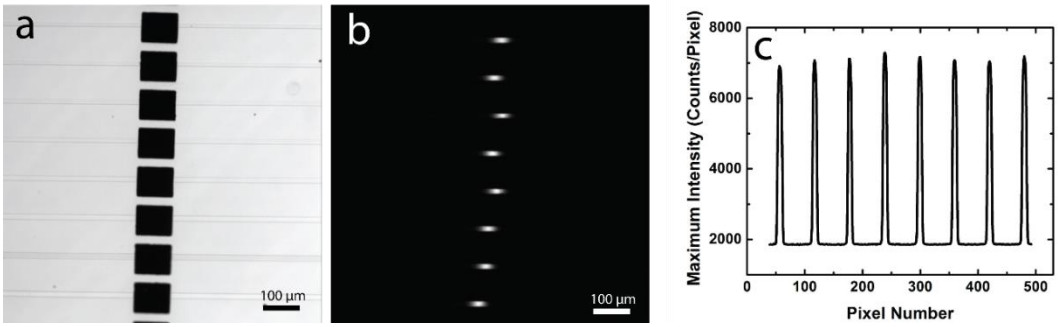

Figure 3.4:

(a) Optical micrograph showing 8 of 100 Au BPEs (100.0 µm-wide) embedded between two driving electrodes. (b) Fluorescence micrograph corresponding to the device region in (a) showing enriched $BODIPY^{2-}$ in 8 of the 100 parallel microchannels. (c) Plot of maximum fluorescence intensity vs pixel number for the enriched $BODIPY^{2-}$ bands in (b). A 200.0 V bias was applied between the driving electrodes. The channels were filled with a solution containing 100.0 mM $TrisH^{+}$ and 1.0 µM $BODIPY^{2-}$.

Upon application of a 200.0 V potential bias, water electrolysis proceeds at the BPE poles. OH^{-} produced at the BPE cathode neutralizes $TrisH^{+}$ buffer to generate a locally elevated electric field gradient in each of the microchannels where $BODIPY^{2-}$ tracer is enriched. Figure 3.4b is a fluorescence micrograph showing 8 of the 100 enriched $BODIPY^{2-}$ bands in the device. Due to limitations of our CCD camera, only 8 enriched bands could be imaged at once. Importantly, the bands enrich at nearly the same position in each microchannel, indicating the local electric field strength

in the parallel microchannels is relatively uniform. Moreover, Figure 3.4c, a plot of the maximum fluorescence intensity of the 8 microbands in Figure 3.4b, demonstrates the $BODIPY^{2-}$ bands are enriching to an equal degree because the fluorescence intensity correlates to tracer concentration. These experiments demonstrate that BPE focusing can be applied in a parallel format to enrich multiple bands simultaneously, while only requiring a simple power supply and a pair of driving electrodes.

ELECTRODEPOSITION MEDIATED ENRICHMENT

Experiments were performed to demonstrate the onset of BPE focusing as a potential readout for sensing applications. The idea is illustrated in Scheme 3.1 where a 50 µm-wide and 40 µm-wide Au BPE are spaced 29 µm apart (edge-to-edge). The microchannel is then filled with 100 mM $TrisH^+$ buffer, 1.0 µM $BODIPY^{2-}$, and 1.8 mM $CuSO_4$. An E_{tot} of 290 V, not sufficiently high to drive water electrolysis at the BPE poles, was then applied across the microchannel. 290 V is sufficiently high to deposit Cu^{2+} at the cathode of the 50 µm-wide BPE, but importantly not at the 40 µm-wide BPE. At this point, Cu dendrites begin to grow from the cathode of the 50 µm-wide BPE (Scheme 3.1b).[141,142] Cu^{2+} continues to deposit until making ohmic contact with the 40 µm-wide BPE, at which point l_{elec}

becomes 119 µm. Consequently, 290 V is now sufficiently large to drive water electrolysis at the BPE poles, thereby generating a local electric field gradient when $TrisH^+$ is neutralized by OH^-, which nearly immediately leads to $BODIPY^{2-}$ enrichment (indicated by the green, Scheme 3.1c). Importantly, without Cu^{2+}, no enrichment is observed.

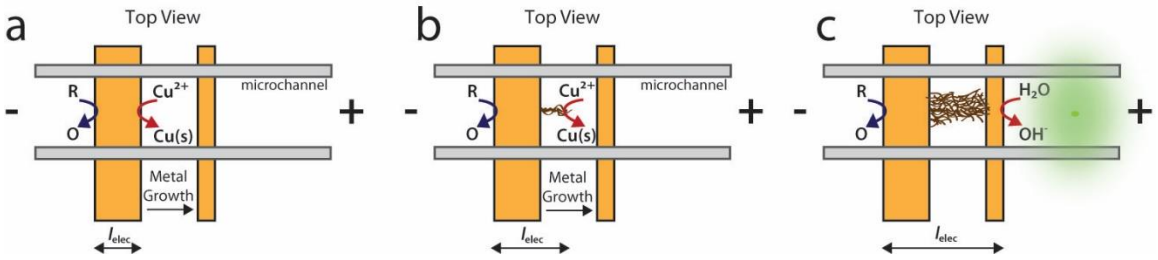

Scheme 3.1:

(a-c) Schematic illustrating the use of BPE focusing as a readout to detect the presence of Cu^{2+}.

An experiment as illustrated in Scheme 3.1 was performed as follows. The microfluidic channel was rinsed using electroosmosis for 5 min with 100.0 mM $TrisH^+$ buffer (pH 8.1) by applying 20.0 V. Next, the rinse buffer was removed from the microchannel and replaced with 100.0 mM buffer containing 1.0 µM $BODIPY^{2-}$ and 1.8 mM $CuSO_4$. 290 V was then applied across the microchannel. Figure 3.5a is an optical micrograph showing the beginning of Cu^{2+} deposition at the cathode of the 50 µm-wide BPE. The Cu^{2+} deposition continues (Figure 3.5b) for ~5 min, at which point the Cu dendrites contact the

40 µm-wide BPE and induce $BODIPY^{2-}$ enrichment (Figure 3.5c). Unfortunately, the enriched band of $BODIPY^{2-}$ remains stable for only ~1 min. The enriched band then begins to shift in the microchannel, indicating an unstable ion depletion zone. The continued deposition of Cu^{2+} and growth of the BPE cathode likely contribute to the instability. In conclusion, the onset of BPE focusing was employed as a readout to detect the presence of Cu^{2+}.

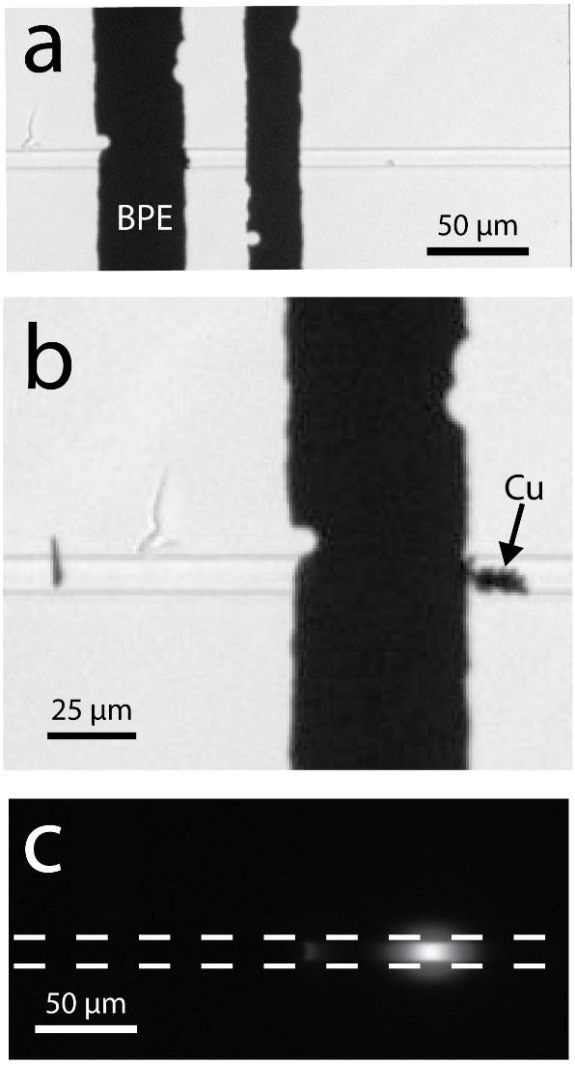

Figure 3.5:

(a) Optical micrograph showing a 50 µm-wide and 40 µm-wide Au BPE spaced 29 µm apart (edge-to-edge). Cu^{2+} is just beginning to deposit on the longer BPE. (b) Optical micrograph showing Cu dendrite growth. (c) Fluorescence micrograph showing an enriched $BODIPY^{2-}$ band forming after ~5 min. The microchannel was filled with 100 mM $TrisH^{+}$ buffer, 1.0 µM $BODIPY^{2-}$, and 1.8 mM $CuSO_4$. A 290 V bias was applied across the microchannel.

Summary and Conclusions

There are three important findings from the studies reported in this chapter. First, BPE focusing can be employed for the enrichment and separation of biomolecules including DNA, proteins, and PNA. Second, by taking advantage of the fact that bipolar electrochemistry does not require a direct external electrical connection, one hundred BPEs are operated simultaneously in parallel with only a single pair of driving electrodes to enrich multiple analyte bands. Third, metal deposition at a BPE is used to mediate BPE focusing, which could serve as a sensing readout.

Chapter 4: Electrochemically Mediated Seawater Desalination

Synopsis

Seawater desalination is achieved using a simple power supply, such as a battery, to apply a 3.0 V potential bias across a microelectrochemical cell comprising two microchannels spanned by a single bipolar electrode (BPE) to drive Cl^- oxidation and water electrolysis at the BPE poles. The resulting ion depletion zone and associated electric field gradient selectively direct ions into a branching microchannel, consequently producing partially desalted water.

Introduction

With global demand rising faster than availability, fresh water is quickly becoming a limited resource. In fact, the United Nations estimates one-third of the world's population is living in water stressed regions, and by 2025 this number is expected to double.[72] Seawater desalination is an attractive solution to this problem, because seawater accounts for more than 97% of the world's water supply.[101,143] Currently, the primary limitation preventing the widespread use of seawater desalination as a fresh water supply is the immense amount of energy required to drive the process.[81]

Here, we describe a new, electrochemically-mediated desalination (EMD) method for membraneless seawater desalination.

Our approach for desalination is illustrated in Scheme 4.1a. A seawater feed is separated into brine and desalted water streams at the junction of a branched microchannel where a bipolar electrode (BPE)[2] is present. The anodic pole of the BPE generates an ion depletion zone,[58] and hence a local electric field gradient that directs ions present in seawater to the brine channel. Importantly, this device operates with an energy efficiency of 25 mWh/L (25±5% salt rejection, 50% recovery), which is near the theoretical minimum amount of energy required for this process (~17 mWh/L).[144,145] In addition to this energy efficiency, the approach provides three other important benefits relative to currently available desalination methods. First, EMD does not require a membrane, thereby eliminating a major drawback of reverse osmosis (RO), currently the most widespread method for desalination.[146] Second, EMD requires only a simple 3.0 V power supply to operate and therefore, in the future, may be employed in resource-limited settings using a battery or low-power, renewable energy source. Third, the EMD platform may be prepared with little capital investment and could be implemented in a massively parallel format.[147]

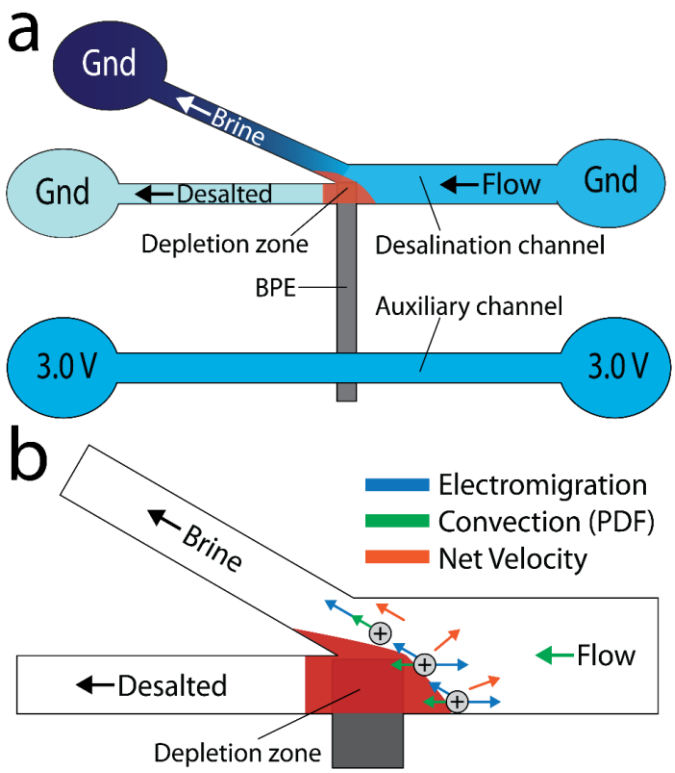

Scheme 4.1:

Schematic illustration of (a) the BPE desalination device and (b) the region of interest near the BPE anode and ion depletion zone depicting the net velocity vectors of a cationic species under the combined forces of electromigration and convection. Gnd = ground.

Our group has developed microfluidic technologies using BPEs for the enrichment,[52] separation,[60] depletion,[64] and controlled delivery[65] of charged analytes. In all cases, the approach relies on the formation of a locally generated electric field gradient and control over convection. The basic operating principles of BPEs[1] and how they are able to generate electric field gradients have been previously

described.[56,57,59] Briefly, if a sufficiently high potential bias (E_{tot}) is applied across a microfluidic channel in which a BPE is present, faradaic reactions will occur at the BPE poles. In seawater, these faradaic reactions result in the formation of an ion depletion zone (region of high solution resistivity), thus producing a local electric field gradient and providing a means for controlling the movement of ions.[63]

Several other techniques, including dynamic field gradient focusing[122] and electric field gradient focusing,[124] also rely on a gradient in the electric field to control the transport of charged analytes. Most relevant to this work is a phenomenon called ion concentration polarization (ICP),[133] which generates an ion depletion zone when a potential bias causes a large proportion of ionic current to be carried by either anions or cations through a perm-selective material or a nanochannel exhibiting overlap of the electrical double layer. In fact, Han and coworkers have recently shown that ICP can be adapted to seawater desalination with a reported energy efficiency of 3750 mWh/L (~99% salt rejection, 50% recovery) for a small-scale system.[112] A number of other electrochemical approaches, including capacitive deionization,[148] a desalination battery,[149] and electrodialysis,[150] have also been implemented for seawater desalination, although these techniques are more commonly

used to desalinate brackish water because their power consumption scales with the extent of salt removal.[108]

EXPERIMENTAL

Chemicals

98% Tris (2,2'-bipyridyl) ruthenium (II) Cl^- hexahydrate ($[Ru(bpy)_3]^{2+}$, Strem Chemicals, Newburyport, MA), was used as a fluorescent tracer in the desalination experiments. Poly(dimethylsiloxane) (PDMS) channels were prepared using a silicone elastomer and curing agent (Sylgard 184) from K.R. Anderson, Inc. (Morgan Hill, CA). Natural seawater was collected from Port Aransas, Texas, USA. Solutions of Na_2SO_4 were prepared from 99% Na_2SO_4 (anhydrous, Acros Organics, Fair Lawn, NJ) by dissolution in deionized water (18 MΩ·cm, Milli-Q Gradient System, Millipore, Bedford, MA). Solutions of NaCl were prepared from 99.5% NaCl (SigmaUltra, Sigma-Aldrich, St. Louis, MO) by dissolution in deionized water.

Device Fabrication

The procedure for assembling the PDMS/quartz microfluidic devices is as follows. Pyrolyzed photoresist carbon (PPC)[151] microband electrodes were fabricated on quartz substrates (Technical Glass Products, Painesville Township, OH) using AZ 1518 photoresist (AZ Electronic Materials, Somerville, NJ) and standard photolithographic techniques.

The photoresist was spin coated onto the substrates at 500 rpm for 10 s, then 3500 rpm for 45 s, and finally 500 rpm for 5 s before being soft baked at 100 °C for 45 s. A mask aligner (Süss MicroTec, Garching, Germany) and photomask (CAD/Art Services, Inc., Brandon, OR) were used to achieve a desired electrode pattern on the substrate. The exposure was 10 s using a UV lamp intensity of 9.7 mW/cm^2. The substrates were then developed for approximately 12 s using AZ 400K developer (AZ Electronic Materials) diluted 1/4 (v/v) with deionized water.

The patterned photoresist substrates were then pyrolyzed in a quartz tube furnace (model 55035, Lindberg, Watertown, WI) with a forming gas of 5% H_2 and 95% N_2 (Regen, Praxair, Danbury, CT) continuously flowing at 100 sccm. The temperature was ramped from 25 °C to 1000 °C at a rate of 5 °C/min and then held at 1000 °C for 1 h before cooling back to 25 °C. As previously described by our group, the PPC microbands undergo a decrease in width and thickness after pyrolysis.[152] A top-down optical microscope (Nikon AZ 100, Nikon, Tokyo, Japan) equipped with a CCD camera (QuantEM:512SC, Photometrics, Tucson, AZ) was employed to determine the lateral dimensions of the PPC microbands. For conductivity and electric field measurements, PPC microbands were bonded to copper wires *via* larger bonding pads using conductive silver paste (62% weight solids, Electron

Microscopy Sciences, Hatfield, PA) and then insulated with epoxy resin (5 min epoxy, Devcon, Danvers, MA).

PDMS microchannels (desalination channel inlet 2.5 mm-long, 100 µm-wide, and 22 µm-tall, desalination channel outlets 2.5 mm-long, 50 µm-wide, and 22 µm-tall, auxiliary channel 5.0 mm-long, 100 µm-wide, and 22-µm tall) were fabricated from a single SU-8 2025 (MicroChem, Newton, MA) mold patterned on a silicon wafer (University Wafer, South Boston, MA). The separation between the parallel channels was 6.0 mm (center-to-center). The brine outlet branched from the desalted stream at a 30° angle (Scheme 4.1a). Reservoirs were made using a 3 mm diameter metal punch to remove PDMS at each microchannel extremity. An optical profilometer (NT9100, Veeco, Plainview, NY) was employed to determine the height of the SU-8 microchannel mold. The PDMS channels were rinsed with ethanol and dried under N_2 before both the PDMS and quartz surfaces were exposed to an air plasma (10.5 W, model PDC-32G, Harrick Scientific, Ossining, NY) for 15 s, and finally the two parts were bound together with the BPE aligned at the channel centers and upstream of the branched microchannel (Scheme 4.1a). The PDMS/quartz microfluidic device was then placed in an oven at 65 °C for 5 min to promote irreversible bonding.

Desalination Experiments

Before each experiment, a solution of seawater spiked with 20.0 µM $[Ru(bpy)_3]^{2+}$ was used to fill the desalination channel. The auxiliary channel was filled with seawater. To prevent obstruction of the microfluidic channel, sand and debris present in the seawater sample were removed *via* sedimentation before use. No other pre-treatment was required. Using a hand-held conductivity meter (Con 6, Oakton, Vernon Hills, IL), the seawater conductivity was measured to be ~50 mS/cm, which is an accepted value for seawater.[88] Pressure driven flow (PDF) was initiated by creating a solution height differential in the reservoirs at the ends of the channel by adding or removing seawater.

Initially, 35.0 µL was added to the inlet reservoir of the desalination channel while 10.0 µL was added to each of the outlet reservoirs. This fill created a PDF (~0.08 µL/min) from inlet to outlets. A power supply (PWS4721, Tektronix, Beaverton, OR) was used to apply a 3.0 V bias between the desalination and auxiliary channels necessary to generate the electric field gradient for desalination. To ensure decoupling of the AC and DC circuits during the *in-situ* conductivity measurements, a 3.2 V battery pack (2 AA batteries, Duracell, Bethel, CT) was used to drive the desalination process. The driving electrodes dipped into each reservoir were Pt wires. The fluorescent tracer was observed

using an inverted epifluorescence microscope (Eclipse TE 2000-U, Nikon) fitted with a CCD camera (Cascade 512B, Photometrics). Images were collected and analyzed with image processing software (V++ Precision Digital Imaging, Auckland, New Zealand). When desired, either electric field or conductivity measurements were collected as desalination proceeded.

During seawater desalination, the primary processes occurring at the anode are Cl^- and water oxidation, respectively. However, oxidation of the PPC anode may also occur if the applied potential is sufficient to drive this process.[153] If oxidation of the BPE anode occurs, it reduces the surface area of the electrode, thus limiting the time desalination can proceed once the anode has been entirely oxidized. Figure 4.1a shows a PPC BPE anode before desalination. After ~10 min of desalination with a 3.0 V bias (Figure 4.1b), the anode surface area is diminished, which indicates oxidation of the BPE is occurring. After ~30 min, the BPE anode is almost entirely oxidized (Figure 4.1c).

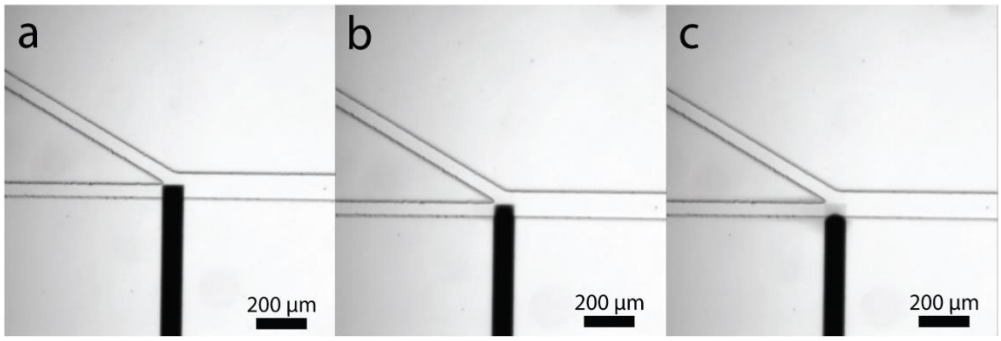

Figure 4.1:

Optical micrographs of a PPC BPE anode during a desalination experiment with a 3.0 V bias at 0 min (a), after ~10 min (b) and ~30 min (c).

Because of this instability, experiments reported here were limited to ~30 min. We are presently investigating the feasibility of using alternative electrode materials that exhibit a higher degree of stability in seawater. Note too, that dissolution of the BPE may result in the formation of ions that lead to an increase in the local conductivity measured in the desalted stream. Therefore, the reported conductivities in the desalted stream and the extent of desalination should be viewed as minimums.

Electric Field Profile Measurements

The axial electric field profile within the desalination channel (Scheme 4.1a) was monitored using a scanning digital multimeter (SDMM, Model 2700, Keithley Instruments, Cleveland, OH) equipped with a multiplexer module (Model

7701, Keithley). The acquisition time for each voltage measurement was ~0.1 s, and the voltage between pairs of microbands recorded every 2.0 s. To collect the axial electric field profile along the centermost ~3.2 mm of the 5.0 mm-long microchannel, twelve PPC microbands (67 µm-wide) were spaced ~323 µm apart (center-to-center). As depicted in Figure 4.2, these microbands surround either side of the 82 µm-wide BPE.

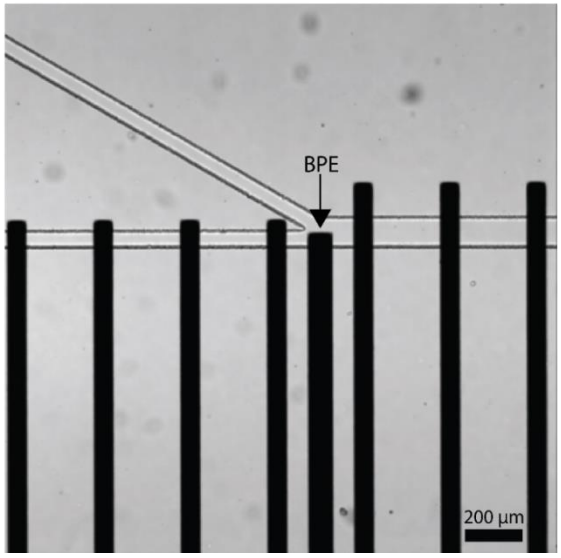

Figure 4.2:

Optical micrograph of PPC microbands and BPE device used to collect axial electric field measurements.

Conductivity Measurements

In-situ conductivity measurements were performed using the bipolar pulse technique[154] with a method described by Soper and coworkers.[155,156] The solution conductivity in the desalted

stream was monitored using a pair of PPC microbands (Figure 4.3) and the circuit depicted in Scheme 4.2. All circuit components were assembled in-house. The exposed portion of the microbands were 50 µm-long, 40 µm-wide, and spaced by ~60 µm (center-to-center).

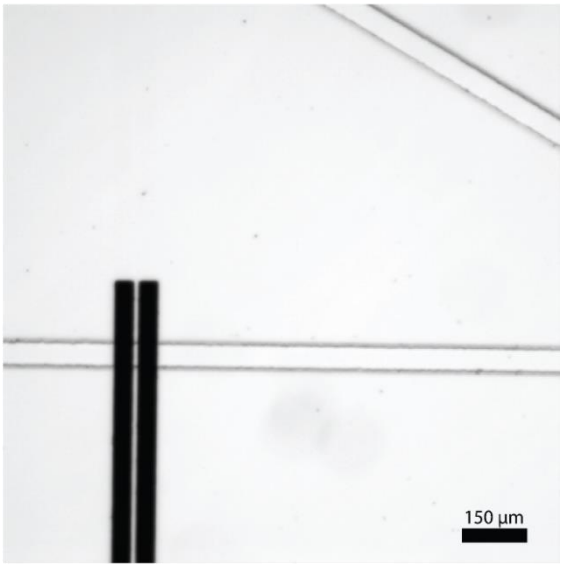

Figure 4.3:

Optical micrograph of PPC microbands embedded in the desalted stream used to collect *in-situ* conductivity measurements.

A function generator (Model 182A, Wavetek, San Diego, CA) was used to drive a ±0.75 V bipolar pulse at 5000 Hz through the upstream PPC microband, while the other microband was at virtual ground. As the signal is passed through the microchannel, the solution conductivity affects the current flow between PPC microbands ($V_O = -R_f i_f$), therefore modulating

the output voltage (V_o) from the transimpedance amplifier with a feedback resistance (R_f) of 511, 400 Ω. Next, the signal is passed through a sample and hold amplifier. Using the trigger of the function generator (Wavetek) and a digital delay/pulse generator (Model DG535, Stanford Research Systems, Sunnyvale, CA), sample collection was set to occur ~25 µs prior to the rising edge of the waveform. Data was collected for a total of 5 µs. The sampled signal was then passed through a second-order, 16 Hz low-pass filter before a multimeter (Model 2700, Keithley), operated with ExcelLINX software (Keithley), was used to collect the DC voltage measurement. The voltage was recorded every 0.5 s.

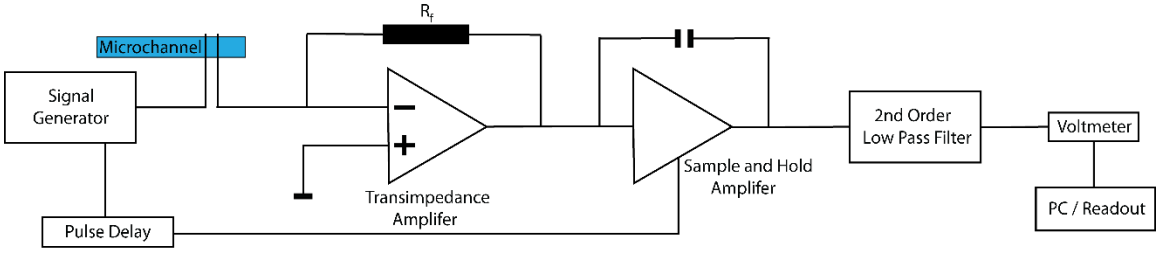

Scheme 4.2:

Schematic illustrating the home-built conductivity circuit employed for measuring the desalted stream conductivity on-chip.

These measurements were correlated to the solution conductivity using a calibration curve of solution conductivity vs the change in measured voltage (ΔE). Figure

4.4 shows a representative 4-point calibration curve (R^2 = 0.99) collected using seawater dilutions of known conductivity.

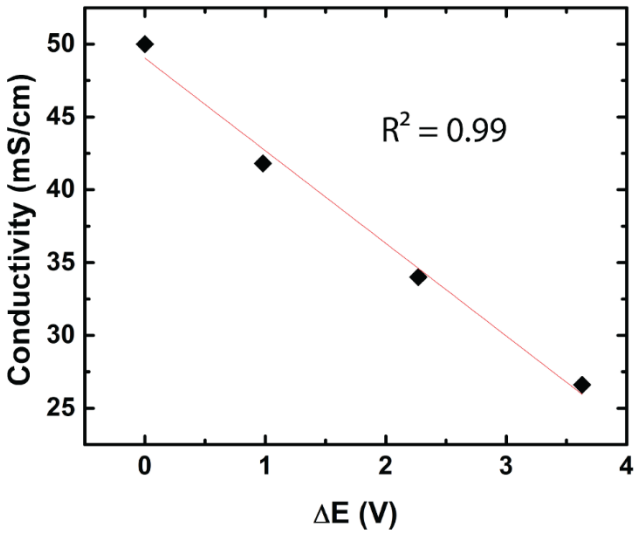

Figure 4.4:

A representative plot of solution conductivity vs change in voltage (ΔE) for a desalination device.

To account for variations in device fabrication and response, each trial required a calibration curve to correlate changes in voltage to solution conductivity. The average conductivity in the desalted stream of five independently prepared devices was 37.5±2.5 mS/cm, indicating a ~25% salt rejection from the feed seawater. The conductivity of the feed seawater was 50 mS/cm.

Flow Rate Measurements

PDF rates through the microchannel inlet and desalted stream (Scheme 4.1a) were measured by monitoring the velocity of the fluorescent tracer after the power source was turned off. Total flow rates were approximately 0.08 µL/min from inlet to outlets. Flow through each of the branched streams was ~0.04 µL/min.

Total Current Measurements

The total current flowing through the device was monitored using the circuit depicted in Scheme 4.3. A power supply (PWS4721, Tektronix) was used to apply a 3.0 V potential difference between the desalination and auxiliary channels necessary to generate the electric field gradient for desalination. The driving electrodes dipped into each reservoir were Pt wires. A multimeter (Model 6517B, Keithley) operated with a custom-written LabVIEW program (National Instruments, Austin, TX) was used to collect current measurements.

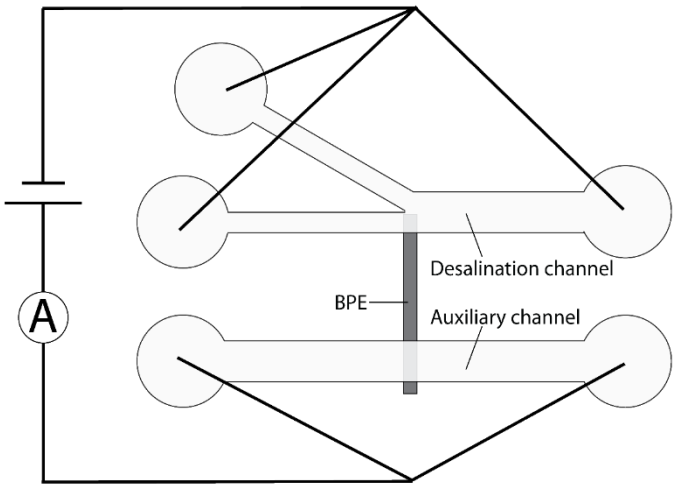

Scheme 4.3:

Schematic illustrating the circuit employed to make total current measurements.

Numerical Simulations

In this section, we present the computational methods used to model the EMD of a 50 mS/cm NaCl solution. The three-dimensional geometry of the simulated system is exactly the same as that used for the experiments. The computer model simulated PDF initiated in the desalination channel as well as the distributions of local ion concentrations and local electric field. We assume Cl^- oxidation is the faradaic reaction occurring at the BPE anode. The model was developed based on numerical schemes with inherent parallelism, allowing the straightforward implementation at modern high-performance computational platforms (supercomputers).

The model is based on equations describing the hydrodynamic, mass/charge transport, and electrostatic

problems. Assuming that the liquid is incompressible, the local flow velocity field (**v**) can be described by the Navier-Stokes equation (eq 4.1)

$$\rho\left(\frac{\partial \mathbf{v}}{\partial t}+\mathbf{v}\cdot\nabla\mathbf{v}\right)=-\nabla p+\eta\nabla^2\mathbf{v}\,, \tag{4.1}$$

where ρ and η are the mass density and dynamic viscosity of the liquid, and p is hydrostatic pressure. Spatiotemporal variations in the concentrations of Na^+ and Cl^- are governed by balance eqs 4.2 and 4.3

$$\frac{\partial n_{Na}}{\partial t}=\nabla\cdot\left(D_{Na}\nabla n_{Na}\right)-\frac{F}{RT}\nabla\cdot\left(D_{Na}\nabla\phi\right)-n_{Na}\nabla\cdot\mathbf{v}\,, \tag{4.2}$$

$$\frac{\partial n_{Cl}}{\partial t}=\nabla\cdot\left(D_{Cl}\nabla n_{Cl}\right)+\frac{F}{RT}\nabla\cdot\left(D_{Cl}\nabla\phi\right)-n_{Cl}\nabla\cdot\mathbf{v}-r\,, \tag{4.3}$$

where n is the species concentration, D is the diffusion coefficient in the bulk fluid, ϕ is the local electric potential; F, R, and T represent the Faraday constant, molar gas constant, and temperature, respectively, **v** is the flow velocity, and r is the electrochemical reaction term describing a reduction in Cl^- concentration due to faradaic reactions at the BPE anode.

The local concentrations of the species and the local electric potential are related by the Poisson equation (eq 4.4)

$$\nabla^2\phi=-q_e\frac{n_{Na}-n_{Cl}}{\varepsilon_0\varepsilon_r}\,, \tag{4.4}$$

where q_e is the elementary charge, ε_0 and ε_r are the vacuum permittivity and dielectric constant. We assumed that the

hydrodynamic problem (eq 4.1) can be decoupled from the species transport problem (eqs 4.2 and 4.3) and the electrostatic problem (eq 4.4); i.e., that the density and viscosity of the fluid are independent of the ionic strength.

Instead of a direct numerical solution of eq 4.1, the simulation of low-Reynolds number flow was performed with the lattice-Boltzmann method (LBM). In the LBM, a discretized version of the Boltzmann equation with linearized collision operator is solved.[157-160] The method simulates hydrodynamic phenomena by tracking the time evolution of distribution functions of fictitious particles that are confined to a spatial lattice and move with discrete velocity, $\mathbf{c}_i$, during discrete time steps. The particle distribution function $f_i(\mathbf{r},t)$ represents the probability of finding a particle with velocity $\mathbf{c}_i$ at position $\mathbf{r}$ and time t. Each time step is divided into separate streaming and collision steps. Velocities $\mathbf{c}_i$ are chosen such that in one streaming step a particle moves along a lattice link from one lattice node to its neighbor. Subsequently, particle distribution functions f_i are redistributed according to the discrete collision operator. The local fluid density $\rho(\mathbf{r},t)$ and velocity $\mathbf{v}(\mathbf{r},t)$ are obtained from the first-order and second-order moments of the particle distribution functions (eqs 4.5 and 4.6):

(4.5) $$\rho(\mathbf{r},t) = \sum_i f_i(\mathbf{r},t)$$, and

(4.6) $$\mathbf{v}(\mathbf{r},t) = \frac{\sum_i \mathbf{c}_i f_i(\mathbf{r},t)}{\rho(\mathbf{r},t)}$$

At the solid-liquid interface, the no-slip boundary condition was implemented by application of the halfway bounce-back rule.[161] Usually, the LBM models are designated as DxQy, where x is the lattice dimensionality and y refers to the number of lattice links from a given lattice node to its neighbors (including the node itself) located on a simple cubic lattice. In this work, we used the D3Q19 lattice, a lattice with 18 links at each lattice node, which can be obtained by projecting the four-dimensional face-centered hypercubic lattice onto three-dimensional space.[162] It should be noted that we used the same D3Q19 lattice also for the numerical solution of the transport equations (eqs 4.2 and 4.3) and the Poisson equation (eq 4.4).

Transport equations were resolved with a numerical approach proposed by Capuani et al.,[163] which is based on identifying the species fluxes between neighboring nodes of a spatial lattice. The symmetric formulation of the flux between neighboring nodes ensures strict local mass/charge conservation. In that approach, the fluxes are the fundamental dynamical objects that couple external fields to both charged species concentration and fluid flow velocity. To resolve eqs 4.2 and 4.3, the following boundary conditions

were imposed: (i) fluxes normal to the channel walls are zero for both charged species (Na^+ and Cl^-); (ii) the flux of Na^+ normal to the anodic BPE surface was zero; and (iii) the flux of Cl^-, j_{Cl}, normal to the anodic BPE surface was determined from a given current density across this surface

$$j_{Cl} = \frac{I_{BPE}}{S_{BPE}} \frac{1}{q_e}, \quad (4.7)$$

where I_{BPE} is the current through the BPE and S_{BPE} is the contact surface area of the BPE anode with the solution.

The Poisson equation (eq 4.4) was resolved by an under-relaxation finite difference method adapted to the D3Q19 lattice. Specifically, the weight coefficients, ω, to determine the updated local value of the electric potential by accounting for its values in neighboring lattice nodes are

$$\omega = \frac{1}{6\left(1+\sqrt{2}\right)} \text{ and } \omega = \frac{1}{6\left(2+\sqrt{2}\right)} \quad (4.8)$$

for the nearest and the next-nearest nodes, respectively. An under-relaxation coefficient of 0.25 was used to ensure numerical stability during calculation of the electrical potential in the region close to the BPE.

In this study, we performed simulations assuming the following values for the physical parameters: ρ = 1.023 × 10^3 kg/m^3, η = 0.966 mPa·s, T = 298.16 K, D_{Cl} = 2.032 × 10^{-9} m^2/s, D_{Na} = 1.334 × 10^{-9} m^2/s, ε_r = 78. The current through the BPE was assumed as I_{BPE} = 50 nA and the BPE surface area (S_{BPE}) in contact with the solution in the desalination channel as S_{BPE}

= 82 µm × 50 µm (BPE width x length). The potential of the BPE was assumed to be 0.9 V and determined from the difference between the externally applied voltage (3.0 V) and the sum of the standard potentials for Cl^- oxidation and water reduction (1.3 V and 0.8 V). The concentrations of Cl^- and Na^+ in the inlet reservoir of the desalination channel were assumed as 3.3121×10^{26} ions/m^3, which corresponds to a molarity of 0.55 M.

Results and Discussion

Electrochemically Mediated Desalination Mechanism

The EMD experiments reported here were carried out using a PDMS/quartz hybrid microfluidic device (22 µm-tall channels with a 100 µm-wide inlet and two 50 µm-wide outlets) outfitted with a pyrolyzed photoresist carbon (PPC)[151] BPE. Both channels were filled with seawater collected near Port Aransas, Texas, USA. To prevent obstruction of the microfluidic channel, sand and debris present in the seawater sample were removed *via* sedimentation before use. Importantly, no other pre-treatment was required. This is in contrast to membrane-based desalination where further pre-treatment, such as disinfection and the addition of anti-scaling chemicals, is required to prevent fouling and maintain the structural integrity of the membrane.[96]

The experimental arrangement is shown in Scheme 4.1a. In the desalination channel, seawater is spiked with a fluorescent cationic tracer, tris (2,2'-bipyridyl) ruthenium (II) Cl^- ($[Ru(bpy)_3]^{2+}$), representative of ionic motion. A total pressure driven flow (PDF) of ~0.08 µL/min is initiated between the inlet and outlets by creating a solution height differential between them. Next, using Pt driving electrodes dipped into each of the five reservoirs, E_{tot} = 3.0 V is applied. This creates a sufficiently large potential difference between the BPE poles to drive Cl^- oxidation and water reduction at the BPE anode and cathode, eqs 4.9 and 4.10, respectively. Importantly, Cl^- oxidation results in the neutralization of Cl^- and hence an ion depletion zone and local electric field gradient near the BPE anode.

(4.9) $$2Cl^- - 2e^- \leftrightarrow Cl_2$$

(4.10) $$2H_2O + 2e^- \leftrightarrow H_2 + 2OH^-$$

(4.11) $$2H_2O - 4e^- \leftrightarrow O_2 + 4H^+$$

Although Cl^- oxidation is known to be the dominant anodic process occurring in seawater,[164] water oxidation also occurs by eq 4.11. Electrogenerated H^+ arising from water oxidation may neutralize anions present in seawater, such as bicarbonate and borate, thus further contributing to ion depletion and the electric field gradient.

The electrophoretic velocity (u_{ep}) of an ion is governed by eq 4.12, where μ_{ep} is its electrophoretic mobility and V_l is the local electric field strength.

$$u_{ep} = \mu_{ep} V_l \tag{4.12}$$

In all regions of the desalination channel depicted in Scheme 4.1b, except near the ion depletion zone, ionic transport is dominated by PDF, which results in a net movement toward the outlets. However, as ions approach the local electric field gradient, they experience an increasing u_{ep}. At some point on this gradient, u_{ep} will exceed the convective velocity, and therefore cations will be directed toward the grounded reservoir in the brine stream. To maintain electroneutrality within the microchannel, anions are also directed into the brine stream.

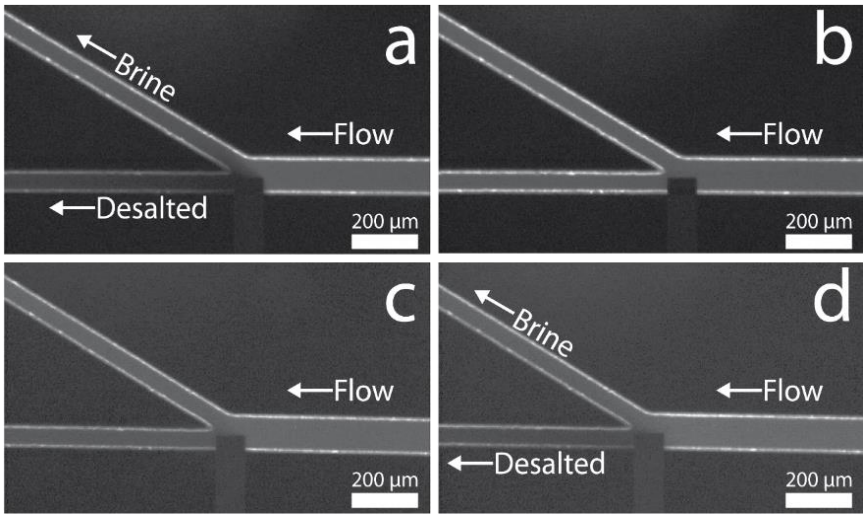

Figure 4.5:

Fluorescence micrographs showing the location of $[Ru(bpy)_3]^{2+}$ tracer, which is representative of the ions present in seawater. (a) The tracer in seawater is directed into the brine stream with E_{tot} = 3.0 V. (b) Same as (a) except E_{tot} = 0.0 V. In this case, the tracer flows into both outlets. (c) In 50 mS/cm Na_2SO_4, the tracer flows into both outlets with E_{tot} = 3.0 V. (d) In 50 mS/cm NaCl, the tracer is directed into the brine stream with E_{tot} = 3.0 V. In all cases, the total PDF was ~0.08 µL/min.

Figure 4.5 provides fluorescence micrographs confirming the electrochemically driven separation of ions. In Figure 4.5a, $[Ru(bpy)_3]^{2+}$ tracer, which represents the ions in seawater, is selectively directed into the brine stream. Conversely, water flowing into the lower channel is depleted of tracer. During this desalination process, *in-situ* conductivity measurements were made. The average conductivity in the desalted stream from five individual trials was

37.5±2.5 mS/cm, indicating a ~25±5% salt rejection from the feed seawater (50 mS/cm). The power source was then turned off (Figure 4.5b, E_{tot} = 0.0 V), whereupon the fluorescent tracer flowed into the desalted stream and the conductivity returned to 50 mS/cm. Although the salt rejection is lower than mature desalination technologies, the EMD process is far from optimized.

The experiment represented in Figure 4.5c was carried out exactly like that described for Figure 4.5a, but using 50 mS/cm Na_2SO_4 instead of seawater. The purpose of this experiment is to demonstrate that the formation of a local electric field gradient is essential for driving desalination. The Na_2SO_4 eliminates the possibility of an ion depletion zone forming due to eq 4.9 or by the neutralization of weak bases present in seawater with electrogenerated H^+. In this case, there is no selective redirection of $[Ru(bpy)_3]^{2+}$, which emphasizes the importance of Cl^- for desalting. The slight decrease in fluorescence intensity in the desalted stream occurs as a result of O_2, generated by water oxidation, quenching the $[Ru(bpy)_3]^{2+}$ fluorescence.[165] Experiments were also carried out exactly like that described for Figure 4.5a, except with 50 mS/cm NaCl. In this case (Figure 4.5d), $[Ru(bpy)_3]^{2+}$ is directed into the brine stream, clearly implicating Cl^- as a critical factor in the desalination process.

Electric Field Measurements

Axial electric field profile measurements were performed using the procedure described in the Experimental Section to confirm the formation of a local electric field gradient in the presence of NaCl. The SDMM data yields both positive and negative electric field measurements,[63,136] and therefore the data is presented as the absolute electric field strength for clarity. When the desalination channel is filled with seawater (red trace, Figure 4.6) or 50 mS/cm NaCl (blue trace, Figure 4.6), there is a sharp increase in the local electric field strength near the BPE anode (centered at 2.5 mm) compared to when the channel is filled with 50 mS/cm Na_2SO_4 (black trace, Figure 4.6). These measurements demonstrate that no local electric field gradient is observed in the presence of Na_2SO_4. Importantly, these measurements also support that Cl^- oxidation (eq 4.9) and the formation of a local electric field gradient is key to EMD.

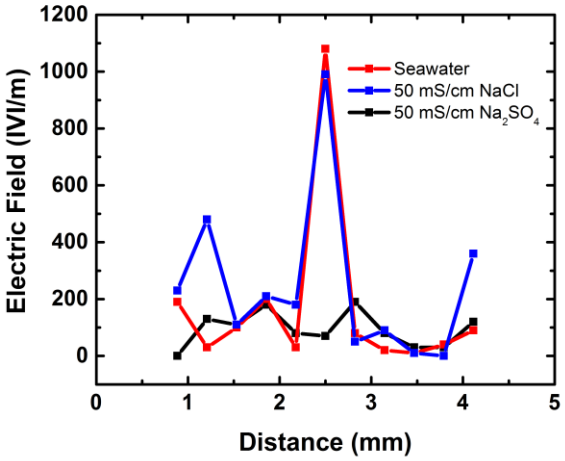

Figure 4.6:

Axial electric field measurements in the desalination channel with a 3.0 V bias between the desalination and auxiliary channels when filled with seawater (red trace), 50 mS/cm NaCl (blue trace), and 50 mS/cm Na_2SO_4 (black trace).

Numerical Simulations

Numerical simulations following the procedure described in the Experimental Section were used to confirm our proposed mechanism for desalination. The simulations mirror the experiment corresponding to Figure 4.5d: desalination of a 50 mS/cm NaCl solution with the assumption of Cl^- oxidation at the BPE anode. Figure 4.7a shows the simulated distribution of salinity in the region of interest close to the BPE anode, normalized by its value in the desalination channel inlet. The developed electric field gradient, illustrated by Figures 4.7b and c, directs ions toward the brine stream, resulting in a 20% reduction of salinity in the

desalted stream. This result is in excellent agreement with the experimental findings (~25±5% salt rejection). Simulated axial electric field measurements (Figure 4.7b) in 50 mS/cm NaCl reveal a peak field of ~14 kV/m, while the experimental measurement shown in Figure 4.6 is lower: ~1.0 kV/m. However, when the simulated electric field strength is averaged over the same distance (323 μm) used in the experimental measurement, the simulated value, ~2.5 kV/m, is much closer to the measured value.

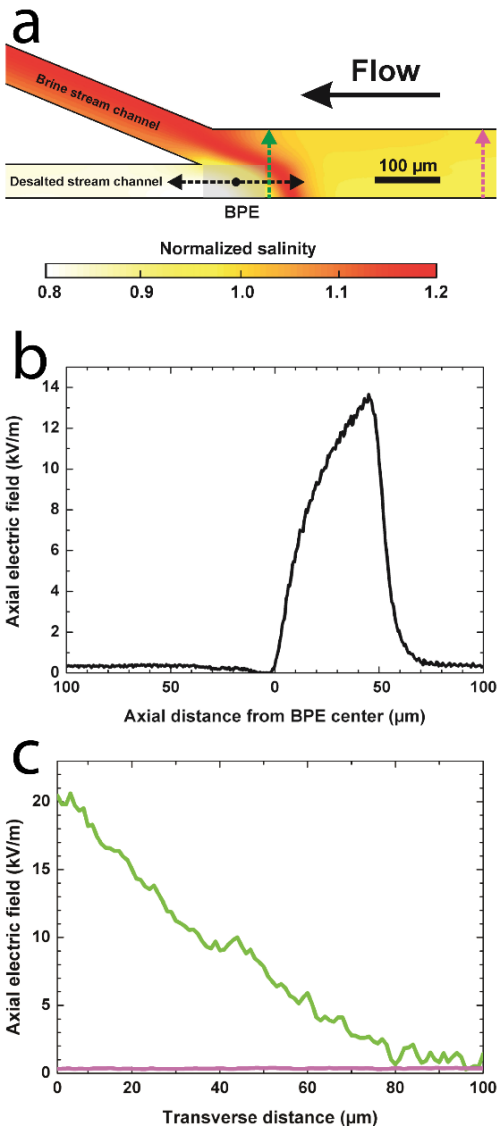

Figure 4.7:

(a) Local salinity distribution simulated for a 50 mS/cm NaCl solution with E_{tot} = 3.0 V and a total PDF rate of 0.08 μL/min from inlet to outlets; the current through the BPE is 50 nA. (b) Simulated profile of the axial electric field strength along the centerline of the desalted stream (as indicated by the black arrows in panel (a)). (c) Simulated profiles of the axial electric field strength along the transverse direction of the desalination channel (as indicated by the green and purple arrows in the corresponding color in panel (a)).

Energy Efficiency Calculations

Figure 4.8 shows a representative plot of total current through the device vs time. The steady-state operating current was 20 nA (device-to-device variation was 10-80 nA) with E_{tot} = 3.0 V driving the desalination process, hence yielding a power consumption of 60 nW. The average flow rate of desalted water was ~0.04 µL/min, resulting in an energy efficiency of just 25 mWh/L for 25±5% salt rejection at a 50% recovery. Thus, this device compares competitively with efficient, state-of-the-art seawater desalination technologies, such as RO, which typically operates at ~2000 mWh/L (~99% salt rejection, 50% recovery) for a process that requires a theoretical minimum energy of ~1000 mWh/L.[87] Note that these RO efficiencies do not include the energy associated with seawater intake, pre-treatment required to maintain membrane performance, or post-treatment. Importantly, RO efficiency improves as the scale of the process is increased to incorporate energy recovery systems,[101] and therefore the energy required to run small-scale RO desalination is higher than 2000 mWh/L. This suggests that EMD, powered by a 3.0 V battery pack, could be competitive for small-scale applications and have utility in resource-limited settings.

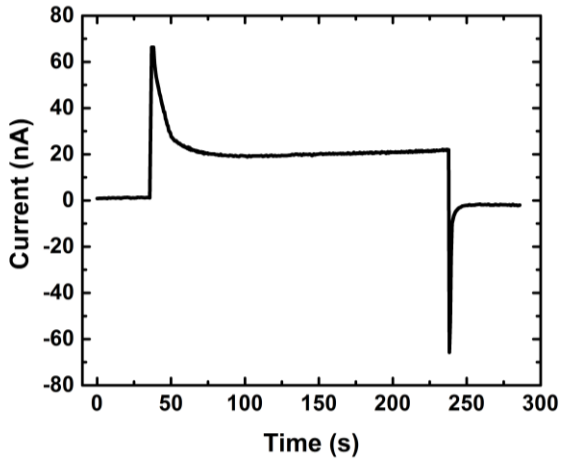

Figure 4.8:

A plot of total current vs time during a seawater desalination experiment showing the steady-state operating current of 20 nA required to drive desalination. Both microchannels were filled with seawater. E_{tot} = 3.0 V was applied and the total PDF was ~0.08 µL/min.

The fundamental operating principles of EMD are different than those of membrane and thermal desalination technologies. For example, membrane-based desalination requires an applied pressure greater than the high osmotic pressure of seawater (~30 atm) to desalt. With regard to thermal desalination, sufficient energy must be provided to vaporize water. In both cases, there are clearly defined minimum energy requirements. EMD requires only enough energy to oxidize a sufficient amount of the total Cl^- present in seawater to form the local electric field gradient.

The amount of Cl^- oxidized during these experiments is calculated assuming all current passing through the BPE anode

goes toward Cl^- oxidation, eq 4.13, where i is current and t is time, can be used to calculate the charge passed through the BPE anode (Q_{passed}).

(4.13) $Q_{passed}=it$

From the plot of total current vs time (Figure 4.8), the steady state current of the device is 20 nA. For a 50 s duration, the charge passing through the BPE anode can be calculated using eq 4.13, which yields $Q_{passed} = 1 \times 10^{-6}$ C. To calculate the total charge associated with Cl^- present in the seawater ($Q_{present}$), eq 4.14 is employed, where n is the number of electrons involved in the redox process, F is Faraday's constant (96,485 C/mol), and N is the moles of Cl^-.

(4.14) $Q_{present}=nFN$

Following eq 4.9, Cl^- oxidation is a 2 electron process, therefore n=2. The volume of seawater solution passing through the microchannel during a 50 s duration can be calculated by multiplying 50 s by the total volumetric flow rate through the device (~0.08 µL/min or 1.33×10^{-12} m^3/s). Knowing the concentration of Cl^- in seawater (0.55 moles/L) then allows the number of moles of Cl^- passing through the microchannel during a 50 s duration to be calculated (N =

3.67 x 10^{-8} moles Cl^-). Using n, F, and N, the charge present from Cl^- is found to be $Q_{present}$ = 7 x 10^{-3}. Finally, dividing Q_{passed} by $Q_{present}$ reveals that only ~0.01% of the total Cl^- present in solution is oxidized at the BPE anode when assuming all current passing through the BPE anode goes toward Cl^- oxidation.

EMD does require PDF and therefore we must consider the energy necessary to produce PDF in the energy efficiency of EMD. To verify laminar flow in these microfluidic devices, the Reynolds number was solved using eq 4.15, where ρ = density, V = linear flow velocity, h = channel height, w = channel width, and η = dynamic viscosity. With the constants[88] ρ = 1.023 g cm^{-3} and η = 0.966 mPa·s for 35% seawater at 25 °C, the

$$\mathrm{Re} = \frac{\rho V \dfrac{2hw}{(h+w)}}{\eta} \qquad (4.15)$$

$$\mathrm{Re} = \frac{(1023\,\mathrm{kg\,m^{-3}})(6.07 \times 10^{-4}\ \mathrm{m\,s^{-1}})\dfrac{2\,(2.2 \times 10^{-5}\ \mathrm{m})(1.0 \times 10^{-4}\ \mathrm{m})}{(2.2 \times 10^{-5}\ \mathrm{m} + 1.0 \times 10^{-4}\ \mathrm{m})}}{9.66 \times 10^{-4}\ \mathrm{kg\,m^{-1}\,s^{-1}}} = 2.3 \times 10^{-2}$$

calculated Reynolds number is 2.3 x 10^{-2}, indicating laminar flow through a rectangular channel.[166] Because seawater is nearly incompressible, the Poiseuille equation for pressure driven laminar flow in a rectangular channel (eq 4.16)[167] can

be used to solve for the pressure drop across the microchannel, where Q = volumetric flow rate, η = dynamic viscosity, L = channel length, h = channel height, and w = channel width. This equation assumes the ratio (h/w) approaches 0.

(4.16) $$\Delta P = \frac{12Q\eta L}{h^3 w}(1 - 0.630\frac{\mathrm{h}}{\mathrm{w}})^{-1}$$

$$\Delta P = \frac{12\,(1.33\times10^{-12}\ \mathrm{m^3\,s^{-1}})\,(9.66\times10^{-4}\ \mathrm{kg\,m^{-1}\,s^{-1}})\,(0.005\,\mathrm{m})}{(2.2\times10^{-5}\ \mathrm{m})^3\,(1.0\times10^{-4}\ \mathrm{m})}(1-0.630\frac{2.2\times10^{-5}\ \mathrm{m}}{1.0\times10^{-4}\ \mathrm{m}})^{-1} = 84.4\,\mathrm{kg\,m^{-1}\,s^{-2}}$$

Again, with ρ = 1.023 g cm^{-3} and η = 0.966 mPa·s for 35% seawater at 25 °C,[88] ΔP = 84.4 kg m^{-1} s^{-2}. The energy required to drive the PDF can be calculated by taking the pressure drop across the microchannel times the volumetric flow rate (eq 4.17).

(4.17) $$\text{Energy for PDF} = (\Delta \mathrm{P} \times \mathrm{Q})$$

$$\text{Energy for PDF} = (84.4\,\mathrm{kg\,m^{-1}\,s^{-2}} \times 1.33\times10^{-12}\ \mathrm{m^3\,s^{-1}}) = 1.12\times10^{-10}\ \mathrm{W}$$

The power consumption required to drive the PDF necessary for desalination is therefore 112 pW. The power consumption necessary to drive EMD was previously found to be 60 nW, which yielded an energy efficiency of 25 mWh/L with a desalted flow rate of ~0.04 µL/min However, to calculate the true efficiency of this device, the power associated with

PDF must also be considered. This means the actual power consumption of this desalination technique is 60.11 nW, as opposed to 60 nW. Thus, the actual energy efficiency of the device is 25.05 mWh/L, as opposed to 25 mWh/L, indicating the energy required for PDF is negligible compared to that required to drive the electrochemical reactions necessary for desalination.

Summary and Conclusions

In summary, we have demonstrated a membraneless and energy efficient technique for seawater desalination. EMD relies on the oxidation of Cl^-, which generates an ion depletion zone and local electric field gradient to direct sea salts into a brine stream. This result is important for a number of reasons. First, the technique is membraneless, and therefore does not suffer from membrane fouling or damage and does not require extensive pre-treatment prior to desalination. Second, EMD achieves energy efficiencies of 25 mWh/L for 25±5% salt rejection at a 50% recovery of desalted water (theoretical minimum energy efficiency is ~17 mWh/L). Lastly, the simple design, operation, and equipment required to perform EMD greatly reduces the capital costs associated with desalination. In the future, to increase the production of desalted water, we plan to utilize the wireless operation

of a BPE array. Moreover, we believe there is considerable room for optimization of the channel and electrode designs.

Chapter 5: Electrochemically Mediated Desalination: Establishing Guidelines to Form a Locally Elevated Electric Field by Cl^- Oxidation

Synopsis

Electrochemically mediated desalination (EMD) is an emerging technique for membraneless desalination. EMD relies on faradaic reactions at an electrode to directly generate an ion depletion zone and concomitant locally elevated electric field in a microchannel. Ions are separated from water when increased electrophoretic velocity near the depletion zone counters bulk flow such that ions are directed into a secondary stream. Accordingly, the local electric field strength (V_1) is the most important variable affecting EMD. Here, we evaluate the effect of key experimental parameters (applied voltage, solution flow rate, and Cl^- concentration) on the formation, location, and magnitude of V_1. The results demonstrate the voltage necessary to form an elevated V_1 corresponds to the onset of Cl^- oxidation, and that even at Cl^- concentrations as high as 1.5 M, the value of V_1 is sufficient for desalination. Moreover, while not strongly affecting the magnitude of V_1, bulk solution flow plays an important role in the stability and maintenance of V_1.

Introduction

Fresh water is a critical resource required to support life. However, population growth,[67] climate change,[68] contamination,[69] public policy,[70,71] and variations in water supply[76] are causing water shortages to become common occurrences. Importantly, ~96.5% of the global water supply is seawater,[77] thereby providing a nearly unlimited source of fresh water if coupled to a viable desalination technology. To begin addressing this need, we recently introduced an energy-efficient membraneless electrochemical desalination technique called electrochemically mediated desalination (EMD).[66] Here, we report on three fundamental parameters that are important for implementation of EMD.

Previously, our group showed that formation of a local electric field gradient within a microchannel containing a bipolar electrode[1] could be used to direct the movement of ions, and that this phenomenon can be used for enrichment,[52,58] separation,[60] membraneless filtration (depletion),[64] and controlled delivery.[65] Our approach relies on the principles of electrokinetic equilibrium and counter-flow gradient focusing (CFGF).[53,125] In CFGF, charged analytes enrich when their electrophoretic velocity (u_{ep}) balances against bulk fluid flow in the opposite direction. This condition is realized in microchannel regions having an elevated local electric field strength (V_1).

In addition to EMD, there are a number of other electrochemical approaches for desalination, including capacitive deionization[109] and electrodialysis.[107] However, these techniques are generally batch processes, and therefore are not efficient for large-scale desalting.[108] Ion concentration polarization (ICP),[133] which also relies on CFGF, is most analogous to EMD. In ICP, an ion depletion zone is generated, resulting in increased V_1, when a large proportion of the ionic current is carried by, most often, cations through a perm-selective material such as Nafion. ICP has been used to drive continuous separations[168-170] and desalt seawater.[112-114]

As in CFGF, EMD occurs when u_{ep} counters bulk flow such that ions are separated into a secondary stream (brine channel, Scheme 5.1a). The localized ion depletion zone and elevated V_1 near the branching channels shown in Scheme 5.1 are essential for EMD,[63,171] and is accomplished by initiating faradaic electrochemical reactions at the anode. Specifically, the principal reaction in EMD is Cl^- oxidation to $Cl_2(aq)$,[66] which results in a net decrease in ionic charge carriers near the anode and a corresponding increase in V_1.

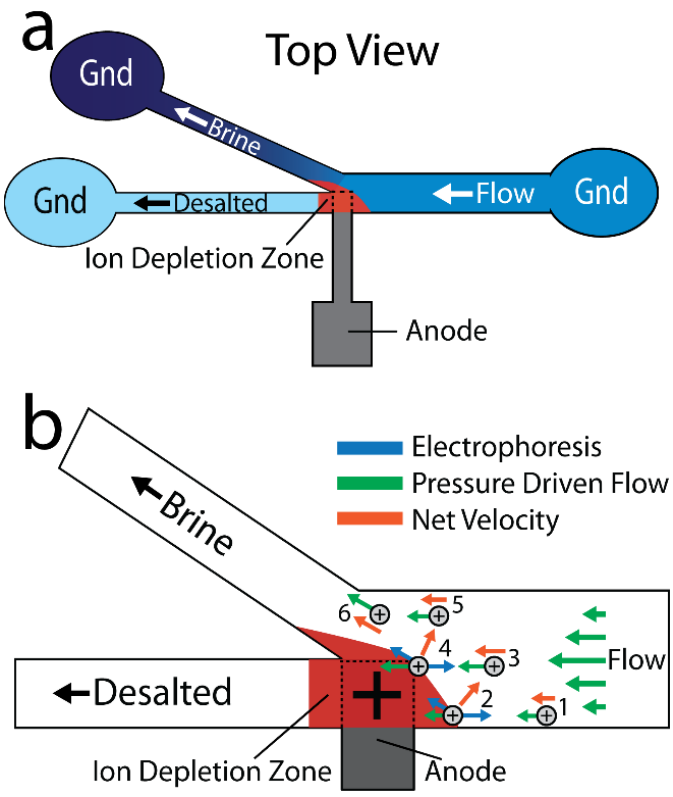

Scheme 5.1:

Schematic illustration of (a) the two-electrode microelectrochemical desalination device and (b) the region of interest near the BPE anode and ion depletion zone depicting the net velocity vectors of a cationic species under the combined forces of electrophoresis and pressure driven flow. Gnd = ground.

Clearly, the characteristics of the local electric field and its dependence on experimental variables are critical to the effectiveness of EMD. Accordingly, the work reported here is focused on how these parameters, which include the applied voltage, flow rate, and Cl^- concentration, affect the formation, location, and magnitude of V_1. The results indicate

that a threshold voltage corresponding to Cl^- oxidation must be applied to the anode before the ion depletion zone, and hence, elevated V_1, forms. Bulk flow is shown to have little effect on the magnitude of V_1, but does play an important role in the stability and maintenance of the elevated V_1. Conversely, the Cl^- concentration is important to the magnitude of V_1. Remarkably, an elevated V_1 forms at high (>0.50 M) Cl^- concentrations, and hence EMD may be suitable to partially desalt brine solutions. This is a particularly challenging type of separation for membrane-based methods because they require very high pressures to remove salts from high ionic strength solutions.[96] These findings provide fundamental insights into the physical principles affecting the ion depletion zone and corresponding V_1, and therefore establish an important foundation for understanding and optimizing the EMD process.

EXPERIMENTAL

Materials and Chemicals

Poly(dimethylsiloxane) (PDMS) channels were prepared using a silicone elastomer and curing agent (Sylgard 184) from K. R. Anderson, Inc. (Morgan Hill, CA). Pt (99.99%) and Ti (99.995%) pellets were purchased from Kurt J. Lesker Company (Jefferson Hills, PA). Glass slides (Fisherfinest)

were purchased from Fisher Scientific (Fair Lawn, NJ) and used without cleaning.

Stock solutions of NaCl and Na_2SO_4 were prepared from SigmaUltra 99.5% NaCl (Sigma-Aldrich, St. Louis, MO) and anhydrous 99% Na_2SO_4 (Acros Organics, Morris Plains, NJ), respectively, by dissolution in deionized (DI) water (>18 MΩ·cm, Milli-Q Gradient System, Millipore, Bedford, MA). A stock solution of H_2SO_4 (ACS Certified Plus, Fisher Scientific) was prepared by dilution in DI water. A stock solution of 1,1'-ferrocenedimethanol (FcDM, 98%, Acros Organics) and KNO_3 (primary nitrogen standard, Fisher Scientific) was prepared by dissolution in DI water. Ethanol (200 proof, anhydrous) was purchased from Pharmco-Aaper (Brookfield, CT) and used without further purification.

Device Fabrication

Microfabricated 100 nm-thick Pt electrodes atop a 10 nm-thick Ti adhesion layer were prepared as follows. AZ 1518 photoresist (AZ Electronic Materials, Somerville, NJ) was spin coated onto glass slides at 500 rpm for 10 s, then 3500 rpm for 45 s, and finally 500 rpm for 5 s before being soft baked at 100 °C for 45 s. A mask aligner (Süss MicroTec, Garching, Germany) and a 25,400 DPI transparency photomask (CAD/Art Services, Brandon, OR) were used to achieve a desired electrode pattern on the substrate. Figure 5.1a shows

the mask design. Figure 5.1b is an expanded view of the region in the vicinity of the anode. The twelve 60 µm-wide microband electrodes, spaced 251 µm apart (center-to-center), depicted in Figure 5.1b were used for electric field measurements. The 100 µm-wide anode generated the local electric field and was used for making electrochemical flow rate measurements.[172] A 100-µm wide collector electrode was used for flow rate measurements. Pt contact pad electrodes were used as counter electrodes in two-electrode experiments.

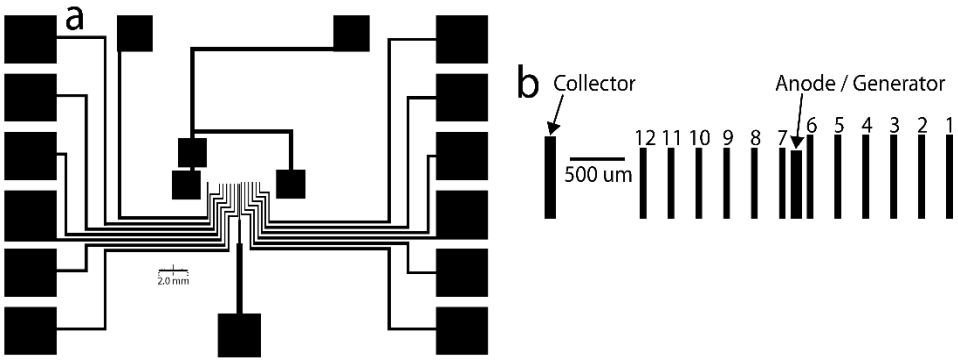

Figure 5.1:

(a) Schematic illustration of the device design used to measure the electric field and monitor flow rates. (b) Expanded view of the device design in the vicinity of the anode.

The UV lamp intensity was 6.5 mW/cm^2 and the exposure time was 15.4 s. The substrates were then developed for approximately 13 s using AZ 400K developer (AZ Electronic Materials) diluted 1/4 (v/v) with DI water. The patterned

photoresist substrates then underwent electron beam deposition. A 10 nm-thick Ti adhesion layer was deposited onto the glass followed by a 100 nm-thick Pt layer. Lift-off of the excess metal was performed in a sonicated acetone bath for 5 min. Finally, the devices were rinsed with acetone and then ethanol before being dried under N_2.

The procedure for assembling PDMS/glass microfluidic devices has been previously published.[134] Briefly, however, the PDMS microchannel (5.0 mm-long, 22.0 µm-tall, 100 µm-wide main channel, and 50.0 µm-wide brine and desalted channels) was fabricated using an SU-8 2025 (MicroChem, Newton, MA) mold patterned on a Si wafer (University Wafer, South Boston, MA). A 1.2 mm-diameter inlet and two 3.0 mm-diameter outlets were punched through the PDMS using Miltex biopsy punches (Ted Pella, Redding, CA). The PDMS channel was rinsed with ethanol and dried under N_2 before the PDMS and glass surfaces were exposed to a 10.5 W O_2 plasma (PDC-32G, Harrick Scientific, Ossining, NY) for 45 s. The channel and glass slides were then bound together with the anode extending 50 µm into and aligned upstream of the bifurcated channel (Scheme 5.1a). The microfluidic device was then placed in an oven at 65° C for 5 min to promote irreversible bonding between the glass and PDMS.

Flow Rate Measurements

The purpose of the flow rate measurements was two-fold. First, to ensure that the syringe pump was delivering the desired volumetric flow. Second, to determine the minimum volumetric flow rate that could be reliably delivered. Flow rates through the microchannel were monitored electrochemically by driving an electrochemical reaction on the upstream generator electrode and the product of this reaction then flows to a downstream collector electrode where the reverse redox reaction occurs (Scheme 5.2).[152,172] The linear flow velocity is calculated by dividing the distance between the generator and collector electrodes (2.07 mm, edge-to-edge) by the time required for the product to reach the collector electrode. The linear velocity is converted to a volumetric flow rate using the cross-sectional area of the desalted channel.

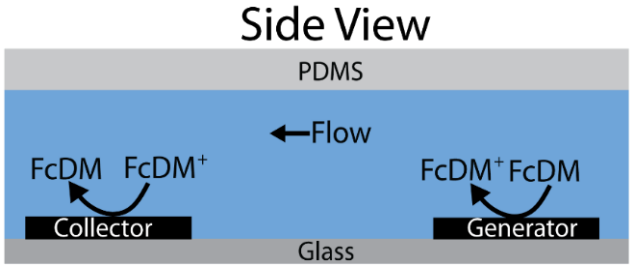

Scheme 5.2:

Schematic illustration of the flow rate measurement showing oxidation of FcDM to $FcDM^+$ at the upstream generator electrode followed by reduction of $FcDM^+$ to FcDM at the downstream collector electrode.

The flow rate experiments were carried out using a solution containing 0.50 mM 1,1'-ferrocenedimethanol (FcDM) and 0.10 M KNO_3 in DI water (18 MΩ·cm, Millipore). The solutions were not deaerated. A syringe pump (Harvard Pico Plus Elite, Harvard Apparatus, Holliston, MA) was used to provide pressure driven flow (PDF) through the channel. Following a previously published procedure,[173] two syringes (500 and 50 µL luer lock gas-tight syringes, Hamilton, Reno, NV) were used to rinse the channel and deliver flow, respectively. Both syringes were filled with the same solution. A low-pressure switching valve (V-101L, IDEX Health & Sciences, Oak Harbor, WA) was employed to quickly switch between syringes. Fittings and PEEK tubing (500 µm I.D.) from IDEX were used to connect to the 1.2 mm inlet. Before each experiment, the flow rate was set to 1.0 µL/min to rinse the device for 5 min. Next, flow was set to the desired rate and allowed to equilibrate for 5 min before initiating data collection. The accuracy of the flow rates was validated using a previously described electrochemical procedure.[152,172]

Electrochemical data were collected using a three-electrode cell configuration and a bipotentiostat (CHI700E, CH Instruments, Austin, TX). The two microfabricated 100 µm-wide Pt electrodes (Figure 5.1b) were both configured as working electrodes in the microchannel, and a 1 mm-diameter leakless Ag/AgCl reference electrode (Innovative

Instruments, Tampa, FL) and Pt wire auxiliary electrode (CH Instruments) were placed in the desalted reservoir (Scheme 5.1a). Generation-collection flow rate measurements were performed using procedures previously described by our group.[173] The generator electrode was set to execute a 10 s potential step from 0.125 V to 0.675 V vs Ag/AgCl. The collector electrode was set to 0.125 V vs Ag/AgCl throughout the course of the experiment. The quiet time for each experiment was 10.0 s and the sampling interval was 0.0050 s.

After setting the flow rate, electrochemical data were collected in triplicate and averaged. Figure 5.2 shows typical current vs time responses at the collector electrode for flow rates ranging from 50 to 100 nL/min. The data has been normalized to the maximum collector current measured. Note the current at t = 0 is not 0 because the oxygen reduction reaction proceeds at the potential of the collector electrode. When $FcDM^+$ reaches the collector (~2-4 s), the current increases due to reduction of $FcDM^+$ formed at the generator. Flow rates measured electrochemically varied with expected flow rates based on the syringe pump setting by no more than 10%. As the flow rate increases, the $FcDM^+$ transit time decreases (Figure 5.2). Flow rates below 50 nL/min could not be accurately maintained.

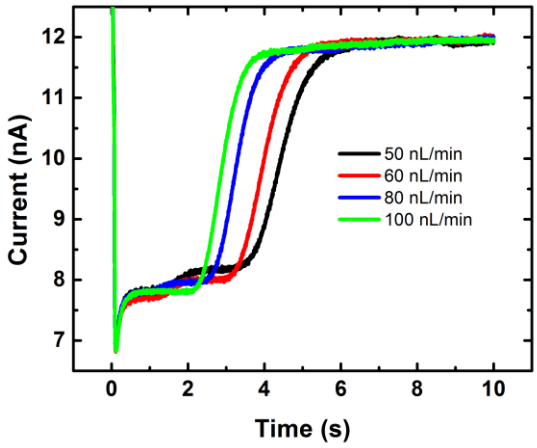

Figure 5.2:

Plot of collector current vs time for a generation-collection experiment carried out at flow rates between 50 and 100 nL/min. The solution contained 0.50 mM FcDM and 0.10 M KNO_3. The collector electrode was held at 0.125 V vs Ag/AgCl while the generator electrode was stepped from 0.125 V to 0.675 V vs Ag/AgCl. The potential step lasted 10 s.

Electric Field Measurements

The axial electric field along the centermost 2.5 mm of the 5.0 mm-long microchannel was monitored using a scanning digital multimeter (SDMM, Model 2700, Keithley Instruments, Cleveland, OH) equipped with a multiplexer module (Model 7701, Keithley). Axial electric field measurements were obtained using the device design shown in Figure 5.1. The microbands extended from below the PDMS monolith to expose a Pt contact pad allowing connection to a breakout board and SDMM. Ohmic connections to the contact pads were made with

Au-coated pogo pins embedded in a custom acrylic device holder (Figure 5.3).

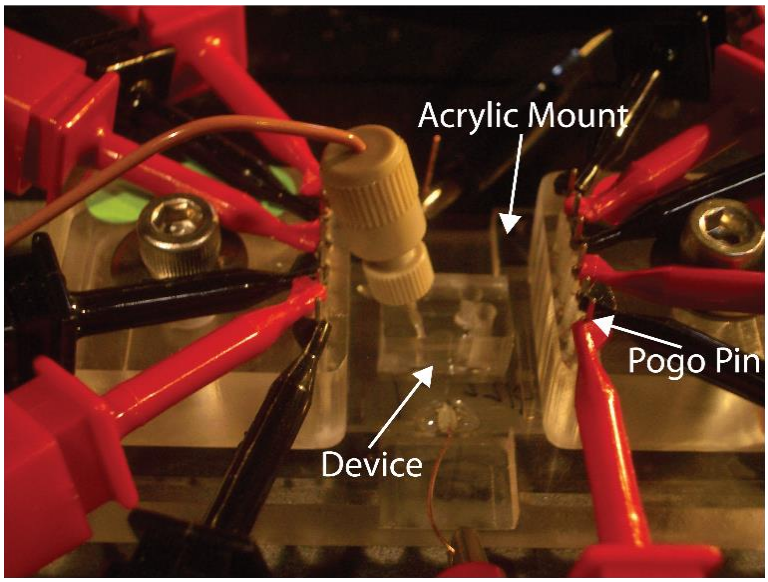

Figure 5.3:

Photograph of the custom device holder containing twelve pogo pins for connection to the Pt microband contact pads.

Measurement of the electric field proceeded as follows. Using the previously described procedure, the channel was rinsed and the flow rate set to 100 nL/min. At 2.0 s intervals, the SDMM was triggered to collect data scans consisting of eleven voltage measurements made between the twelve sequential Pt microbands. Data were collected for a total of ~180 s. The data acquisition time for each voltage measurement between pairs of neighboring Pt microbands was ~0.1 s. Measurements started with the most upstream

microbands and proceeded in the downstream direction. Devices were monitored optically with a top-down microscope (AZ100, Nikon, Tokyo, Japan) fitted with a CCD camera (QuantEM: 512SC, Photometrics, Tucson, AZ).

The SDMM collected the voltage difference sequentially between microbands starting with microbands 1 and 2, followed by 2 and 3, and so forth. Voltage measurements were converted to an average electric field by dividing the measured voltage by 251 μm (the distance between microband electrodes). Figure 5.4 is a representative plot of the axial electric field strength vs distance across the 5.0 mm-long microchannel after application of 1.3 V between the anode and the grounded electrodes in the reservoirs. The solution contained 0.50 M NaCl. Note the electric field in the range of 2.5 to 3.7 mm, corresponding to measurements obtained between microbands 1 to 7, is negative, while the field in the range of 1.2 to 2.5 mm, corresponding to measurements obtained between microbands 7 to 12, is positive. The reason that both positive and negative electric fields are measured is because voltage is dropped from the anode at the channel center to the grounded reservoirs at the periphery of the microchannel. Hence, the voltage at microband 1 is lower than the voltage at microband 2. Therefore, the voltage difference measured between microbands 1 and 2 is negative. This is true until the measurement is made between microbands 7 and 8. This effect

has been reported previously.[131,136] Therefore, to improve clarity, the electric field strengths are plotted as the absolute value of the electric field. If the measurements were made starting with microband 12 instead of microband 1, the signs would all be reversed.

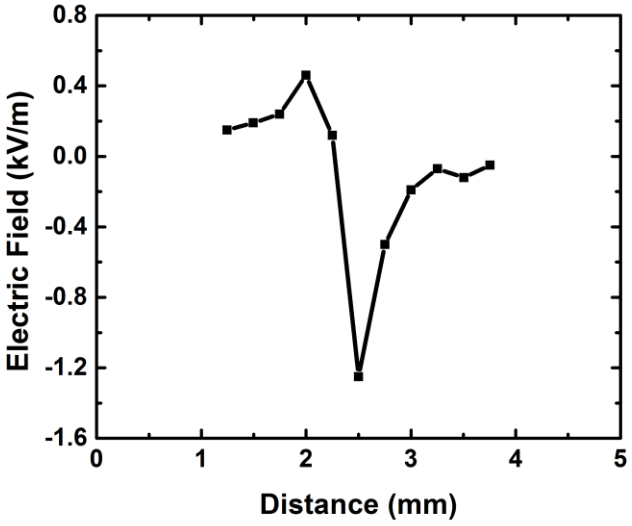

Figure 5.4:

Plot of the electric field vs distance along the 5.0 mm-long microchannel. A 1.3 V bias was applied between the anode and the electrodes in the three reservoirs. The solution contained 0.50 M NaCl and the flow rate was 100 nL/min. The inlet is centered at 5.0 mm, the 100 µm-wide anode is centered at 2.5 mm, and the desalted reservoir is at 0.

Cyclic Voltammetry

Cyclic voltammograms (CVs) were collected on-chip in a three-electrode cell configuration using a bipotentiostat (CHI700E, CH Instruments). The microfabricated Pt anode served as the working electrode, with a 1 mm-diameter

leakless Ag/AgCl reference electrode (Innovative Instruments) and Pt wire auxiliary electrode (CH Instruments) placed in the desalted channel outlet (Scheme 5.1a). Voltammograms were collected at 100 mV/s between -0.3 and 1.3 V vs Ag/AgCl at a flow rate of 100 nL/min. Solutions were not deaerated.

Results and Discussion

Principles of Electrochemically Mediated Desalination

EMD is an emerging technique for driving continuous membraneless separations. The method is based on our previous finding that charged analytes may be enriched in the vicinity of a local electric field near a bipolar electrode.[2,3] In that work, the concentration of ionic charge carriers in solution was reduced by neutralizing a buffer with the products of water electrolysis.[59,63] For EMD, however, an elevated V_1 forms as a result of direct faradaic reactions near an anode (Scheme 5.1a). More specifically, Cl^- oxidation (eq 5.1) results in a net decrease in charge carriers.[66] This in turn results in a region of high solution resistance termed the ion depletion zone. Within this zone, an increased voltage drop results in a measureable increase in V_1. As the solution resistance within the ion depletion zone increases relative to the bulk solution resistance, V_1 increases as well.[59] Importantly, only

a small percentage (~0.01%) of Cl^- present in, for example, a ~0.50 M NaCl solution must be oxidized to form an ion depletion zone having sufficient magnitude for EMD to proceed.[66]

(5.1) $$2Cl^- - 2e^- \leftrightarrow Cl_2$$

(5.2) $$2H_2O - 4e^- \leftrightarrow O_2 + 4H^+$$

(5.3) $$2H_2O + 2e^- \leftrightarrow H_2 + 2OH^-$$

It is important to note that H_2O oxidation (eq 5.2) can proceed at potentials sufficiently high to oxidize Cl^-. However, Cl^- oxidation is the primary faradaic reaction occurring in solutions with Cl^- concentrations near 0.50 M, and therefore H^+ generation does not compromise the ion depletion zone.[164] While Cl^- oxidation is the dominant reaction at the anode, the corresponding reduction reaction at the three grounded Pt electrodes in the reservoirs (Scheme 5.1a) is H_2O reduction (eq 5.3). For EMD, this reaction is not important.

In all regions of the desalination channel depicted in Scheme 5.1a, except near the ion depletion zone, ionic transport is dominated by pressure driven flow (PDF), which results in a net movement of ions toward the outlets. Importantly, there is no electroosmotic flow (EOF) in this device configuration because voltage is applied between the

channel center and peripheral reservoirs. That is, O_2 plasma-treated PDMS has negatively charged walls, and therefore the direction of EOF is from the anode to the grounded cathodes.[135] However, the absence of a fluid reservoir at the channel center prevents EOF.

The electrophoretic velocity (u_{ep}) of an ion is governed by eq 5.4, where μ_{ep} is its electrophoretic mobility. PDF directs ions toward the depletion zone, but in that vicinity, ions experience an increased u_{ep} because of its proportionality with V_1. EMD is achieved when u_{ep} counters PDF such that ions are separated into a secondary stream (Scheme 5.1b).

$$u_{ep} = \mu_{ep} V_1 \tag{5.4}$$

For example, consider Na^+, the most abundant cation in seawater,[88] approaching the ion depletion zone opposite the brine stream as depicted in Scheme 5.1b(1). Initially Na^+ does not encounter the increased V_1, and therefore its movement is dominated by PDF. As Na^+ begins to enter the depletion zone (Scheme 5.1b(2)), however, its u_{ep} toward the grounded reservoirs becomes increasingly strong until Na^+ is directed away from the depletion zone and toward the channel center. At this point (Scheme 5.1b(3)), the V_1 is low and PDF once again dominates transport, causing Na^+ to move back

toward the depletion zone. Here, the V_l and u_{ep} are high, resulting in Na^+ again being directed away from the anode (Scheme 5.1b(4)). Finally, Na^+ enters the brine stream flow path where PDF dictates its trajectory (Scheme 5.1b(5-6)). To maintain electroneutrality, anions are also directed into the brine stream.[58,111,174] The important point is that EMD is achieved by driving Cl^- oxidation at the anode, and this results in formation of an ion depletion zone and concomitant elevated V_l allowing for continuous separation of ions without the need for a physical membrane.

Electric Field Measurements

The formation of an ion depletion zone and increased V_l are responsible for the efficacy of EMD, and therefore it is critical to measure and correlate the formation, location, and magnitude of V_l to changes in experimental variables. The device configuration used for these measurements is shown in Figure 5.5a. The anode extends halfway (50 µm) into the main channel (Figure 5.5b) just before it splits into the desalted and brine channels, which are indicated by dashed white lines in Figure 5.5b. To measure the axial electric field adjacent to the anode, six microband electrodes are placed on either side of the anode (just half of these are shown in Figure 5.5b).

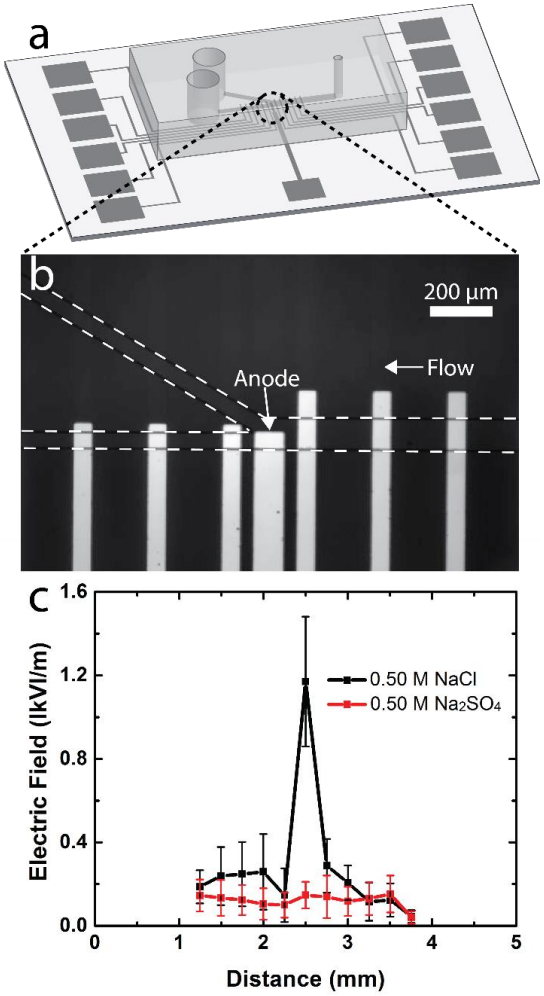

Figure 5.5:

(a) Schematic illustration of the microelectrochemical device used to measure the axial electric field. (b) Optical micrograph of the branching channel region where the anode and surrounding microbands (used for electric field measurements) are located. (c) Plots of average electric field strength vs distance across the 5.0 mm-long microchannel for 0.50 M NaCl (black trace) and 0.50 M Na_2SO_4 (red trace) solutions. A 1.3 V bias was applied between the anode and the electrodes in the reservoirs (Scheme 5.1). Each error bar represents the standard deviation of measurements made over a period of ~180 s. The inlet is centered at 5.0 mm, the 100 µm-wide anode is centered at 2.5 mm, and the desalted outlet is at 0. The flow rate was 100 nL/min.

To eliminate the possibility of an ion depletion zone forming due to indirect neutralization of buffering species present in seawater,[62] we used a 0.50 M NaCl solution for these experiments. This solution choice ensures that formation of an ion depletion zone, and associated increase in V_1, corresponds only to direct electrochemical neutralization of Cl^- (eq 5.1) at the anode. Moreover, 0.50 M NaCl is close to the Cl^- concentration in seawater (0.56 M), so it is a good proxy.[88] Well-controlled PDF is essential for these experiments, so the syringe pump set-up described in the Experimental Section was used to control flow. Before making measurements, the channels were rinsed with 0.50 M NaCl for 5 min at a 1.0 µL/min flow rate, the flow rate was reduced to 100 nL/min, and the system was allowed to equilibrate for an additional 5 min before data collection was initiated.

Next, a 1.3 V bias, which is sufficiently high for Cl^- oxidation, was applied between the Pt anode and electrodes present in each of the three reservoirs. As shown by the black trace in Figure 5.5c, this results in an immediate increase in V_1 only above the anode. With reference to the horizontal axis, the inlet is centered at position 5.0 mm, the 100 µm-wide anode is centered at 2.5 mm, and the desalted outlet is at 0. The error bars represent the standard deviation of all the measurements made between pairs of

electrodes for a single ~180 s experiment. The outcome of an important control experiment is shown by the red trace in Figure 5.5c. Here, an experiment identical to that described in the presence of NaCl was carried out, but now using 0.50 M Na_2SO_4. In this case, H_2O oxidation (eq 5.2) is the only reaction that can occur at the anode, and therefore an ion depletion zone does not form and there is no increase in V_1. These results demonstrate Cl^- oxidation is essential to the formation of an ion depletion zone and elevated V_1.

Effect of Potential Bias on Formation of the Ion Depletion Zone

To correlate the onset of Cl^- oxidation and formation of the ion depletion zone with an elevated V_1, we performed cyclic voltammetry (CV) experiments in solutions containing Cl^- present at different concentrations. In addition, electric field strength measurements as a function of the anode potential were carried out. All of these experiments were done using the three-electrode microelectrochemical configuration described in the Experimental Section. The viability of making three-electrode measurements in the microfluidic device was confirmed by the CV results in Figure 5.6, which show characteristic Pt electrochemistry in a 0.10 M H_2SO_4 solution exhibiting Pt oxidation and oxide reduction waves, as well as the peaks corresponding to hydride

adsorption and desorption.[175] The increased baseline current near 0 V is due to the oxygen reduction reaction.

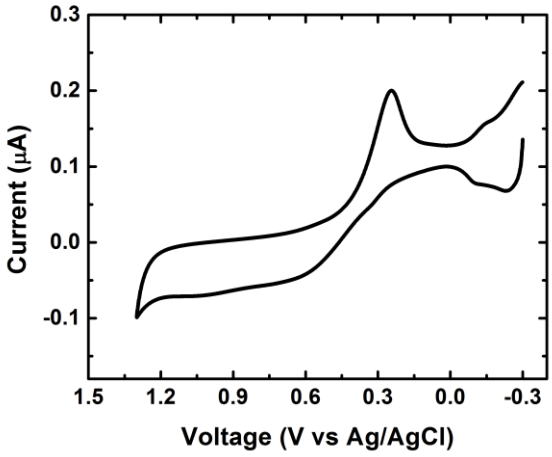

Figure 5.6:

CV obtained in a solution containing 0.10 M H_2SO_4. The working electrode was a 100 μm-wide microfabricated Pt anode. The reference electrode and Pt wire auxiliary electrode were placed in the reservoir of the desalted channel. The solution was not deaerated. The scan started at -0.3 and was reversed at 1.3 V. The scan rate was 100 mV/s.

The CVs in Figure 5.7a demonstrate that addition of Cl^- causes the characteristic peaks (Pt oxidation, oxide reduction, and hydride adsorption and desorption) associated with Pt electrochemistry in H_2SO_4 to change (compare to the black trace obtained with no Cl^- present).[176,177] More importantly, the presence of Cl^- (e.g., green trace) causes the onset potential for anodic current to shift to more negative potentials, thereby demonstrating that Cl^- oxidation

(eq 5.1) is more favorable than H_2O oxidation (eq 5.2) under the conditions used in our experiments.

To confirm that the onset of Cl^- oxidation results in an increase in V_1, we measured the electric field strength while varying the potential bias in 0.10 V increments. Specifically, the potential was stepped from -0.20 V, which is not sufficiently high for Cl^- oxidation, to values ranging from 0.20 to 1.60 V vs Ag/AgCl and the electric field was measured for the 30 s duration of each potential step. These experiments were carried out using 0.50 M NaCl and a 100 nL/min flow rate. The averaged results, obtained using two separate microelectrochemical devices, are shown in Figure 5.7b. The error bars represent the pooled standard deviation. As mentioned earlier, these experiments are focused on the channel region in the immediate vicinity of the anode (2.5 mm, Figure 5.5c), and therefore the V_1 values plotted in Figure 5.7b are those at this location. The data establish there is a threshold voltage required to form the ion depletion zone and elevated V_1. This voltage is 1.2 V vs Ag/AgCl, which corresponds well to the onset for Cl^- oxidation recorded in the CVs (dashed line, Figure 5.7a). Importantly, these results demonstrate the onset of Cl^- oxidation is key to forming the elevated V_1 necessary for EMD. One final point: Figure 5.7b shows there is a minimum voltage required to generate an elevated V_1, but there is also a maximum voltage

limit (>5 V) set by the appearance of gas bubbles arising from H_2O oxidation (eq 5.2). Evolution of $Cl_2(g)$ according to eq 5.1 could also contribute to bubble formation, but it is orders of magnitude more soluble than O_2 and, as will be discussed later, reacts with water.[178,179] The establishment of these types of voltage bounds for depletion zone formation is essential for future studies aimed at improving the energy efficiency of EMD.

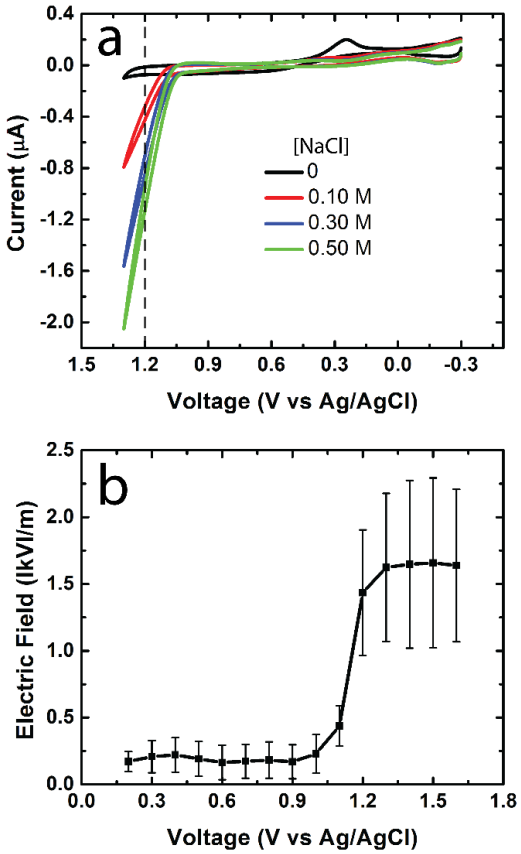

Figure 5.7:

Cyclic voltammograms (CVs) and electric field measurements obtained in the microelectrochemical device shown in Scheme 5.1a. The working electrode was a 100 μm-wide Pt anode, and a Ag/AgCl reference electrode and a Pt wire auxiliary electrode were placed in the reservoir of the desalted channel. (a) CVs obtained in 0.10 M H_2SO_4 solutions containing the concentrations of NaCl indicated in the legend. The initial and final potentials were -0.30 and 1.3 V, the scan rate was 100 mV/s, and the flow rate was 100 nL/min. Solutions were not deaerated. (b) Plot of average electric field strength above the anode vs the final potential of the working electrode. The potential was stepped from an initial value of -0.20 V to the values indicated on the horizontal axis. The microchannel was filled with 0.50 M NaCl and the flow rate was 100 nL/min. The error bars represent the pooled standard deviation for two separate devices.

The foregoing experiments were performed using a potentiostat and a three-electrode cell configuration so that the potential could be controlled vs a reference electrode. However, this type of arrangement is not practical for applications outside the laboratory. Accordingly, we performed similar experiments using a two-electrode cell and a standard power supply (Figure 5.8). Electric field measurements were carried out as follows using a two-electrode configuration with the microfabricated Pt electrode as the anode and the Pt contact pad electrodes in the three reservoirs as the cathode (Figure 5.1a). The device was rinsed with 0.50 M NaCl and the flow rate was set to 100 nL/min as described in the Experimental Section. A 0.5 to 1.5 V potential bias was then applied with a PWS4721 DC power supply (Tektronix, Portland, OR). Electric field measurements were collected for a total of ~180 s at each voltage. 2 min elapsed between each experiment. The averaged results obtained using three separate devices are shown in Figure 5.8. The error bars represent the pooled standard deviation. These experiments yielded the same sigmoidal relationship between the field and the applied voltage as those presented in Figure 5.7b. In this case, the voltage required to achieve an elevated V_1 was 0.9 V.

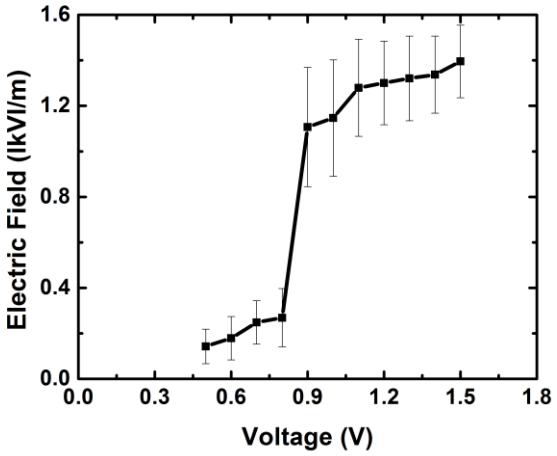

Figure 5.8:

Plot of average electric field magnitude above the anode vs potential bias for three separate devices. The microchannel was filled with 0.50 M NaCl and a 0.5 to 1.5 V bias was applied between the anode and reservoirs. Error bars represent the pooled standard deviation.

Effect of Flow Rate on the Local Electric Field Strength, Maintenance, and Location

In the previous discussion, we established Cl^- oxidation as the key to generating an increased V_1, which in turn amplifies u_{ep} near the branch point in the microchannel. We now turn our attention to the effect of flow rate on the magnitude, maintenance, and location of the V_1. These experiments were carried out using a two-electrode cell configuration and the following procedure. The device was first rinsed with 0.50 M NaCl using the method described earlier. The flow rate was then set to values between 50 and 400 nL/min and allowed to equilibrate for 5 min. Lastly, a

1.3 V potential bias was applied between the anode and electrodes in the reservoirs, while electric field data were collected for a total of ~180 s. As discussed next, there are several important outcomes from this series of experiments.

Figure 5.9a is a plot of the average V_1 above the anode as a function of flow rate for three separate devices. It shows that the magnitude of V_1 is (within error) constant over the range of flow rates examined. The error bars represent the pooled standard deviation from all experiments. This result is in contrast to previous studies from our group in which the ion depletion zones formed due to indirect buffer neutralization. In that case, small flow rate changes (~0.5 nL/min) were shown to have a significant effect on the magnitude of V_1.[57] Even in the case of the direct faradaic process here, however, it is somewhat surprising that higher flow rates don't result in transport of the ion depletion region away from the vicinity of the anode (where the data in Figure 5.9a was obtained), and hence lower V_1.[180] One likely explanation for this result is that the measurements in Figure 5.9a are obtained at the floor of the microchannel (in plane with the anode), where the solution velocity due to PDF is lowest.[166] If electric field measurements could be made throughout the height of the microchannel, the results might be different. Additionally, as discussed shortly, Cl_2(aq) reacts with water, causing the ionic strength of the

depletion zone to increase. This unavoidable increase in ionic strength limits the extent to which the depletion zone ionic strength can change relative to the bulk, thereby likely also contributing to the steady magnitude of V_1 in Figure 5.9a. Finally, as mentioned earlier, with the amount of Cl^- oxidation being very low, we did not expect the rate of oxidation to be mass transfer limited. This hypothesis was confirmed by measuring the total faradaic current as a function of flow rate (Figure 5.10). Total current measurements were collected a total of ~240 s using a 6517B Ammeter (Keithley). Figure 5.10 is a plot of the average total current collected at t = 240 s for three separate devices as a function of flow rate. The error bars represent the pooled standard deviation. These results demonstrate that, within error, the total current is constant over the indicated range of flow rates.

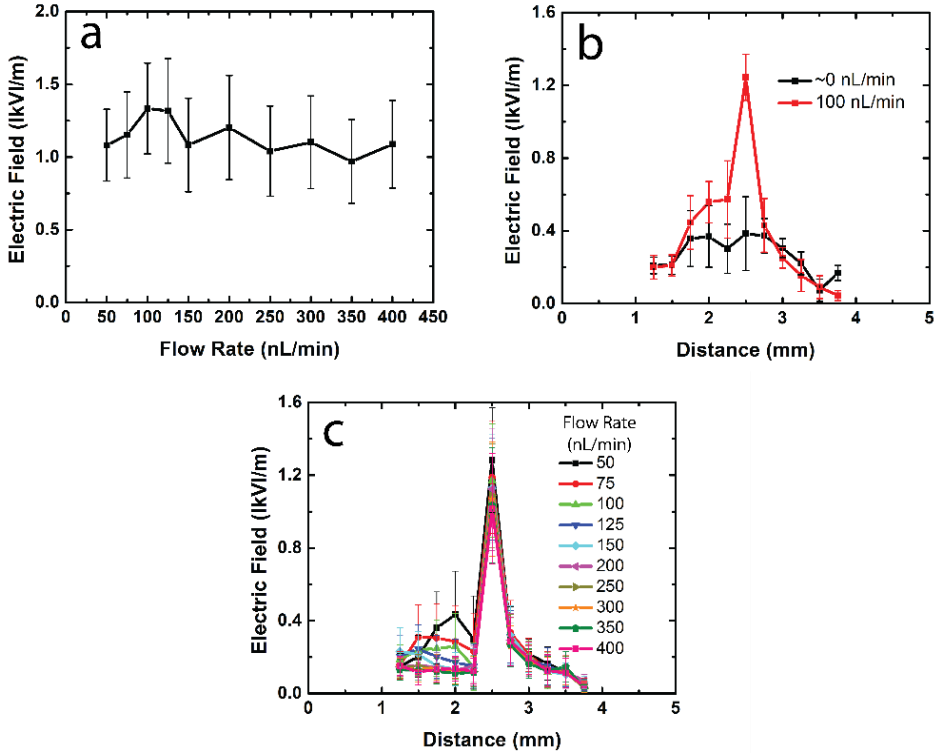

Figure 5.9:

Axial electric field measurements collected in 0.50 M NaCl with a 1.3 V bias applied between the anode and the electrodes in the three reservoirs (Scheme 5.1). (a) Plot of the average electric field strength above the anode vs flow rate. The error bars represent the pooled standard deviation for three ~180 s experiments using three independently fabricated devices. (b) Plots of average electric field strength vs distance across the 5.0 mm-long microchannel. The flow rate was set to 100 nL/min for the first 40 s of this experiment (red trace). The pump was then turned off to diminish flow for the final 140 s of the experiment (black trace). The error bars represent the standard deviation of the first 40 s and final 140 s of this experiment. (c) Plot of average electric field strength vs distance across the microchannel as a function of flow rate. Each error bar represents the standard deviation of measurements made over a period of ~180 s. For (b) and (c), the inlet is centered at 5.0 mm, the 100 µm-wide anode is centered at 2.5 mm, and the desalted outlet is at 0.

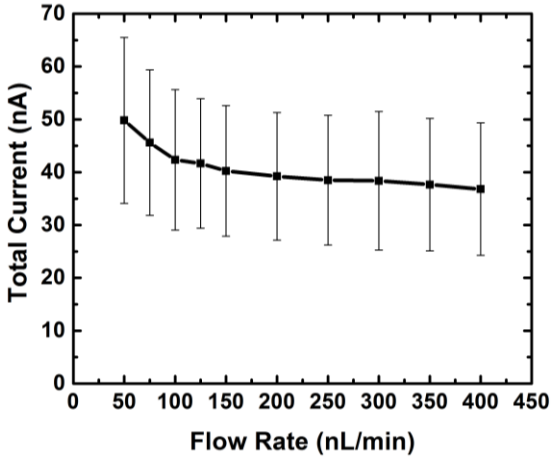

Figure 5.10:

Plot of the average total current collected at t = 240 s as a function of flow rate for three separate devices. The channel contained 0.50 M NaCl, and a 1.3 V bias was applied between the Pt anode and the electrodes in the three reservoirs. The flow rate was varied from 50 to 400 nL/min. The error bars represent the pooled standard deviation.

While Figure 5.9a indicates that flow does not significantly affect the magnitude of V_1, flow is critical to the maintenance of a stable and elevated V_1. Figure 5.9b shows a V_1 measurement collected in 0.50 M NaCl for a total of ~180 s. For the first 40 s of this experiment, the flow rate was set to 100 nL/min, and the red trace shows the average and standard deviation of the V_1 measurements during this time period. The syringe pump was then turned off to diminish flow (there is some residual flow immediately after the pump is turned off), and the black trace shows the averaged measurements during the final 140 s of the experiment

(selected individual measurements are provided in Figure 5.11).

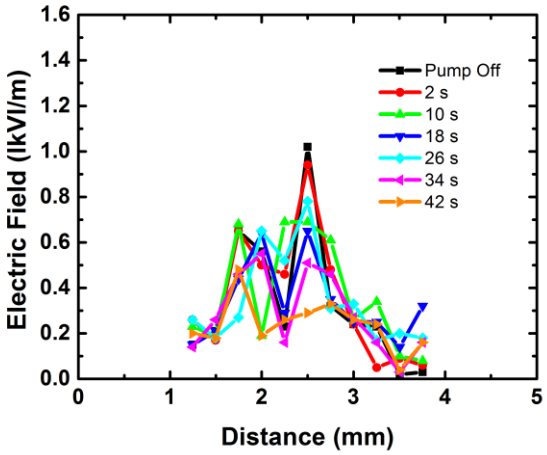

Figure 5.11:

Plot of the magnitude of the electric field vs distance along the 5.0 mm-long microchannel. The channel was filled with 0.50 M NaCl, and a 1.3 V bias was applied between the anode and electrodes in the three reservoirs. The flow rate was initially set to 100 nL/min. The pump was then turned off (black trace) to diminish flow. Selected times immediately following the syringe pump being turned off are plotted. The inlet is centered at 5.0 mm, the 100 µm-wide anode is centered at 2.5 mm, and the desalted outlet is at 0.

The results clearly show that when flow is stopped, the maximum value of V_1 above the anode decays to a value comparable to that collected in Na_2SO_4 (Figure 5.5c, red trace) where an ion depletion zone does not form. The decrease in V_1 is the result of two factors. First, Cl^- oxidation (eq 5.1) produces $Cl_2(aq)$, which rapidly undergoes hydrolysis to form HOCl and HCl (eq 5.5).[179] HCl completely dissociates and

HOCl is a weak acid that partially dissociates (pK_a = 7.5), and consequently these ions contribute to the collapse of the ion depletion zone (Scheme 5.3).[179,181] Second, with the syringe pump turned off, Cl^- oxidation proceeds by diffusion of Cl^- to the anode, but the ions generated from Cl_2(aq) hydrolysis are not transported away from the depletion zone. Consequently, the decrease in ionic strength of the depletion zone relative to the bulk is limited. When flow is reinitiated, the ion depletion zone and elevated V_1 are reestablished.

(5.5) $$Cl_2 + H_2O \leftrightarrow HOCl + HCl$$

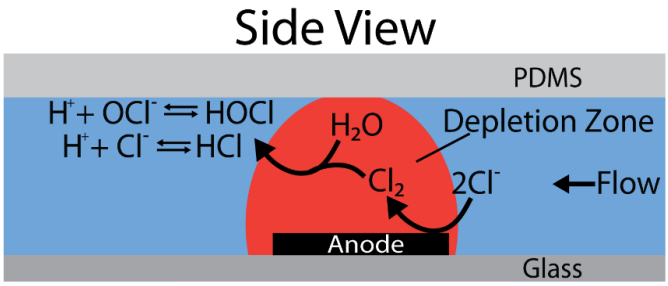

Scheme 5.3:

Schematic illustration of the depletion zone collapsing as Cl_2(aq) reacts with water to generate HCl and HOCl, which then dissociate and cause an increase in local ionic strength.

The last important finding from these flow rate studies is that the location of the ion depletion zone and maximum V_1

are not affected by flow rates spanning the range from 50 to 400 nL/min. The results of this experiment are shown in Figure 5.9c, and they differ greatly from previous studies reported by our group where V_1 was found to be highly sensitive to flow rate.[57,63]. Importantly, however, formation of the ion depletion zone in those earlier experiments relied upon indirect buffer neutralization rather than the direct faradaic process used here. For example, a change of just ~0.5 nL/min led to an easily measurable change in the position of the ion depletion zone. The insensitivity to flow rate in the present study is likely due to two factors. First, the depletion zone, and therefore the maximum V_1, forms directly at the anode rather than in solution following acid/base chemistry. Second, as previously discussed, after Cl^- is oxidized, Cl_2(aq) undergoes hydrolysis (eq 5.5) and therefore no longer contributes to ion depletion. Consequently, the depletion zone has little ability to shift with flow within the resolution of our measurements.

The results described in this section have a number of important implications for future EMD studies. First, the flow rate must be chosen judiciously to achieve maximum salt rejection. This is because the counter-flow separation mandates that a given V_1 and u_{ep} must be countered by a proportional PDF. Consequently, with the magnitude of V_1 and hence u_{ep} relatively constant as a function of flow rate,

there is a limited range of flow rates suitable for separation. When the flow rate increases past this range and PDF dominates u_{ep}, ions traverse the depletion zone. Second, although EMD requires flow to maintain an elevated V_1, the absence of a membrane lowers the resistance to mass transfer, thus reducing the energy required for flow. Third, because the location of the depletion zone and elevated V_1 is insensitive to flow but dependent on the anode position, future studies will focus on the optimal positioning and geometry of the anode.

Effect of Cl^- Concentration on the Local Electric Field Strength

Thus far, all our experiments have been performed at Cl^- concentrations near that of seawater (3.0-5.0% total salt). However, we are interested in expanding the scope of EMD beyond seawater to the desalination of lower (brackish water, 0.05-3.0% salt) and higher (brine, >5.0% salt) salinity solutions. Accordingly, we measured the electric field as a function of Cl^- concentration to understand its effect on V_1. These experiments were carried out using the following procedure. First, the syringes, tubing, fittings, and device were rinsed with the salt solution to be tested (0.001 to 0.50 M NaCl) using the method described earlier. Second, the flow rate was set to 100 nL/min and allowed to equilibrate for 5 min. Third, a 1.3 V potential bias was applied between

the anode and the three electrodes in the reservoirs while electric field data were collected for a total of ~180 s.

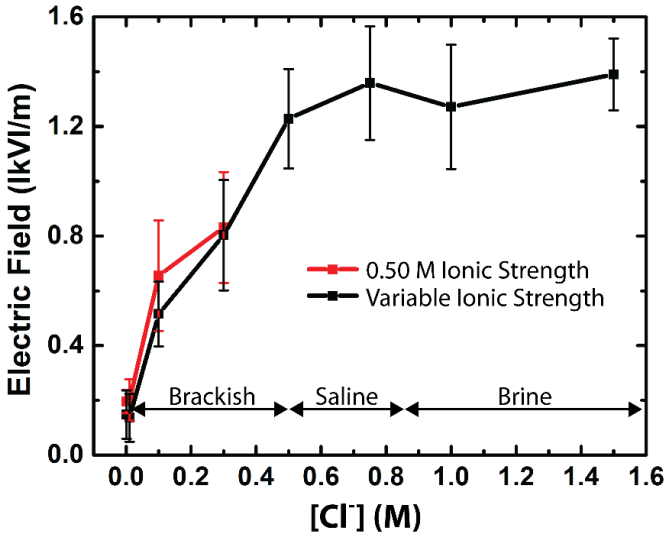

Figure 5.12:

Plot of electric field strength above the anode vs Cl^- concentration. Measurements were made with a 1.3 V bias applied between the anode and the electrodes in the three reservoirs (Scheme 5.1). The error bars represent the pooled standard deviation for ~180 s experiments using three independently fabricated devices. The microchannel was filled with 0.001 to 1.5 M NaCl at variable ionic strength (black trace) or 0.001 to 0.3 M NaCl at 0.50 M total ionic strength (red trace). Na_2SO_4 was added to fix the ionic strength in the latter case. The flow rate was 100 nL/min.

The averaged results obtained from three separate devices are plotted in Figure 5.12. The error bars represent the pooled standard deviation. The data show that at concentrations of Cl^- ranging from 0.001 to 0.30 M, the magnitude of V_1 is less than that measured in 0.50 M Cl^-. To

ensure that these measurements are not simply artifacts of the decreased ionic strength (i.e., increased solution resistance in the channel), additional experiments were carried out at the same Cl^- concentrations, but at a total ionic strength of 0.50 M. The additional salt required to fix the ionic strength at 0.50 M was Na_2SO_4 because, as shown earlier (Figure 5.5c), it does not contribute directly to the ion depletion zone and elevated V_1. The results (Figure 5.12, red trace) nearly overlay those obtained in the absence of Na_2SO_4, and therefore we conclude that solution resistance does not significantly contribute to the magnitude of V_1 in this concentration range. Note that it is possible to achieve separation at these values of V_1 in brackish water (0.10 to 0.30 M Cl^-), but this requires lower flow rates. This is because the counter-flow separation dictates that a lower V_1 and u_{ep} must be countered by a proportional decrease in PDF.

An important outcome of the experiments leading to Figure 5.12 is that at Cl^- concentrations spanning the range 0.50 to 1.5 M, which includes brine solutions, V_1 is indistinguishable from that observed using 0.50 M Cl^-. This supports the notion that it might be possible to use EMD to partially desalinate brine solutions. In contrast, membrane-based desalination of brine solutions is particularly challenging due to the high pressures required.[87]

Summary and Conclusions

In summary, we have reported on experiments intended to provide a fundamental basis for EMD. Specifically, we have evaluated the effect of three key parameters (applied voltage, solution flow rate, and Cl^- concentration) on the formation, magnitude, and location of V_1. The results are important because the nature of the V_1 is the key parameter governing EMD. The data indicate that Cl^- oxidation is required to generate an ion depletion zone, and hence achieve a sufficiently high V_1 for EMD. Another key outcome of this study is that it is possible to generate a sufficiently elevated V_1 to at least partially desalinate high-salt brine solutions. This is important because membrane-based methods require very high pressures, and correspondingly high energy costs, to achieve this result.[87] Thus, one can envision EMD being used to lower the overall ionic strength of salt water to the point that reverse osmosis becomes viable.

We previously reported that EMD, as presently configured, desalts seawater at about the 25% level (>98% desalination is required for drinking water). We have, therefore, considered the possibility of operating EMD in serial to successively reduce the salt level with each pass of the solution by an electrode and ion depletion zone. The results shown in Figure 5.12, however, temper our enthusiasm for this approach because the low V_1 generated at Cl^-

concentrations below 0.50 M may limit the throughput of this approach. Nevertheless, we plan to explore this possibility in more detail soon.

Another important outcome of this study is that the formation and magnitude of V_1 is not significantly affected by flow rate values ranging over an order of magnitude (Figure 5.9a). This is a consequence of the ion depletion zone and concomitantly elevated V_1 directly forming by Cl^- oxidation. While this result offers the promise of high energy efficiency per volume of desalinated water, our current apparatus only provides information about V_1 at the base of the fluidic channel. Undoubtedly, it would be advantageous to obtain such data perpendicular to the channel floor, perhaps using an appropriate dye and confocal microscopy.

Much work is still necessary before the viability of EMD is realized. Nevertheless, the experiments discussed here provide guidance as to both the opportunities and limitations of EMD. In forthcoming publications, we plan to use these findings to improve energy efficiency, increase salt rejection, and explore the possibility of desalinating brine solutions.

Chapter 6: Explorations in Electrochemically Mediated Desalination

Synopsis

Electrochemically mediated desalination (EMD) is an emerging technique for membraneless desalination. EMD relies on Cl^- oxidation at an electrode to directly generate a locally elevated electric field in a microchannel where ions are separated into a secondary channel when their electrophoretic velocity counters bulk fluid flow. Here, in an effort to increase the percentage of salt rejection, we modify the anode configuration driving Cl^- oxidation to increase the local electric field strength. Moreover, we explore the possibility of reducing or eliminating the electrical energy costs of EMD by driving photoelectrochemical Cl^- oxidation. Finally, we introduce on-line capacitively coupled contactless conductivity detection (C^4D) to rapidly and reliably quantify salt rejection for EMD.

Experimental

Chemicals

4,4-Difluoro-1,3,5,7,8-pentamethyl-4-bora-3a,4a-diaza-s-indacene-2,6-disulfonic acid ($BODIPY^{2-}$, Invitrogen, Carlsbad, CA) was used as a fluorescent probe of Cl^-

photooxidation. Poly(dimethylsiloxane) (PDMS) channels were prepared using a silicone elastomer and curing agent (Sylgard 184) from K.R. Anderson, Inc. (Morgan Hill, CA). Solutions of Na_2SO_4 were prepared from 99% Na_2SO_4 (anhydrous, Acros Organics, Fair Lawn, NJ) by dissolution in deionized (DI) water (18 MΩ·cm, Milli-Q Gradient System, Millipore, Bedford, MA). Solutions of NaCl were prepared from 99.5% NaCl (SigmaUltra, Sigma-Aldrich, St. Louis, MO) by dissolution in DI water. Stock solutions of H_2SO_4 and HCl (both ACS Certified Plus, Fisher Scientific) were prepared by dilution in DI water. Ethanol (200 proof, anhydrous) was purchased from Pharmco-Aaper (Brookfield, CT) and used without further purification.

Device Fabrication

All experiments in Chapter 6 were performed with PDMS microchannels (5.0 mm-long, 22.0 µm-tall, 100.0 µm-wide main channel, and 50.0 µm-wide brine and desalted channels) prepared by previously described procedures.[66] The PDMS channels were rinsed with ethanol and dried under N_2 before both the PDMS and glass or quartz surfaces having an adhered anode were exposed to an air plasma (10.5 W, model PDC-32G, Harrick Scientific, Ossining, NY) for 15 s. The two parts were then bound together with the anode extending 50 µm into and upstream of the branched microchannel (Scheme 6.1). The

device was then placed in an oven at 65 °C for 5 min to promote irreversible bonding.

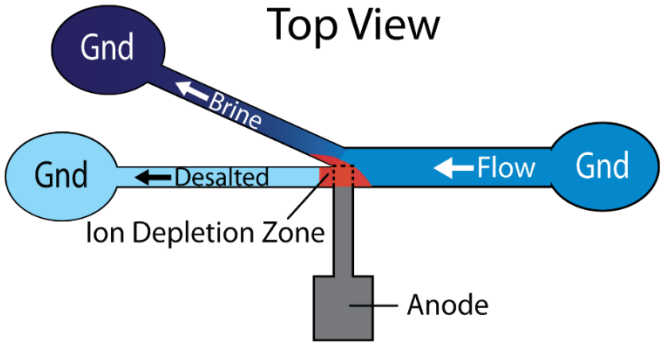

Scheme 6.1:

Schematic illustration of the two-electrode microelectrochemical desalination device. Gnd = ground.

For multi-wall anode experiments, microfabricated 100 nm-thick Pt electrodes atop a 10 nm-thick Ti adhesion layer were prepared on glass substrates as described in Chapter 5. In addition, a 10 nm-thick Ti adhesion layer and 100 nm-thick Pt layer were deposited directly on the PDMS microchannel structure by electron beam (e-beam) deposition.[182] Scotch tape (3M, St. Paul, MN) masked the PDMS regions where metal deposition was unwanted. Lift-off of excess metal was performed by removing the Scotch tape, which revealed a ~100 µm-wide anode on the side wall and ceiling of the PDMS microchannel that extended ~50 µm into and upstream of the branched microchannel. The final anode construction is

depicted in Scheme 6.2, showing an anode on the microchannel floor, side wall, and ceiling.

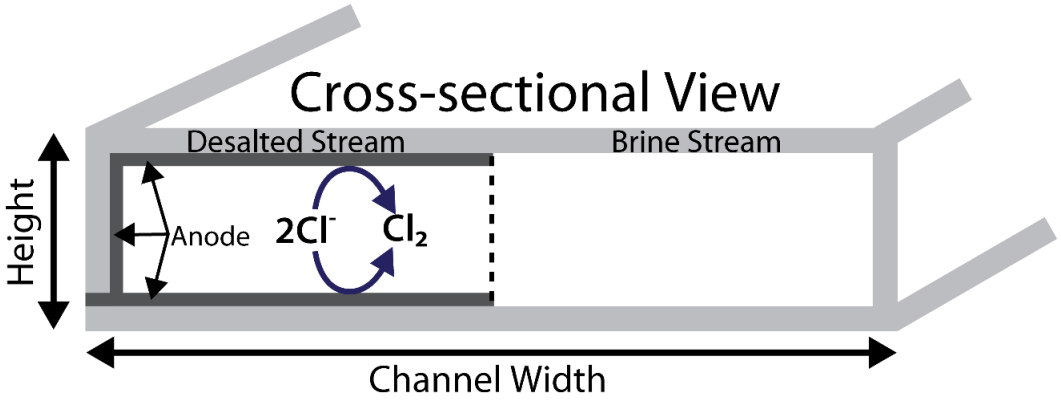

Scheme 6.2:

Schematic illustrating the multi-wall anode design. The Pt anode extends ~50 μm into the channel from the floor and ceiling. The side wall nearest to the desalted channel is also coated with Pt.

For photodesalination experiments, TiO_2 photoanodes were prepared on quartz substrates as follows by thermal oxidation of a Ti film.[183,184] Using photolithographic and e-beam deposition, a 200 nm-thick Ti electrode was prepared on quartz substrates. The Ti electrode was then thermally oxidized to TiO_2 by placing the electrode in a tube furnace heated at a rate of 30 °C/min to 450 °C for 1 hr while exposed to air, thus allowing O_2 to diffuse into the Ti lattice and forming a thin film of TiO_2 above a conductive Ti support. The devices were cooled back to room temperature at a rate

of 5 °C/min. 450 °C is between the transition temperatures of anatase and rutile TiO_2, consequently we expect to produce a polycrystalline electrode.[185] The TiO_2 photoanode was then bound to a PDMS microchannel as previously described.

Devices for C^4D measurements were prepared following a previously published procedure illustrated in Scheme 6.3.[186] First, 100 nm-thick Cr C^4D electrodes were patterned and deposited on a glass slide using photolithographic masking and e-beam deposition. The C^4D electrodes were then insulated using a 200 nm-thick layer of SiO_2 deposited on the C^4D electrodes by e-beam deposition. The SiO_2 layer serves as an insulating barrier between the AC conductivity and DC EMD circuits. A strip of polyimide tape is used to mask the SiO_2 deposition to allow electrical connection to Cr C^4D contact pads. Finally, using a mask aligner, a 100 nm-thick Pt anode on top of a 10 nm-thick Ti adhesion layer is positioned by photolithography and deposited with e-beam deposition.

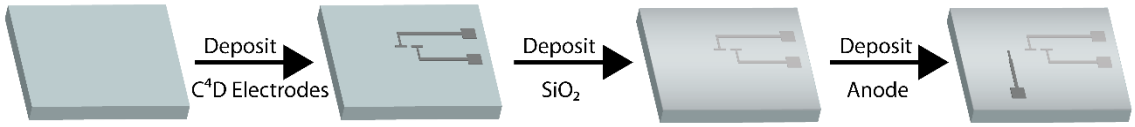

Scheme 6.3:

Schematic illustrating the three key steps to fabricating EMD devices with on-chip C^4D electrodes: deposition of C^4D electrodes, insulation by SiO_2 deposition, Pt anode deposition.

C^4D Measurements

The solution conductivity in the desalted channel (Scheme 6.1) was monitored using a contactless conductivity detector (ER225, eDAQ Inc., Denistone East, Australia) equipped with a headstage (ER125, eDAQ) compatible with microfluidic devices. Ohmic connections between the Cr C^4D contact pads and headstage were made with Au-coated pogo pins embedded in a custom acrylic device holder (Figure 6.1).

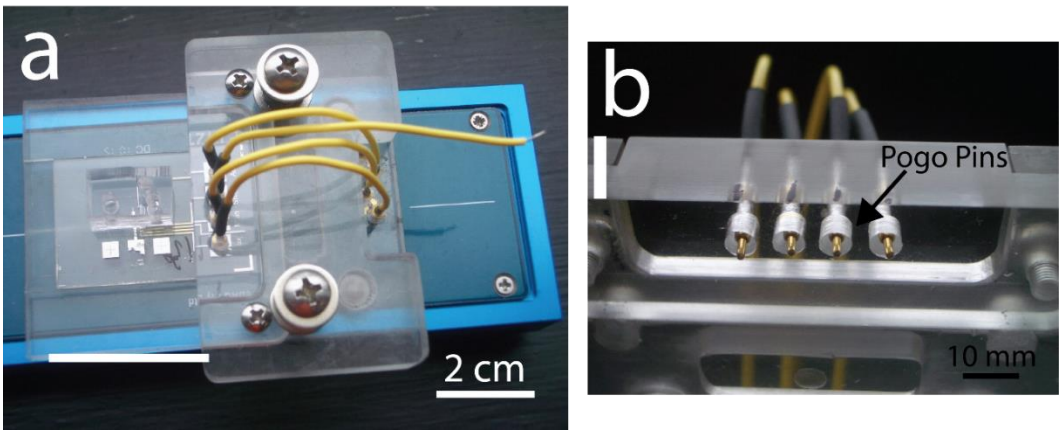

Figure 6.1:

(a) Photograph of the custom acrylic device holder containing four pogo pins for connection to the Cr C^4D contact pads and headstage. (b) Close up view of the four pogo pins embedded in the acrylic holder.

The conductivity in the desalted stream was monitored using PowerChrom (eDAQ) software coupled to the C^4D headstage and detector. Measurement of the conductivity proceeded as follows. The channel was rinsed and the flow rate set to ~100

nL/min by PDF using the solution that would initially fill the channel. With no DC bias applied, C^4D electrodes applied a sinusoidal AC waveform at 250 kHz and 2% amplitude to one of the two C^4D electrodes beneath the desalted channel. The second C^4D electrode monitored the AC signal, which is attenuated by the solution conductivity, and converted it to an output DC voltage measured at 10 Hz in a 200 mV range. Before each experiment, the PowerChrom software was used to set the initial measured signal to 0. Solutions were exchanged from reservoirs manually with a pipette. When a DC bias was applied, a battery-pack was used to apply a 1.3 V bias between the anode and cathodes located in each of the reservoirs. Devices were periodically monitored optically with a top-down microscope (AZ100, Nikon, Tokyo, Japan) fitted with a CCD camera (QuantEM: 512SC, Photometrics, Tucson, AZ).

Improving Salt Rejection with a Multi-Wall Anode

Presently, EMD has achieved a maximum separation of 25% for a 0.50 M NaCl solution. A primary reason for this low salt rejection is illustrated by the simulations in Figure 6.2. These simulations were carried out with a planar anode in 0.50 M NaCl at a PDF of 80 nL/min, analogous to the work presented in Chapters 4 and 5. Figure 6.2a is a normalized

salinity distribution at the central plane of the microchannel (z = 11 μm) showing 20% salt rejection.

The anode is responsible for driving Cl^- oxidation and generating the elevated local electric field required for separation. The purple and green arrows in Figure 6.2a correspond to the simulated electric field strengths across the microchannel width that are plotted in Figure 6.2b. The purple trace in Figure 6.2b shows the electric field strength away from the anode is low. The green trace shows the field strength is highest above the anode (0 on x-axis), but decays to 0 at the channel wall opposite the anode. This electric field profile allows salts to traverse the depletion zone and enter the desalted channel because the magnitude of the V_1 is not sufficient at all points upstream of the desalted channel for u_{ep} to counter bulk flow.

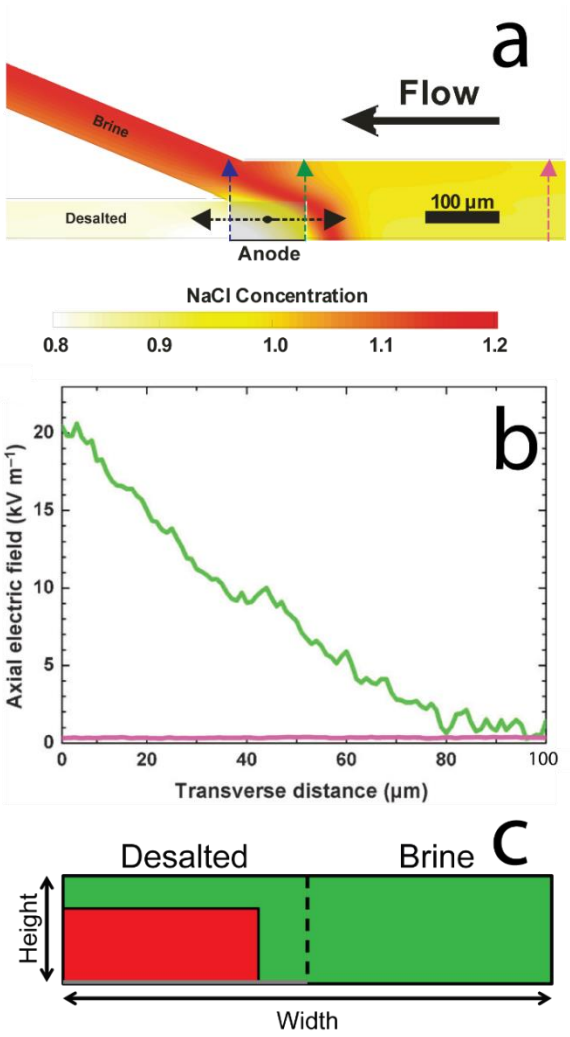

Figure 6.2:

(a) Local salinity distribution simulated for a 0.50 M NaCl solution with a total PDF rate of 80 nL/min from inlet to outlets; the current through the anode is 50 nA. (b) Simulated profiles of the axial electric field strength along the transverse direction of the separation channel (as indicated by the green and purple arrows in panel (a)). (c) A view from within the inlet toward the bifurcated channel at the location indicated by the blue arrow in (a). The green color indicates locations where the electric field strength is insufficient for separation. The red color indicates locations where the electric field strength is sufficient for separation.

For example, let's consider the separation of Na^+, the most abundant cation in seawater with the lowest μ_{ep}, meaning it requires the highest V_1 to be directed into the brine stream. With a 100 nL/min PDF, the V_1 must be ~14 kV/m. Consequently, in regions of Figure 6.2b where the bulk fluid flow is 100 nL/min, Na^+ is directed to the brine stream in regions only where the V_1 is ~14 kV/m or higher. The idea is illustrated schematically in Figure 6.2c, a cross-sectional view of the microchannel at the blue arrow in Figure 6.2a, highlighting the regions of the microchannel where the V_1 is sufficient for salt rejection. The red region denotes locations where the V_1 is sufficiently high to direct Na^+ into the brine stream. Conversely, the green region shows where the V_1 is too weak to exclude Na^+. From this simplified schematic, we can visualize that a planar anode allows salt to enter the desalted channel at transverse locations beyond ~40 μm (in this simulation, as in our experimental EMD system, the inlet channel is 100 μm wide and the two outlet channels are 50 μm wide) and also at locations near the channel ceiling (opposite the anode).

In other words, to increase the percentage of salt rejection, the channel height must be lowered or an additional anode added at the channel ceiling as shown in Scheme 6.2. Likewise, the anode must be extended further into the main channel to ensure that the V_1 is sufficiently strong

in the transverse direction to prevent leakage of salt into the desalted channel. Of course, increasing the surface area of the anode will increase faradaic current and the power consumption of the device. However, if salt rejection increases as well, the energy efficiency of EMD with a multi-wall anode may still be comparable to the theoretical energy required for the separation.

The multi-wall anode device depicted in Scheme 6.2 may increase the percentage of salt rejection because Cl^- oxidation will be driven at three walls in the microchannel. This will not only increase the size of the depletion zone, but should lead to a greater decrease in the local ionic strength relative to the bulk ionic strength, thereby increasing the magnitude of V_1. Consequently, at a given flow rate, more salt is expected to be directed into the brine channel.

To support this notion, simulations analogous to those presented earlier were performed with a multi-wall anode at the channel ceiling and floor. In this configuration, Figure 6.3a shows the simulated normalized salinity distribution at the central plane of the microchannel (z = 11 μm) in a multi-wall anode device producing 50% salt rejection, more than double that with a planar anode (Figure 6.2a). Consistent with the simulations in Figure 6.2 with the multi-wall anode extending 50 μm into the channel, salts are still able to

enter the desalted channel near the center of the microchannel (Figure 6.3b), thus providing another avenue to improve salt rejection.

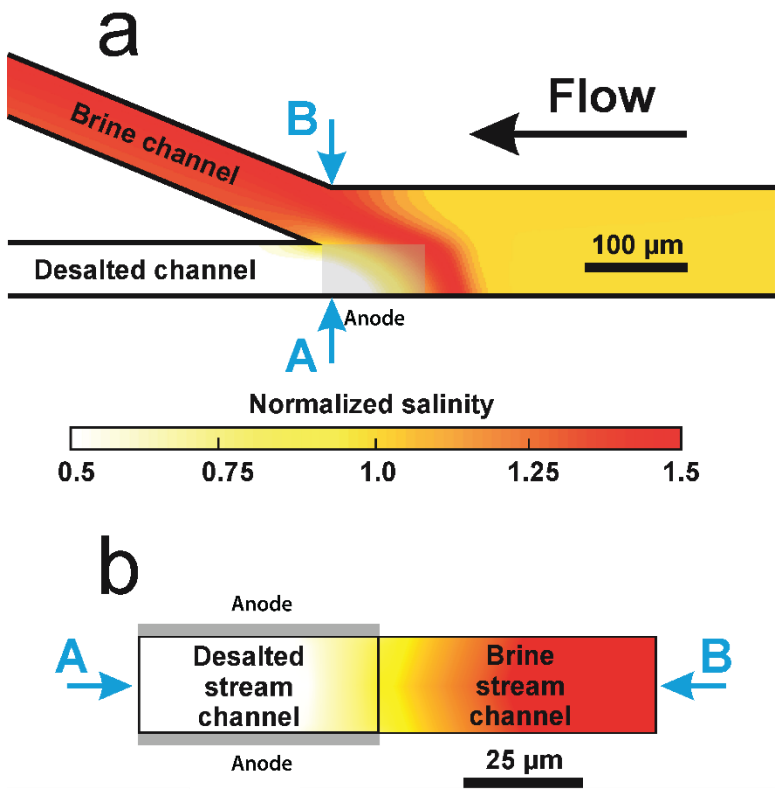

Figure 6.3:

(a) Salinity distribution simulated for a 0.50 M NaCl solution with a multi-wall anode at the microchannel floor and ceiling. The PDF rate was 80 nL/min. The current through each anode was 50 nA. (b) Cross-sectional view of the salinity distribution at the blue arrows in (a).

To demonstrate an increase in V_1 with the multi-wall anode, axial electric field measurements were performed with the multi-wall anode device described in the Experimental

Section. These experiments were carried out using a two-electrode cell configuration and the following procedure. The device was first rinsed with 0.50 M NaCl by PDF. The flow rate was then set to ~100 nL/min and a 1.3 V potential bias was applied between the multi-wall anode and electrodes in the reservoirs, while electric field data were collected for a total of ~180 s.

As shown by the red trace in Figure 6.4, the average V_1 with the multi-wall anode (2.5 mm) is ~1.75 kV/m. With reference to the horizontal axis, the inlet is centered at position 5.0 mm, the ~100 µm-wide multi-wall anode is centered at 2.5 mm, and the desalted outlet is at 0. The error bars represent the standard deviation of all the measurements made for a single ~180 s experiment. An important control experiment is shown by the black trace in Figure 6.4. Here, an experiment identical to that just described was performed with a planar anode. In this case, the V_1 above the anode is less than that measured with the multi-wall anode, demonstrating the multi-wall anode increases the V_1. Further experiments, including conductivity measurements, which we will discuss later, are required to confirm an increase in the percentage of salt rejection.

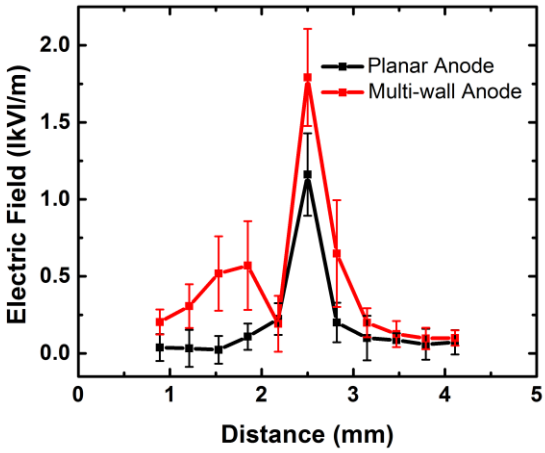

Figure 6.4:

Plots of average electric field strength vs distance across the 5.0 mm-long microchannel using a multi-wall anode (red trace) and planar anode (black trace). The experiemnts were performed in 0.50 M NaCl with a 1.3 V bias applied between the anode and the electrodes in the reservoirs. Each error bar represents the standard deviation of measurements made over a period of ~180 s. The inlet is centered at 5.0 mm, the 100 µm-wide anode is centered at 2.5 mm, and the desalted outlet is at 0. The flow rate was 100 nL/min.

Electrochemically Mediated Photodesalination

As discussed in Chapter 1, salt removal from water is inextricably linked to energy. Currently, EMD is driven by a simple power supply, which provides the energy required to oxidize Cl^- and form the ion depletion zone necessary for separation.[66] In our previous studies, only a small fraction (10^{-4}) of the total Cl^- present in a 0.50 M NaCl solution was oxidized to generate the required local electric field

gradient.[66] The EMD system currently operates on a small scale, and therefore the amount of energy required for Cl^- oxidation is small. However, at larger scales, energy efficiency is a key figure of merit. Hence, minimizing the electrical energy required for ion separations using EMD is important.

One strategy to reduce or possibly eliminate the electrical energy required for EMD is to drive the process photoelectrochemically. Here, we present preliminary experiments toward directly coupling EMD to photoelectrochemical Cl^- oxidation (Scheme 6.4). Photodriven EMD depicted in Scheme 6.4 is analogous to previously described EMD separations. However, the C or Pt anode employed in previous experiments is replaced with a TiO_2 photoanode, an *n*-type semiconductor, having a ~3.0 eV band gap,[187,188] which is sufficient to drive Cl^- oxidation (E° = 1.358 V).[189,190] Upon sufficiently energetic incident solar radiation, an electron is promoted to the conduction band of the TiO_2 photoanode to yield an electron/hole pair.[187,191] For an *n*-type semiconductor, holes move toward the electrode surface to oxidize a species in solution, while electrons carry out a corresponding reduction at a counter electrode. In the presence of NaCl, Cl^- is oxidized at the TiO_2 photoanode, while H_2O is reduced at Pt counter electrodes. Following the oxidation of Cl^-, a localized ion depletion

zone and elevated V_1 is expected to result, thus allowing ion separation by the previously described counter-flow mechanism. With this strategy, it might be possible to completely eliminate the external power supply, thereby separating ions from water using zero external electrical energy.

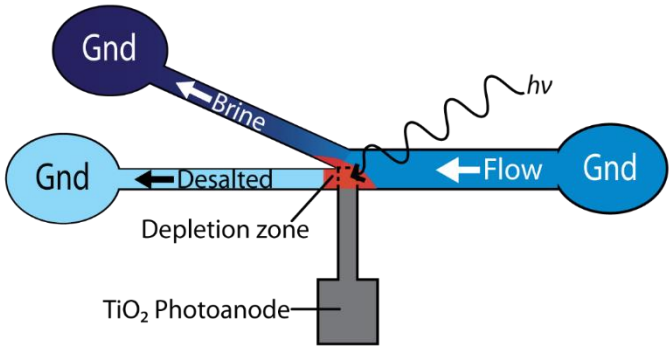

Scheme 6.4:

Schematic illustrating EMD driven photoelectrochemically.

Importantly, TiO_2 is an easily prepared and inexpensive material that exhibits excellent photostability and corrosion resistance in aqueous environments, including those containing high concentrations of Cl^-.[190,192] In fact, there are numerous reports of TiO_2 employed for photoelectrochemical applications,[188] including its use for Cl^- oxidation.[189,190] To examine photodriven EMD, we fabricated PDMS microelectrochemical devices with a thermally prepared TiO_2 photoanode as described in the Experimental Section.

To ensure our photoanodes are capable of generating photocurrents, we first measured photocurrents in a two-electrode cell configuration using a 6517 Keithley multimeter and the following procedure. Pt wires were dipped into each of the three device reservoirs to serve as counter electrodes. The device was first rinsed with 0.50 M NaCl by PDF. The flow rate was then set to ~100 nL/min. Using a Hg lamp (EFOS lite, Mississauga, Canada) equipped with a 365 nm filter, the device was exposed to three ~60s doses of radiation. The lamp was oriented ~50 mm from and roughly perpendicular to the TiO_2 photoanode. Note, there was no external bias during this experiment. Figure 6.5 shows the photocurrents collected during this experiment. The current density achieved is ~2.5 mA/cm^2, which is comparable to that measured for EMD separations with a Pt anode and power supply (~1.0 mA/cm^2).[66] Importantly, the photocurrents are stable and reproducible. At this preliminary stage, the Hg lamp intensity has not been measured and correlated to solar radiation. However, similar experiments have been carried out using artificial light with an AM 1.5 filter simulating the solar spectrum, as well as natural sunlight to demonstrate these devices can generate photocurrents in real-world conditions.

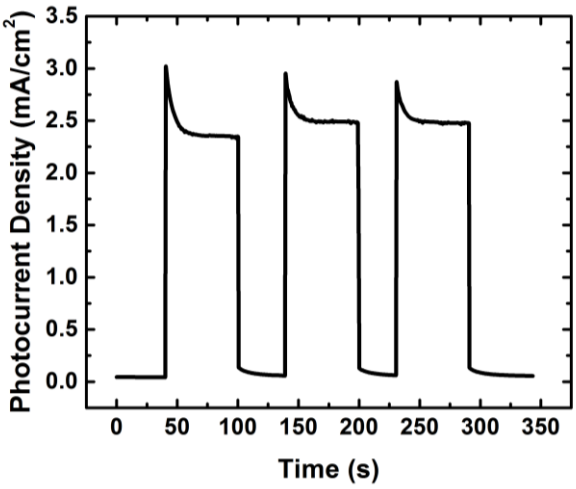

Figure 6.5:

Plot of photocurrent density vs time for a TiO_2 photoanode at open circuit and contained within a glass/PDMS EMD device exposed to 365 nm light in the presence of 0.50 M NaCl. The flow rate was 100 nL/min and the counter electrode was a Pt wire.

If the radiation intensity used to collect photocurrents in Figure 6.5 is in excess of natural solar radiation, thereby causing inflated photocurrent, higher current densities can be achieved by applying a small potential bias to the TiO_2 photoanode (Figure 6.6). In this series of experiments, photocurrents were collected in a three-electrode cell with a Pt wire counter electrode, Ag wire reference electrode, and TiO_2 photoanode in a single PDMS reservoir. The surface area of the TiO_2 was ~0.13 cm^2, as opposed to 5 x 10^{-5} cm^2 for the previous experiment in an EMD device. The reservoir was rinsed with 0.50 M NaCl. The solution was stationary during

this experiment. Photocurrent was measured with a potentiostat (CH Instruments). Chronoamperograms were collected for 300s with the potential of TiO_2 photoanode stepped to the biases (vs Ag wire) denoted in Figure 6.6. Using a Hg lamp (EXFO X-Cite 120) equipped with a UV-2E/C filter (Nikon), the device was exposed to two ~60s doses of 340 - 380 nm radiation. No photocurrent is observed with a potential bias in the absence of radiation. However, when exposed to radiation and with a small positive bias insufficient to drive Cl^- oxidation, an increase in photocurrent density is observed. While differences in experimental set-up preclude direct comparison of Figure 6.6 to results in Figure 6.5, the important point is that with a small potential bias, photocurrents can be increased.

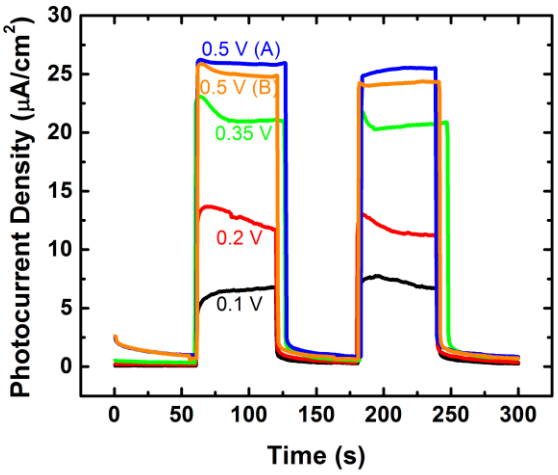

Figure 6.6:

Plot of photocurrent density vs time for a 0.13 cm^2 TiO_2 photoanode exposed to 340-380 nm light in the presence of 0.5 M NaCl. Experiments were performed in a three-electrode PDMS reservoir with a Pt counter and Ag wire reference electrode. Biases were applied for 300 s as denoted in the figure.

While Figures 6.5 and 6.6 demonstrate the TiO_2 photoanode is capable of generating photocurrent, they do not show that Cl^- oxidation is the reaction occurring. However, as discussed in Chapter 5, Cl^- oxidation results in the formation of Cl_2(aq), which subsequently undergoes hydrolysis to form HOCl, a strong oxidizing agent.[96] In fact, HOCl is capable of oxidizing the fluorescent tracer, $BODIPY^{2-}$, thus causing a decrease in fluorescence intensity.[193] For example, with no external bias and no illumination, Figure 6.7 shows the fluorescence intensity of 10.0 μM $BODIPY^{2-}$ tracer without (a) and with (b) 10.0 μM NaOCl. Figure 6.7b with NaOCl shows a

70% decrease in fluorescence intensity relative to the solution without NaOCl (a). This phenomenon is utilized to support that Cl^- oxidation is driven at the TiO_2 photoanode.

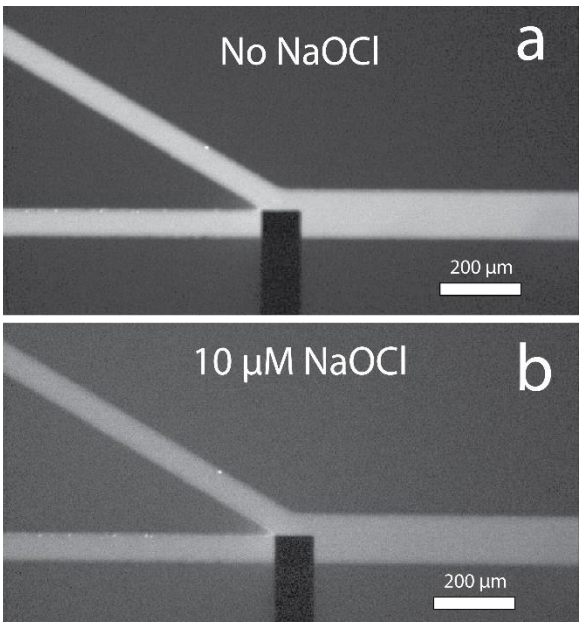

Figure 6.7:

Fluorescence micrographs of 10.0 µM $BODIPY^{2-}$ without (a) and with (b) 10.0 µM NaOCl. The microchannel is filled such that there is no flow. No illumination or bias is applied.

Figure 6.8 presents fluorescence data demonstrating Cl^- oxidation is driven at the TiO_2 photoanode. Here, the microchannel is initially filled with 0.50 M Na_2SO_4 and 10.0 µM $BODIPY^{2-}$ tracer at a 100 nL/min flow rate. Under no external bias, the device is exposed to radiation from a Hg lamp. Importantly, no significant change in fluorescence intensity

is observed. This is expected for two reasons. First, there is no ion depletion zone forming and therefore ions are not expected to separate into the brine channel. Second, water oxidation is the only reaction occurring, thus HOCL is not generated and no oxidation of $BODIPY^{2-}$ is expected.

An identical experiment was then performed, but the Na_2SO_4 solution was replaced with 0.50 M NaCl. In this case, a clear decrease in fluorescence intensity is observed due to the presence HOCL, indicating Cl^- is being oxidized. Alternatively, some of the decrease in fluorescence intensity may be due to the formation of an ion depletion zone and locally elevated electric field causing EMD. However, additional experiments are required to confirm. The important point is that only in the presence of Cl^- is the fluorescence intensity attenuated, supporting that Cl^- photooxidation is driven at the TiO_2 photoanode.

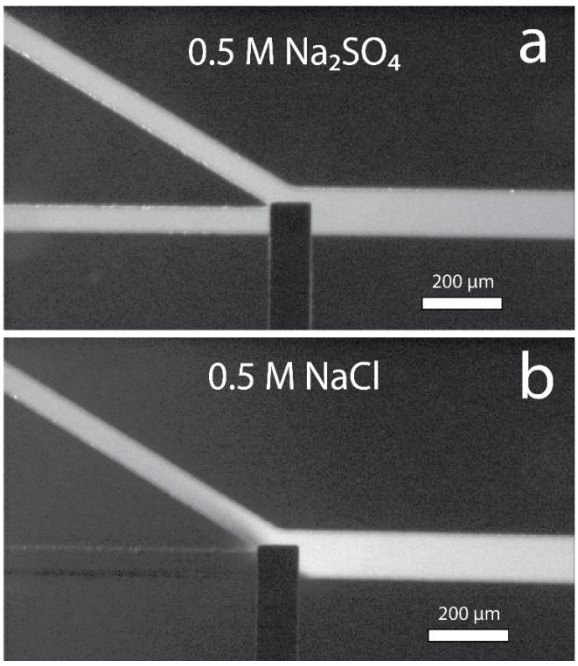

Figure 6.8:

Fluorescence micrographs of 10.0 µM $BODIPY^{2-}$ in (a) 0.50 M Na_2SO_4 and (b) 0.50 M NaCl near a TiO_2 photoanode exposed to 365 nm light with a 100 nL/min flor rate. No external bias was applied to the device.

The next step toward demonstrating photodriven EMD is to measure the axial electric field while exposing devices to incident radiation. These experiments would allow us to demonstrate the photooxidation of Cl^- is resulting in the formation of an ion depletion zone and elevated V_1. After establishing an ion depletion zone forms by Cl^- photooxidation, the final step is to quantify the amount of salt rejection using conductivity measurements. As discussed in the next section, we plan to use on-chip capacitively

coupled contactless conductivity detection (C^4D) to quantify salt rejection.

Contactless Conductivity Measurements

To analyze the performance of EMD, a suitable ion detection strategy is required. EMD studies presented earlier relied on fluorescent tracers, such as $BODIPY^{2-}$, to serve as a proxy for gauging the distribution of ions. Using fluorescence, the ion concentration is determined by correlating fluorescence intensity to a calibration curve. However, as discussed in the last section, this optical detection strategy has limitations due to fluorophores being oxidized by HOCl,[96] leading to an artificially suppressed fluorescence intensity and erroneous correlation to salt concentration. Therefore, the use of fluorescent tracers is not the optimal strategy for quantifying the extent of separations in EMD. To overcome the oxidation of organic fluorophores, we turned to metal based fluorophores such as $[Ru(bpy)_3]^{2+}$, but they too are limited in their quantitative capacity because they undergo quenching in the presence of O_2. During EMD, some amount of O_2 is generated at the anode as a product of water oxidation.

To provide a quantitative measure of ion separation, conductivity measurements are necessary. Due to the small

scale of the device, we implemented a home-built conductivity circuit described in Chapter 4.[154,156] This set-up required two microband electrodes to contact the solution. An AC signal was applied to one microband electrode, while the other electrode was held at virtual ground. The solution conductivity affects the current flow between the microband electrodes, thus altering the output signal and allowing for ion detection. Although a partial solution to our detection difficulties, several challenges remained. Most notable was the inability to fully decouple the AC conductivity circuit and the DC circuit used to drive EMD, thus frequently resulting in signal drift, bubble formation, and sometimes electrodissolution of the conductivity electrodes (Figure 6.9). Moreover, reproducibility remained a challenge with contact conductivity measurements, limiting its everyday use.

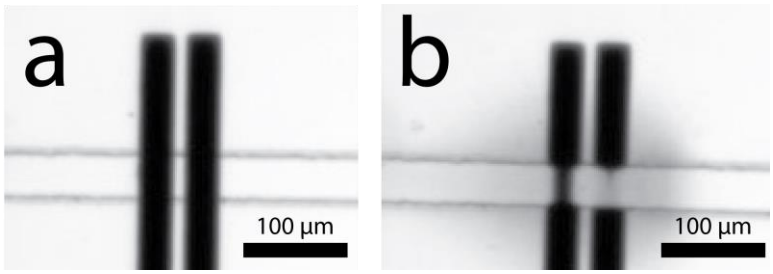

Figure 6.9:

(a) Optical micrograph of two 40.0 µm-wide pyrolyzed photoresist carbon microband electrodes used for contact conductivity measurements before (a) and after (b) an experiment showing microband dissolution.

To further develop EMD, the ability to rapidly and reliably make conductivity measurements is key. Therefore, we are working to implement capacitively coupled contactless conductivity detection (C^4D) to EMD. As illustrated in Scheme 6.5a,[194] this configuration isolates the conductivity electrodes from the solution, thereby eliminating the possibility of faradaic reactions. Moreover, because the AC conductivity electrodes are decoupled from the DC separation electrodes, little to no interference is expected between their respective circuits.

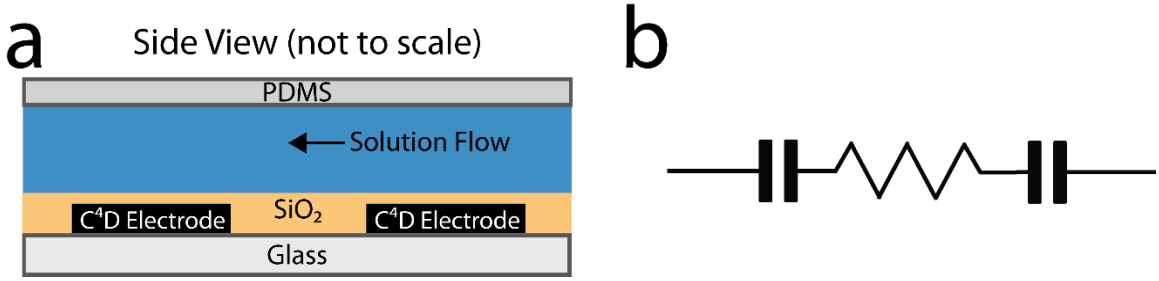

Scheme 6.5:

(a) Schematic illustrating the C^4D electrodes isolated from solution by a layer of SiO_2. (b) Simplified equivalent circuit diagram of the C^4D electrodes, SiO_2 insulating layer, and solution.

C^4D is similar to traditional conductivity measurements, but instead of applying a relatively low frequency and amplitude signal, a high frequency and amplitude signal is applied. The increased amplitude in C^4D measurements is to

mitigate signal loss form potential dropping in the insulating layer. Scheme 6.5b shows a simplified equivalent circuit diagram of the C^4D set-up where the SiO_2 layer above each electrode can be thought of as two capacitors in series with the solution resistance. Eq 6.1 describes the current expected from this circuit. However, if the signal frequency is high, eq 6.1 simplifies to eq 6.2 meaning the current flowing through the circuit is dependent on the applied AC bias (known) and the solution conductivity. Therefore, changes in current, which are converted to a DC voltage by the C^4D electronics, represent changes in solution conductivity. A signal decrease indicates a decrease in solution conductivity and conversely, a signal increase indicates an increase in solution conductivity. Importantly, absolute conductivities are not measured using this technique. Rather, conductivities are determined using a calibration curve of signal change vs conductivity.[195]

$$I = \frac{V}{\sqrt{R^2+(\frac{1}{2\pi fC})^2}} \quad (6.1)$$

$$I = \frac{V}{R} \quad (6.2)$$

C^4D measurements have been used for microdevice applications, including detection for capillary electrophoresis,[194] sensing,[196] and flow cytometry.[197] Here, we

show preliminary experiments toward implementing C^4D to quantify salt rejection in EMD. The device used for these measurements is depicted in Figure 6.10a and was prepared as described in the Experimental Section. Figures 6.10b and c show enhanced views of the measuring C^4D electrodes positioned below the desalted channel (b) and reference C^4D electrodes away from any fluidic channel (c). There are two sets of C^4D electrodes because the commercial electronics used require a differential measurement. Because the reference C^4D electrodes are away from solution, only changes in the desalted channel will result in a signal change. The microband positioned between the C^4D electrodes is used to minimize noise.

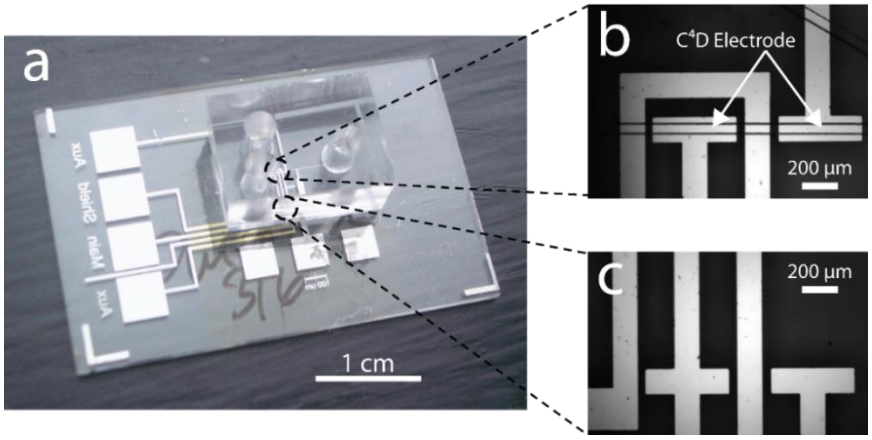

Figure 6.10:

(a) Image of the microelectrochemical device used to make C^4D measurements. (b-c) Optical micrographs of the measuring C^4D electrodes positioned below the desalted channel (b) and reference C^4D electrodes away from any fluidic channel (c). The microband between the C^4D electrodes is used to minimize noise.

To demonstrate the suitability of making C^4D measurements on-chip, Figures 6.11a and b show the raw signal (a) and calibration (b) for a proof-of-concept C^4D experiment collected in a microchannel filled with NaCl solutions of varying conductivity and without the DC circuit for EMD. The results of this and similar trials yield calibrations with R^2 = 0.98 to 0.99.

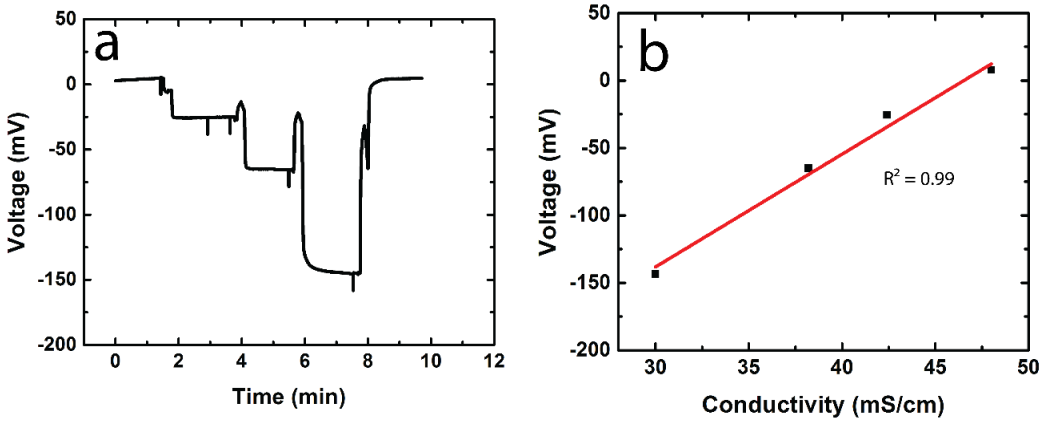

Figure 6.11:

Plot of signal voltage vs time during a 4-pt conductivity calibration using NaCl standards (a) and corresponding calibration plot (b) showing a linear response.

To demonstrate we are measuring conductivity changes and not concentration changes, a control experiment was performed with 0.36 M Na_2SO_4 and 0.50 M NaCl, both having conductivities of 48 mS/cm. The conductivity of these solutions was measured using a bench-top conductivity meter (Oakton Instruments,

Vernon Hills, IL). The device was first filled with 0.36 M Na_2SO_4 flowing through the device at ~100 nL/min by PDF. The inlet reservoir was then emptied with a pipette and filled with 0.50 M NaCl solution before again being empitied and filled with 0.36 M Na_2SO_4. Figure 6.12 demonstrates that although the concentration of the solutions is changing, the measured conductivity on-chip is constant throughout the experiment.

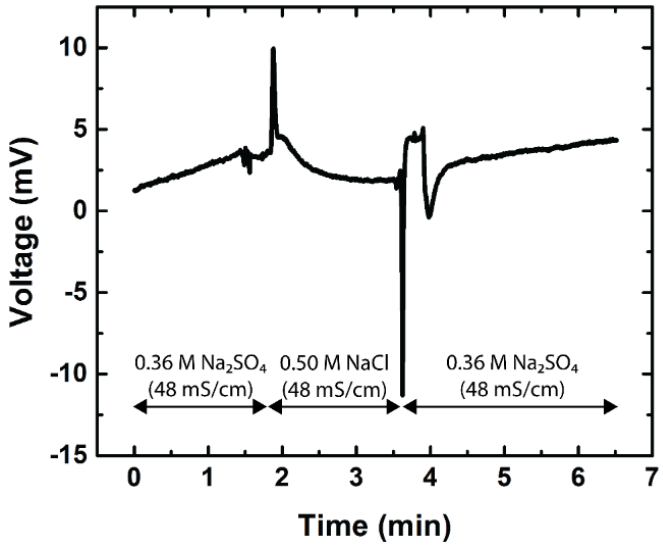

Figure 6.12:

Plot of voltage vs time for an on-chip C^4D measurement made with varying solutions as indicated in the figure. Data was collected with a ~100 nL/min PDF. The AC signal was applied at 250 kHz with a 2% amplitude.

To demonstrate on-chip C^4D measurements can be made in the presence of the DC circuit required for EMD, a control

experiment was performed in 0.50 M Na_2SO_4. With this solution, a decrease in conductivity is not expected because an ion depletion zone does not form and there is no ion separation. However, as shown in Figure 6.13, with a 1.4 V bias, a decrease in conductivity is recorded.

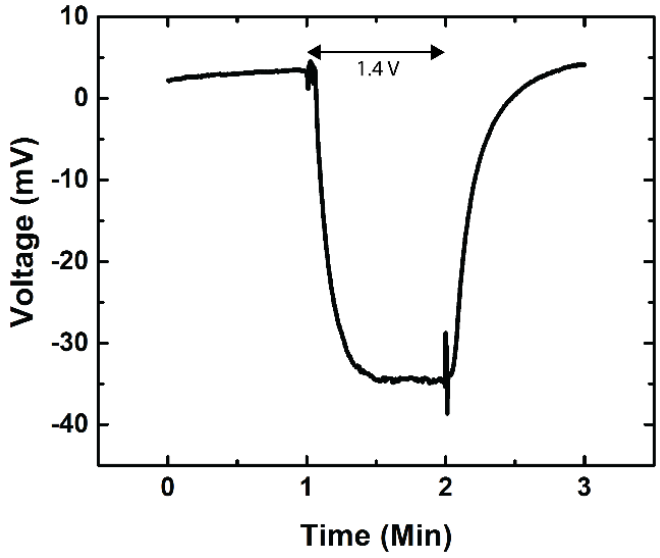

Figure 6.13:

Plot of voltage vs time for an on-chip C^4D measurement made with 0.50 M Na_2SO_4. Data was collected with a ~100 nL/min PDF. The AC signal was applied at 250 kHz with a 2% amplitude. A 1.4 V bias was applied for the times indicated in the figure.

To further investigate this result, a series of control experiments were performed. We first ensured C^4D measurements can be made in the presence of a DC bias by applying a uniform bias across the length of the channel while collecting a successful calibration. Next, because any change in

conductivity must be resulting from reactions at the anode, we performed an experiment in 0.50 M Na_2SO_4 with flow reversed, meaning flow was from the two ''outlets'' toward the ''inlet''. This ensures the solution composition above the C^4D electrodes is uniform because the reaction products generated at the anode flow away from the C^4D electrodes. From t = 1-2 min, Figure 6.14 shows there is no change in signal measured with the flow reversed. However, in the same device, with the flow moving forward and a 1.4 V bias applied (t = 4-5 min) a decrease in signal similar to that in Figure 6.13 was recorded, thus suggesting the reaction products at the anode are causing the unwanted signal change.

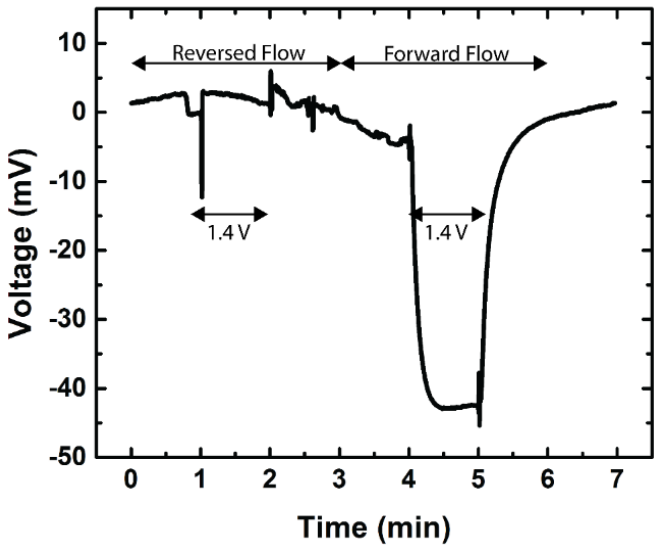

Figure 6.14:

Plot of voltage vs time for an on-chip C^4D measurement made with 0.50 M Na_2SO_4. Data was collected with a ~100 nL/min. PDF initially reversed and then forward as indicated in the figure. The AC signal was applied at 250 kHz with a 2% amplitude. A 1.4 V bias was applied for the times indicated in the figure.

In Na_2SO_4, only water oxidation is driven at the anode, which generates O_2 and H^+. The signal decrease measured in the previous experiments indicates a decrease in solution conductivity is occurring. To ensure O_2 is not causing the unexpected decrease in signal, experiments were performed while optically monitoring the device with a top-down microscope to detect bubbles. However, no bubbles were observed in these experiments, suggesting H^+ is causing the signal change. Hence, we performed control experiments where the pH in the microchannel was altered. Devices were

initially filled with 0.36 M Na_2SO_4 or 0.50 NaCl (both 48 mS/cm) while monitoring the C^4D signal. These solutions were then replaced with 0.10 M H_2SO_4 or 0.11 HCl (both 50 mS/cm), respectively. With the solution conductivity increasing, a signal increase is expected in these experiments. However, as in the previous experiments with a bias applied, Figures 6.15a and b show the signal decreases. Interestingly, when the solutions that first filled the device were placed back in the device, signal does not return to the initial baseline. While not entirely clear what is causing the unexpected signal decrease, H^+ protonating SiO^- functional groups on the surface of the SiO_2 insulating layer is a probable explanation because changes in the capacitance of the SiO_2 insulating layer will affect the C^4D response.[198,199]

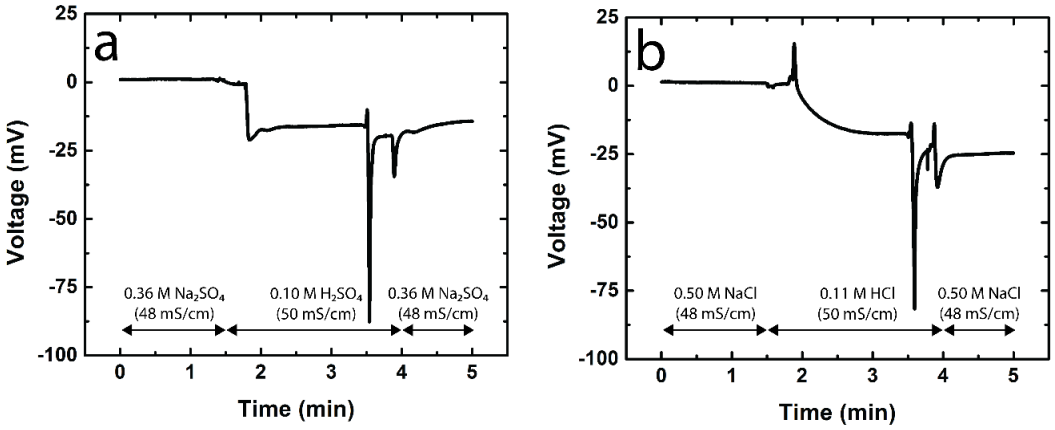

Figure 6.15:

Plot of voltage vs time for on-chip C^4D measurements made with 0.36 M Na_2SO_4 (a) or 0.50 NaCl (b) initially filling the microchannel. At t = 1.5 min, these solutions were replaced with 0.10 M H_2SO_4 (a) or 0.11 HCl (b). Data was collected with a ~100 nL/min PDF. The AC signal was applied at 250 kHz with a 2% amplitude. No bias was applied.

In summary, C^4D measurements have been successfully employed for on-chip conductivity measurements, but challenges remain when measuring with the DC circuit required for EMD. Control experiments indicate the measurement is pH sensitive. Consequently, we are unable to distinguish between salt rejection and pH changes with the current experimental set-up. Whether driving water oxidation or Cl^- oxidation, H^+ is generated downstream, meaning these challenges must be resolved to implement C^4D for quantifying salt rejection. Two possible solutions we are currently investigating: First, using buffered solutions and second, replacing the SiO_2 insulating layer with another more pH-insensitive material.

Summary and Conclusions

This chapter provides preliminary experiments for three avenues of future work to develop EMD. By implementing a multi-wall anode, experiments and simulations demonstrate an increase in V_1 which may be used to increase the percentage of salt rejection. Moreover, experiments using TiO_2 photoanodes show Cl^- oxidation can be driven photoelectrochemically, thus suggesting it may be possible to drive EMD with renewable solar radiation to reduce or eliminate the electrical energy requirements of the process. Much of the aforementioned research hinges on the ability to rapidly and reliably quantitate the percentage of salt rejection. Therefore, we have presented work toward implementing on-chip capacitively coupled contactless conductivity detection (C^4D) to quantify salt rejection.

Chapter 7: Conclusions and Outlook

This dissertation examines developments in bipolar electrochemistry for the simultaneous separation and enrichment of charged species and membraneless electrochemically mediated desalination. The basis for each of these techniques is that faradaic electrochemical reactions result in the generation of a local ion depletion zone and concomitant elevated electric field within a microchannel. With control over bulk fluid flow, charged species may be enriched and or separated at the elevated electric field. We demonstrated the principles of BPE focusing can be applied toward a two-electrode microelectrochemical cell to form an ion depletion zone by Cl^- oxidation for continuous separations by EMD.

EMD provides three important advantages compared to currently available desalination techniques: high energy efficiency, simplicity, and the absence of a physical membrane. Instead of a membrane, a small percentage of Cl^- present in solution is converted to neutral $Cl_2(aq)$, which is sufficient to generate an ion depletion zone and concomitant elevated electric field that facilitates ion separation. There is a clear need for a reliable and sustainable fresh water supply beyond those currently available. Although proper water management practices are crucial, these

solutions alone cannot meet rising demand. Because conventional water treatment costs are continually rising, while desalination costs have been steadily decreasing, desalination is becoming an increasingly viable solution for meeting global water challenges.[92] In fact, desalination is already becoming a component of many nations' water supply portfolios. Since 1960, there has been an exponential growth in desalination, which is expected to continue in the coming decades.[90,92]

It is increasingly likely that a variety of desalination technologies will be required to supplement the natural fresh water reserve. A number of novel desalination technologies are being developed to lower the overall cost of desalination by overcoming the limitations of currently available strategies. For example, RO has plateaued in terms of energy efficiency for the separation process, but reducing the intensive pre-treatment expenditures required for RO would lower the cost of desalination, thereby increasing its viability. EMD, which operates at energy efficiencies comparable to RO, but requires less pre-treatment and no membrane, could potentially achieve this goal.

Although EMD provides a number of benefits relative to existing desalination technologies, it faces several key challenges. Primary in this regard is the feasibility of scaling the technology to a commercially viable level. While

much of the work in this dissertation focuses on the underlying principles of EMD, scaling EMD to levels sufficient for real-world application should be on the forefront of future work. Scaling would not only demonstrate the viability of EMD, but also allow access to larger output of desalted water sufficient for conductivity to be measured off-channel, solving a key challenge currently limiting the development of EMD. While there are many possible approaches to generate larger output volumes, we'll briefly discuss two strategies here. The first is to increase the width of both the channel and electrode, while maintaining the existing channel height and device design. Along these lines, recent literature supports that a device with an ion depletion zone formed by ICP operated in three dimensions, rather than two like our current design, can be used to scale desalination.[114] The second approach is to operate multiple devices of the current design in parallel. The idea of simultaneously running devices is analogous to the parallel BPE focusing studies presented in Chapter 3.

The second key challenge to EMD is that higher salt rejection rates are required for producing potable water. Preliminary experiments and simulations presented in Chapter 6 suggest improvements in salt rejection are feasible, but much work is still required. While potable water is the ultimate goal, not all uses of desalinated water require the

production of potable water. For example, water used in industrial cooling towers may contain substantially higher salt concentrations than that required for drinking water.[200] EMD could also be used as a first stage for a hybrid desalination strategy incorporating RO.

Glossary

ϕ	local electric potential
ε_0	vacuum permittivity
ε_r	dielectric constant
μ_{ep}	electrophoretic mobility
ΔE	change in voltage
ΔE_{elec}	potential difference between the bipolar electrode poles
ΔP	change in pressure
η	dynamic viscosity
η_{an}	anodic overpotential
η_{cat}	cathodic overpotential
ρ	density
$BODIPY^{2-}$	anionic fluorescent tracer
BPE	bipolar electrode
C	capacitance
C^4D	capacitively coupled contactless conductivity detection
CDI	capacitive deionization
CFGF	counter-flow gradient focusing
D	diffusion coefficient
DFGF	dynamic-field gradient focusing
E°	standard reduction potential
ED	electrodialysis
EDR	electrodialysis reversal
E_{elec}	floating potential of the bipolar electrode
EF	enrichment factor
EFGF	electric field gradient focusing
EM	electromigration
EMD	electrochemically mediated desalination
EOF	electroosmotic flow
E_{tot}	applied voltage between driving electrodes
F	Faraday constant
f	frequency
FASS	field-amplified sample stacking
h	channel height
I_{BPE}	total current through the bipolar electrode
ICP	ion concentration polarization
IEF	isoelectric focusing
I_{tot}	total current

ITP	isotachophoresis
j	flux
k_B	Boltzmann constant
LBM	lattice-Boltzmann method
$l_{channel}$	microchannel length
l_{elec}	bipolar electrode length
MED	multiple-effect distillation
MSF	multi-stage flash distillation
MVC	mechanical vapor compression
n	number of electrons
N	number of moles
PDF	pressure driven flow
PDMS	poly(dimethylsiloxane)
PEM	polymeric-electrolyte-membrane
PPC	pyrolyzed photoresist carbon
Q	volumetric flow rate
q_e	elementary charge
Q_{passed}	charge passed through the bipolar electrode
$Q_{present}$	charge present in solution
R	molar gas constant
R_{ct}	charge transfer resistance
R_e	Reynolds number
R_{elec}	resistance to current by the bipolar electrode
R_f	feedback resistance
RO	reverse osmosis
R_s	solution resistance
$[Ru(bpy)_3]^{2+}$	cationic fluorescent tracer
SAM	surface assembled monolayer
S_{BPE}	bipolar electrode surface area
T	temperature
TFG	temperature gradient focusing
$TrisH^+$	protonated tris(hydroxymethyl)aminomethane buffer
u_{ep}	electrophoretic velocity
$\mathbf{v}$	local flow velocity field
V_l	local electric field strength
V_O	output voltage
w	channel width
x_0	position of zero overpotential on a bipolar electrode
Z	charge

References

1. Mavré, F.; Anand, R. K.; Laws, D. R.; Chow, K.-F.; Chang, B.-Y.; Crooks, J. A.; Crooks, R. M. Bipolar Electrodes: A Useful Tool for Concentration, Separation, and Detection of Analytes in Microelectrochemical Systems. *Anal. Chem.* **2010**, *82*, 8766-8774.
2. Fosdick, S. E.; Knust, K. N.; Scida, K.; Crooks, R. M. Bipolar Electrochemistry. *Angew. Chem., Int. Ed.* **2013**, *52*, 10438-10456.
3. Loget, G.; Zigah, D.; Bouffier, L.; Sojic, N.; Kuhn, A. Bipolar Electrochemistry: From Materials Science to Motion and Beyond. *Acc. Chem. Res.* **2013**, *46*, 2513-2523.
4. Mavré, F.; Chow, K.-F.; Sheridan, E.; Chang, B.-Y.; Crooks, J. A.; Crooks, R. M. A Theoretical and Experimental Framework for Understanding Electrogenerated Chemiluminescence (ECL) Emission at Bipolar Electrodes. *Anal. Chem.* **2009**, *81*, 6218-6225.
5. Terrill, R. H.; Balss, K. M.; Zhang, Y. M.; Bohn, P. W. Dynamic monolayer gradients: Active spatiotemporal control of alkanethiol coatings on thin gold films. *J. Am. Chem. Soc.* **2000**, *122*, 988-989.
6. Duval, J.; Kleijn, J. M.; van Leeuwen, H. P. Bipolar electrode behaviour of the aluminium surface in a lateral electric field. *J. Electroanal. Chem.* **2001**, *505*, 1-11.
7. Zhan, W.; Alvarez, J.; Crooks, R. M. Electrochemical sensing in microfluidic systems using electrogenerated chemiluminescence as a photonic reporter of redox reactions. *J. Am. Chem. Soc.* **2002**, *124*, 13265-13270.
8. Bard, A. J.; Faulkner, L. R. *Electrochemical Methods: Fundamentals and Applications*; 2nd ed. John Wiley & Sons: New York, **2001**.
9. Duval, J. F. L.; Huijs, G. K.; Threels, W. F.; Lyklema, J.; van Leeuwen, H. P. Faradaic depolarization in the electrokinetics of the metal-electrolyte solution interface. *J. Colloid Interface Sci.* **2003**, *260*, 95-106.

10. Duval, J. F. L.; Minor, M.; Cecilia, J.; van Leeuwen, H. P. Coupling of lateral electric field and transversal faradaic processes at the conductor/electrolyte solution interface. *J. Phys. Chem. B* **2003**, *107*, 4143-4155.

11. Duval, J. F. L.; van Leeuwen, H. P.; Cecilia, J.; Galceran, J. Rigorous analysis of reversible faradaic depolarization processes in the electrokinetics of the metal/electrolyte solution interface. *J. Phys. Chem. B* **2003**, *107*, 6782-6800.

12. Duval, J. F. L. Electrokinetics of the amphifunctional metal/electrolyte solution interface in the presence of a redox couple. *J. Colloid Interface Sci.* **2004**, *269*, 211-223.

13. Duval, J. F. L.; Buffle, J.; van Leeuwen, H. P. Quasi-reversible faradaic depolarization processes in the electrokinetics of the metal/solution interface. *J. Phys. Chem. B* **2006**, *110*, 6081-6094.

14. Plana, D.; Shul, G.; Stephenson, M. J.; Dryfe, R. A. W. The voltammetric response of bipolar cells: Mechanistic investigations of electroless deposition. *Electrochem. Commun.* **2009**, *11*, 61-64.

15. Ndungu, P. G. *The Use of Bipolar Electrochemistry in Nanoscience: Contact Free Methods for the Site Selective Modification of Nanostructured Carbon Materials*. **2004**, Drexel University: Philadelphia, PA.

16. Plana, D.; Jones, F. G. E.; Dryfe, R. A. W. The voltammetric response of bipolar cells: Reversible electron transfer. *J. Electroanal. Chem.* **2010**, *646*, 107-113.

17. Backhurst, J. R.; Coulson, J. M.; Goodridge, F.; Plimley, R. E.; Fleischmann, M. A Preliminary Investigation of Fluidized Bed Electrodes. *J. Electrochem. Soc.* **1969**, *116*, 1600-1607.

18. Fleischmann, M.; Oldfield, J. W. Fluidized bed electrodes. I. Polarization predicted by simplified models. *J. Electroanal. Chem. Interfacial Electrochem.* **1971**, *29*, 211-230.

19. Fleischmann, M.; Ghoroghchian, J.; Rolison, D.; Pons, S. Electrochemical behavior of dispersions of spherical ultramicroelectrodes. *J. Phys. Chem.* **1986**, *90*, 6392-6400.

20. Goodridge, F.; King, C. J. H.; Wright, A. R. The behaviour of bipolar packed-bed electrodes. *Electrochim. Acta* **1977**, *22*, 347-352.

21. Goodridge, F.; King, C. J. H.; Wright, A. R. Performance Studies on a Bipolar Fluidized-Bed Electrode. *Electrochim. Acta* **1977**, *22*, 1087-1091.

22. Plimley, R. E.; Wright, A. R. A Bipolar Mechanism for Charge-Transfer in a Fluidized-Bed Electrode. *Chem. Eng. Sci.* **1984**, *39*, 395-405.

23. Ellis, K. G.; Jansson, R. E. W. Further studies on the epoxidation of propylene in a bipolar trickle bed. *J. Appl. Electrochem.* **1981**, *11*, 531-535.

24. Manji, A.; Oloman, C. W. Electrosynthesis of propylene oxide in a bipolar trickle-bed reactor. *J. Appl. Electrochem.* **1987**, *17*, 532-544.

25. Lee, J. K.; Shemilt, L. W.; Chun, H. S. Studies of bipolarity in fluidized bed electrodes. *J. Appl. Electrochem.* **1989**, *19*, 877-881.

26. Smotkin, E.; Bard, A. J.; Campion, A.; Fox, M. A.; Mallouk, T.; Webber, S. E.; White, J. M. Bipolar titanium dioxide/platinum semiconductor photoelectrodes and multielectrode arrays for unassisted photolytic water splitting. *J. Phys. Chem.* **1986**, *90*, 4604-4607.

27. Cervera-March, S.; Smotkin, E. S.; Bard, A. J.; Campion, A.; Fox, M. A.; Mallouk, T.; Webber, S. E.; White, J. M. Modeling of Bipolar Semiconductor Photoelectrode Arrays for Electrolytic Processes. *J. Electrochem. Soc.* **1988**, *135*, 567-573.

28. Wiesener, K.; Ohms, D.; Benczúr-Ürmössy, G.; Berthold, M.; Haschka, F. High power metal hydride bipolar battery. *J. Power Sources* **1999**, *84*, 248-258.

29. Steele, B. C. H.; Heinzel, A. Materials for fuel-cell technologies. *Nature* **2001**, *414*, 345-352.

30. Hermann, A.; Chaudhuri, T.; Spagnol, P. Bipolar plates for PEM fuel cells: A review. *Int. J. Hydrogen Energy* **2005**, *30*, 1297-1302.

31. Guerrette, J. P.; Oja, S. M.; Zhang, B. Coupled Electrochemical Reactions at Bipolar Microelectrodes and Nanoelectrodes. *Anal. Chem.* **2012**, *84*, 1609-1616.

32. Cox, J. T.; Guerrette, J. P.; Zhang, B. Steady-state voltammetry of a microelectrode in a closed bipolar cell. *Anal. Chem.* **2012**, *84*, 8797-804.

33. Amatore, C.; Brown, A. R.; Thouin, L.; Warkocz, J.-S. Mimicking neuronal synaptic behavior: Processing of information with 'AND' or 'OR' Boolean logic via paired-band microelectrode assemblies. *C. R. Acad. Sci. Ser. IIC* **1998**, *1*, 509-515.

34. Paxton, W. F.; Kistler, K. C.; Olmeda, C. C.; Sen, A.; St. Angelo, S. K.; Cao, Y.; Mallouk, T. E.; Lammert, P. E.; Crespi, V. H. Catalytic Nanomotors: Autonomous Movement of Striped Nanorods. *J. Am. Chem. Soc.* **2004**, *126*, 13424-13431.

35. Kline, T. R.; Paxton, W. F.; Mallouk, T. E.; Sen, A. Catalytic nanomotors: Remote-controlled autonomous movement of striped metallic nanorods. *Angew. Chem. Int. Ed.* **2005**, *44*, 744-746.

36. Sengupta, S.; Ibele, M. E.; Sen, A. Fantastic Voyage: Designing Self-Powered Nanorobots. *Angew. Chem. Int. Ed.* **2012**, *51*, 8434-8445.

37. Wang, J.; Manesh, K. M. Motion Control at the Nanoscale. *Small* **2010**, *6*, 338-345.

38. Inagi, S.; Ishiguro, Y.; Atobe, M.; Fuchigami, T. Bipolar Patterning of Conducting Polymers by Electrochemical Doping and Reaction. *Angew. Chem. Int. Ed.* **2010**, *49*, 10136-10139.

39. Ishiguro, Y.; Inagi, S.; Fuchigami, T. Gradient Doping of Conducting Polymer Films by Means of Bipolar Electrochemistry. *Langmuir* **2011**, *27*, 7158-7162.

40. Ulrich, C.; Andersson, O.; Nyholm, L.; Bjorefors, F. Formation of molecular gradients on bipolar electrodes. *Angew. Chem., Int. Ed.* **2008**, *47*, 3034-3036.

41. Ramakrishnan, S.; Shannon, C. Display of Solid-State Materials Using Bipolar Electrochemistry. *Langmuir* **2010**, *26*, 4602-4606.

42. Ramaswamy, R.; Shannon, C. Screening the optical properties of Ag-Au alloy gradients formed by bipolar electrodeposition using surface enhanced Raman spectroscopy. *Langmuir* **2011**, *27*, 878-881.

43. Fosdick, S. E.; Crooks, R. M. Bipolar Electrodes for Rapid Screening of Electrocatalysts. *J. Am. Chem. Soc.* **2012**, *134*, 863-866.

44. Fosdick, S. E.; Berglund, S. P.; Mullins, C. B.; Crooks, R. M. Parallel Screening of Electrocatalyst Candidates Using Bipolar Electrochemistry. *Anal. Chem.* **2013**, *85*, 2493-2499.

45. Fosdick, S. E.; Berglund, S. P.; Mullins, C. B.; Crooks, R. M. Evaluating Electrocatalysts for the Hydrogen Evolution Reaction Using Bipolar Electrode Arrays: Bi- and Trimetallic Combinations of Co, Fe, Ni, Mo, and W. *ACS Catal.* **2014**, *4*, 1332-1339.

46. Klett, O.; Nyholm, L. Separation High Voltage Field Driven On-Chip Amperometric Detection in Capillary Electrophoresis. *Anal. Chem.* **2003**, *75*, 1245-1250.

47. Ordeig, O.; Godino, N.; del Campo, J.; Munoz, F. X.; Nikolajeff, F.; Nyholm, L. On-Chip Electric Field Driven Electrochemical Detection Using a Poly(dimethylsiloxane) Microchannel with Gold Microband Electrodes. *Anal. Chem.* **2008**, *80*, 3622-3632.

48. Chang, B.-Y.; Chow, K.-F.; Crooks, J. A.; Mavre, F.; Crooks, R. M. Two-channel microelectrochemical bipolar electrode sensor array. *Analyst* **2012**, *137*, 2827-2833.

49. Chow, K.-F.; Mavre, F.; Crooks, R. M. Wireless Electrochemical DNA Microarray Sensor. *J. Am. Chem. Soc.* **2008**, *130*, 7544-7545.

50. Chow, K.-F.; Mavre, F.; Crooks, J. A.; Chang, B.-Y.; Crooks, R. M. A Large-Scale, Wireless Electrochemical Bipolar Electrode Microarray. *J. Am. Chem. Soc.* **2009**, *131*, 8364-8365.

51. Chow, K.-F.; Chang, B.-Y.; Zaccheo, B. A.; Mavre, F.; Crooks, R. M. A Sensing Platform Based on Electrodissolution of a Ag Bipolar Electrode. *J. Am. Chem. Soc.* **2010**, *132*, 9228-9229.

52. Dhopeshwarkar, R.; Hlushkou, D.; Nguyen, M.; Tallarek, U.; Crooks, R. M. Electrokinetics in Microfluidic Channels Containing a Floating Electrode. *J. Am. Chem. Soc.* **2008**, *130*, 10480-10481.

53. Shackman, J. G.; Ross, D. Counter-flow gradient electrofocusing. *Electrophoresis* **2007**, *28*, 556-571.

54. Yalcin, S. E.; Sharma, A.; Qian, S.; Joo, S. W.; Baysal, O. Manipulating particles in microfluidics by floating electrodes. *Electrophoresis* **2010**, *31*, 3711-3718.

55. Yalcin, S. E.; Sharma, A.; Qian, S.; Joo, S. W.; Baysal, O. On-demand particle enrichment in a microfluidic channel by a locally controlled floating electrode. *Sens. Actuators, B* **2011**, *153*, 277-283.

56. Perdue, R. K.; Laws, D. R.; Hlushkou, D.; Tallarek, U.; Crooks, R. M. Bipolar Electrode Focusing: The Effect of Current and Electric Field on Concentration Enrichment. *Anal. Chem.* **2009**, *81*, 10149-10155.

57. Anand, R. K.; Sheridan, E.; Hlushkou, D.; Tallarek, U.; Crooks, R. M. Bipolar electrode focusing: tuning the electric field gradient. *Lab Chip* **2011**, *11*, 518-527.

58. Anand, R. K.; Sheridan, E.; Knust, K. N.; Crooks, R. M. Bipolar Electrode Focusing: Faradaic Ion Concentration Polarization. *Anal. Chem.* **2011**, *83*, 2351-2358.

59. Hlushkou, D.; Perdue, R. K.; Dhopeshwarkar, R.; Crooks, R. M.; Tallarek, U. Electric field gradient focusing in microchannels with embedded bipolar electrode. *Lab Chip* **2009**, *9*, 1903-1913.

60. Laws, D. R.; Hlushkou, D.; Perdue, R. K.; Tallarek, U.; Crooks, R. M. Bipolar Electrode Focusing: Simultaneous

Concentration Enrichment and Separation in a Microfluidic Channel Containing a Bipolar Electrode. *Anal. Chem.* **2009**, *81*, 8923-8929.

61. Sheridan, E.; Hlushkou, D.; Anand, R. K.; Laws, D. R.; Tallarek, U.; Crooks, R. M. Label-Free Electrochemical Monitoring of Concentration Enrichment during Bipolar Electrode Focusing. *Anal. Chem.* **2011**, *83*, 6746-6753.

62. Sheridan, E.; Hlushkou, D.; Knust, K. N.; Tallarek, U.; Crooks, R. M. Enrichment of Cations via Bipolar Electrode Focusing. *Anal. Chem.* **2012**, *84*, 7393-7399.

63. Knust, K. N.; Sheridan, E.; Anand, R. K.; Crooks, R. M. Dual-channel bipolar electrode focusing: simultaneous separation and enrichment of both anions and cations. *Lab Chip* **2012**, *12*, 4107-4114.

64. Sheridan, E.; Knust, K. N.; Crooks, R. M. Bipolar electrode depletion: membraneless filtration of charged species using an electrogenerated electric field gradient. *Analyst* **2011**, *136*, 4134-4137.

65. Scida, K.; Sheridan, E.; Crooks, R. M. Electrochemically-gated delivery using bipolar electrodes: control over enriched band location and transport. *Lab Chip* **2013**, *13*, 2292-2299.

66. Knust, K. N.; Hlushkou, D.; Anand, R. K.; Tallarek, U.; Crooks, R. M. Electrochemically mediated seawater desalination. *Angew. Chem., Int. Ed.* **2013**, *52*, 8107-8110.

67. Vörösmarty, C. J.; Green, P.; Salisbury, J.; Lammers, R. B. Global water resources: vulnerability from climate change and population growth. *Science* **2000**, *289*, 284-288.

68. Ramanathan, V.; Crutzen, P. J.; Kiehl, J. T.; Rosenfeld, D. Aerosols, climate, and the hydrological cycle. *Science* **2001**, *294*, 2119-2124.

69. Schwarzenbach, R. P.; Escher, B. I.; Fenner, K.; Hofstetter, T. B.; Johnson, C. A.; von Gunten, U.; Wehrli, B. The Challenge of Micropollutants in Aquatic Systems. *Science* **2006**, *313*, 1072-1077.

70. Postel, S. L.; Daily, G. C.; Ehrlich, P. R. Human appropriation of renewable fresh water. *Science* **1996**, *271*, 785-788.

71. *The World's Water: The Biennial Report on Freshwater Resources*, ed. P.H. Gleick. Vol. 7. Island Press, **2012**.

72. *World Water Development Report 2*. United Nations, **2006**.

73. Falkenmark, M.; Lundqvist, J.; Widstrand, C. Macro-scale water scarcity requires micro-scale approaches. Aspects of vulnerability in semi-arid development. *Nat. Resour. Forum* **1989**, *13*, 258-267.

74. Kenny, J. F.; Barber, N. L.; Hutson, S. S.; Linsey, K. S.; Lovelace, J. K.; Maupin, M. A., *Estimated Use of Water in the United States in 2005*, U.S.G. Survey, Editor. **2005**.

75. *World Energy Outlook*. International Energy Agency, **2013**.

76. Oki, T.; Kanae, S. Global Hydrological Cycles and World Water Resources. *Science* **2006**, *313*, 1068-1072.

77. *Water in Crisis: A Guide to the World's Fresh Water Resources*, ed. P.H. Gleick. Oxford University Press, **1993**.

78. Nriagu, J. O.; Pacyna, J. M. Quantitative assessment of worldwide contamination of air, water and soils by trace metals. *Nature* **1988**, *333*, 134-139.

79. Fick, J.; Söderström, H.; Lindberg, R. H.; Phan, C.; Tysklind, M.; Larsson, D. G. J. Contamination of surface, ground, and drinking water from pharmaceutical production. *Environ. Toxicol. Chem.* **2009**, *28*, 2522-2527.

80. King, C. W.; Holman, A. S.; Webber, M. E. Thirst for energy. *Nat. Geosci.* **2008**, *1*, 283-286.

81. Hightower, M.; Pierce, S. A. The energy challenge. *Nature* **2008**, *452*, 285-286.

82. Semiat, R. Energy Issues in Desalination Processes. *Environ. Sci. Technol.* **2008**, *42*, 8193-8201.

83. Montgomery, C. T.; Smith, M. B. Hydraulic Fracturing: History of an Enduring Technology. *J. Pet. Technol.* **2010**, *62*, 26-32.

84. Miller, D. J.; Huang, X.; Li, H.; Kasemset, S.; Lee, A.; Agnihotri, D.; Hayes, T.; Paul, D. R.; Freeman, B. D. Fouling-resistant membranes for the treatment of flowback water from hydraulic shale fracturing: A pilot study. *J. Membr. Sci.* **2013**, *437*, 265-275.

85. Osborn, S. G.; Vengosh, A.; Warner, N. R.; Jackson, R. B. Methane contamination of drinking water accompanying gas-well drilling and hydraulic fracturing. *Proc. Natl. Acad. Sci. U. S. A.* **2011**, *108*, 8172-8176.

86. Spiegler, K. S.; El-Sayed, Y. M. The energetics of desalination processes. *Desalination* **2001**, *134*, 109-128.

87. Elimelech, M.; Phillip, W. A. The Future of Seawater Desalination: Energy, Technology, and the Environment. *Science* **2011**, *333*, 712-717.

88. *Properties of Seawater*, 93rd ed.; CRC Handbook of Chemistry and Physics, ed. W.M. Haynes. CRC Press: USA, **2012**.

89. Al-Sahali, M.; Ettouney, H. Developments in thermal desalination processes: Design, energy, and costing aspects. *Desalination* **2007**, *214*, 227-240.

90. *Desalination: A National Perspective*. National Academy of Sciences: Washington, D.C., **2008**.

91. *Seawater Desalination: Conventional and Renewable Energy Processes*, ed. A. Cipollina, G. Micale, and L. Rizzuti. Springer, **2009**.

92. *Sustainable Water for the Future: Water Recycling versus Desalination*, Sustainability Science and Engineering, ed. I.C. Escobar and A.I. Schäfer. Vol. 2. Elsevier, **2010**.

93. Karagiannis, I. C.; Soldatos, P. G. Water desalination cost literature: review and assessment. *Desalination* **2008**, *223*, 448-456.

94. Koschikowski, J.; Wieghaus, M.; Rommel, M. Solar thermal-driven desalination plants based on membrane distillation. *Desalination* **2003**, *156*, 295-304.

95. Schwantes, R.; Cipollina, A.; Gross, F.; Koschikowski, J.; Pfeifle, D.; Rolletschek, M.; Subiela, V. Membrane distillation: Solar and waste heat driven demonstration plants for desalination. *Desalination* **2013**, *323*, 93-106.

96. Geise, G. M.; Lee, H.-S.; Miller, D. J.; Freeman, B. D.; McGrath, J. E.; Paul, D. R. Water purification by membranes: the role of polymer science. *J. Polym. Sci., Part B: Polym. Phys.* **2010**, *48*, 1685-1718.

97. Fritzmann, C.; Löwenberg, J.; Wintgens, T.; Melin, T. State-of-the-art of reverse osmosis desalination. *Desalination* **2007**, *216*, 1-76.

98. Lonsdale, H. K.; Merten, U.; Riley, R. L. Transport properties of cellulose acetate osmotic membranes. *J. Appl. Polym. Sci.* **1965**, *9*, 1341-1362.

99. Paul, D. R. Reformulation of the solution-diffusion theory of reverse osmosis. *J. Membr. Sci.* **2004**, *241*, 371-386.

100. Lee, K. P.; Arnot, T. C.; Mattia, D. A review of reverse osmosis membrane materials for desalination. Development to date and future potential. *J. Membr. Sci.* **2011**, *370*, 1-22.

101. Shannon, M. A.; Bohn, P. W.; Elimelech, M.; Georgiadis, J. G.; Mariñas, B. J.; Mayes, A. M. Science and technology for water purification in the coming decades. *Nature* **2008**, *452*, 301-310.

102. Geise, G. M.; Park, H. B.; Sagle, A. C.; Freeman, B. D.; McGrath, J. E. Water permeability and water/salt selectivity tradeoff in polymers for desalination. *J. Membr. Sci.* **2011**, *369*, 130-138.

103. Yang, H. Y.; Han, Z. J.; Yu, S. F.; Pey, K. L.; Ostrikov, K.; Karnik, R. Carbon nanotube membranes with ultrahigh specific adsorption capacity for water desalination and purification. *Nat. Commun.* **2013**, *4*, 2220.

104. Tang, C. Y.; Zhao, Y.; Wang, R.; Hélix-Nielsen, C.; Fane, A. G. Desalination by biomimetic aquaporin membranes: Review of status and prospects. *Desalination* **2013**, *308*, 34-40.

105. Glater, J.; Hong, S.-k.; Elimelech, M. The search for a chlorine-resistant reverse osmosis membrane. *Desalination* **1994**, *95*, 325-45.

106. Park, H. B.; Freeman, B. D.; Zhang, Z.-B.; Sankir, M.; McGrath, J. E. Highly chlorine-tolerant polymers for desalination. *Angew. Chem., Int. Ed.* **2008**, *47*, 6019-6024.

107. Strathmann, H. Electrodialysis, a mature technology with a multitude of new applications. *Desalination* **2010**, *264*, 268-288.

108. Oren, Y. Capacitive deionization (CDI) for desalination and water treatment - past, present and future (a review). *Desalination* **2008**, *228*, 10-29.

109. Porada, S.; Zhao, R.; van der Wal, A.; Presser, V.; Biesheuvel, P. M. Review on the science and technology of water desalination by capacitive deionization. *Prog. Mater. Sci.* **2013**, *58*, 1388-1442.

110. Anderson, M. A.; Cudero, A. L.; Palma, J. Capacitive deionization as an electrochemical means of saving energy and delivering clean water. Comparison to present desalination practices: Will it compete? *Electrochim. Acta* **2010**, *55*, 3845-3856.

111. Zangle, T. A.; Mani, A.; Santiago, J. G. Theory and experiments of concentration polarization and ion focusing at microchannel and nanochannel interfaces. *Chem. Soc. Rev.* **2010**, *39*, 1014-1035.

112. Kim, S. J.; Ko, S. H.; Kang, K. H.; Han, J. Direct seawater desalination by ion concentration polarization. *Nat. Nanotechnol.* **2010**, *5*, 297-301.

113. Kim, S. J.; Ko, S. H.; Kang, K. H.; Han, J. Direct seawater desalination by ion concentration polarization. *Nat. Nanotechnol.* **2013**, *8*, 609.

114. Macdonald, B. D.; Gong, M. M.; Zhang, P.; Sinton, D. Out-of-plane ion concentration polarization for scalable water desalination. *Lab Chip* **2014**, *14*, 681-685.

115. Tran, N. T.; Ayed, I.; Pallandre, A.; Taverna, M. Recent innovations in protein separation on microchips by

electrophoretic methods: An update. *Electrophoresis* **2010**, *31*, 147-173.

116. Cui, H.; Horiuchi, K.; Dutta, P.; Ivory, C. F. Isoelectric Focusing in a Poly(dimethylsiloxane) Microfluidic Chip. *Anal. Chem.* **2005**, *77*, 1303-1309.

117. Kohlheyer, D.; Eijkel, J. C. T.; Schlautmann, S.; van den Berg, A.; Schasfoort, R. B. M. Microfluidic high-resolution free-flow isoelectric focusing. *Anal. Chem.* **2007**, *79*, 8190-8198.

118. Yang, H.; Chien, R. L. Sample stacking in laboratory-on-a-chip devices. *J. Chromatogr. A* **2001**, *924*, 155-163.

119. Jung, B.; Bharadwaj, R.; Santiago, J. G. Thousandfold signal increase using field-amplified sample stacking for on-chip electrophoresis. *Electrophoresis* **2003**, *24*, 3476-3483.

120. Jung, B.; Zhu, Y.; Santiago, J. G. Detection of 100 aM fluorophores using a high-sensitivity on-chip CE system and transient isotachophoresis. *Anal. Chem.* **2007**, *79*, 345-349.

121. Khurana, T. K.; Santiago, J. G. Preconcentration, separation, and indirect detection of nonfluorescent analytes using fluorescent mobility markers. *Anal. Chem.* **2008**, *80*, 279-286.

122. Huang, Z.; Ivory, C. F. Digitally Controlled Electrophoretic Focusing. *Anal. Chem.* **1999**, *71*, 1628-1632.

123. Burke, J. M.; Smith, C. D.; Ivory, C. F. Development of a membrane-less dynamic field gradient focusing device for the separation of low-molecular-weight molecules. *Electrophoresis* **2010**, *31*, 902-909.

124. Humble, P. H.; Kelly, R. T.; Woolley, A. T.; Tolley, H. D.; Lee, M. L. Electric field gradient focusing of proteins based on shaped ionically conductive acrylic polymer. *Anal. Chem.* **2004**, *76*, 5641-5648.

125. Kelly, R. T.; Woolley, A. T. Electric field gradient focusing. *J. Sep. Sci.* **2005**, *28*, 1985-1993.

126. Ross, D.; Locascio, L. E. Microfluidic temperature gradient focusing. *Anal. Chem.* **2002**, *74*, 2556-2564.

127. Balss, K. M.; Vreeland, W. N.; Phinney, K. W.; Ross, D. Simultaneous concentration and separation of enantiomers with chiral temperature gradient focusing. *Anal. Chem.* **2004**, *76*, 7243-7249.

128. Kamande, M. W.; Ross, D.; Locascio, L. E.; Lowry, M.; Warner, I. M. Simultaneous concentration and separation of coumarins using a molecular micelle in micellar affinity gradient focusing. *Anal. Chem.* **2007**, *79*, 1791-1796.

129. Khurana, T. K.; Santiago, J. G. Effects of carbon dioxide on peak mode isotachophoresis: Simultaneous preconcentration and separation. *Lab Chip* **2009**, *9*, 1377-1384.

130. Inglis, D. W.; Goldys, E. M.; Calander, N. P. Simultaneous Concentration and Separation of Proteins in a Nanochannel. *Angew. Chem., Int. Ed.* **2011**, *50*, 7546-7550.

131. Burke, J. M.; Huang, Z.; Ivory, C. F. Simultaneous Separation of Negatively and Positively Charged Species in Dynamic Field Gradient Focusing Using a Dual Polarity Electric Field. *Anal. Chem.* **2009**, *81*, 8236-8243.

132. Wang, Y.-C.; Stevens, A. L.; Han, J. Million-fold Preconcentration of Proteins and Peptides by Nanofluidic Filter. *Anal. Chem.* **2005**, 77, 4293-4299.

133. Kim, S. J.; Song, Y.-A.; Han, J. Nanofluidic concentration devices for biomolecules utilizing ion concentration polarization: theory, fabrication, and applications. *Chem. Soc. Rev.* **2010**, *39*, 912-922.

134. McDonald, J. C.; Duffy, D. C.; Anderson, J. R.; Chiu, D. T.; Wu, H.; Schueller, O. J. A.; Whitesides, G. M. Fabrication of microfluidic systems in poly(dimethylsiloxane). *Electrophoresis* **2000**, *21*, 27-40.

135. Ocvirk, G.; Munroe, M.; Tang, T.; Oleschuk, R.; Westra, K.; Harrison, D. J. Electrokinetic control of fluid flow in native poly(dimethylsiloxane) capillary

electrophoresis devices. *Electrophoresis* **2000**, *21*, 107-115.

136. Burke, J. M.; Ivory, C. F. Characterization of voltage degradation in dynamic field gradient focusing. *Electrophoresis* **2008**, *29*, 1013-1025.

137. Persat, A.; Santiago, J. G. MicroRNA Profiling by Simultaneous Selective Isotachophoresis and Hybridization with Molecular Beacons. *Anal. Chem.* **2011**, *83*, 2310-2316.

138. Cheow, L. F.; Sarkar, A.; Kolitz, S.; Lauffenburger, D.; Han, J. Detecting Kinase Activities from Single Cell Lysate Using Concentration-Enhanced Mobility Shift Assay. *Anal. Chem.* **2014**, *86*, 7455-7462.

139. Ray, A.; Norden, B. Peptide nucleic acid (PNA): its medical and biotechnical applications and promise for the future. *Faseb J.* **2000**, *14*, 1041-1060.

140. Ko, S. H.; Kim, S. J.; Cheow, L. F.; Li, L. D.; Kang, K. H.; Han, J. Massively parallel concentration device for multiplexed immunoassays. *Lab Chip* **2011**, *11*, 1351-1358.

141. Bradley, J.-C.; Chen, H.-M.; Crawford, J.; Eckert, J.; Ernazarova, K.; Kurzeja, T.; Lin, M.; McGee, M.; Nadler, W.; Stephens, S. G. Creating electrical contacts between metal particles using directed electrochemical growth. *Nature* **1997**, *389*, 268-271.

142. Bradley, J. C.; Crawford, J.; Ernazarova, K.; McGee, M.; Stephens, S. G. Wire formation on circuit boards using spatially coupled bipolar electrochemistry. *Adv. Mater.* **1997**, *9*, 1168-1171.

143. Service, R. F. Desalination Freshens Up. *Science* **2006**, *313*, 1088-1090.

144. Çengel, Y. A.; Çerçi, Y.; Wood, B., *Second law analysis of separation processes of mixtures*, in *Proceedings of the ASME Advanced Energy Systems Division*. **1999**. 537-543.

145. Çerçi, Y.; Çengel, Y. A.; Wood, B., *The minimum separation work for desalination processes*, in

Proceedings of the ASME Advanced Energy Systems Division. **1999**. 545-552.

146. Penate, B.; Garcia-Rodriguez, L. Current trends and future prospects in the design of seawater reverse osmosis desalination technology. *Desalination* **2012**, *284*, 1-8.

147. Bard, A. J. *Integrated chemical systems: a chemical approach to nanotechnology*. John Wiley & Sons, Inc.: New York, NY, **1994**.

148. Suss, M. E.; Baumann, T. F.; Bourcier, W. L.; Spadaccini, C. M.; Rose, K. A.; Santiago, J. G.; Stadermann, M. Capacitive desalination with flow-through electrodes. *Energy Environ. Sci.* **2012**, *5*, 9511-9519.

149. Pasta, M.; Wessells, C. D.; Cui, Y.; La Mantia, F. A Desalination Battery. *Nano Lett.* **2012**, *12*, 839-843.

150. Sadrzadeh, M.; Mohammadi, T. Sea water desalination using electrodialysis. *Desalination* **2008**, *221*, 440-447.

151. Ranganathan, S.; McCreery, R.; Majji, S. M.; Madou, M. Photoresist-derived carbon for microelectromechanical systems and electrochemical applications. *J. Electrochem. Soc.* **2000**, *147*, 277-282.

152. Dumitrescu, I.; Yancey, D. F.; Crooks, R. M. Dual-electrode microfluidic cell for characterizing electrocatalysts. *Lab Chip* **2012**, *12*, 986-993.

153. Takmakov, P.; Zachek, M. K.; Keithley, R. B.; Walsh, P. L.; Donley, C.; McCarty, G. S.; Wightman, R. M. Carbon Microelectrodes with a Renewable Surface. *Anal. Chem.* **2010**, *82*, 2020-2028.

154. Johnson, D. E.; Enke, C. G. Bipolar pulse technique for fast conductance measurements. *Anal. Chem.* **1970**, *42*, 329-35.

155. Galloway, M.; Stryjewski, W.; Henry, A.; Ford, S. M.; Llopis, S.; McCarley, R. L.; Soper, S. A. Contact Conductivity Detection in Poly(methyl methacrylate)-Based Microfluidic Devices for Analysis of Mono- and Polyanionic Molecules. *Anal. Chem.* **2002**, *74*, 2407-2415.

156. Shadpour, H.; Hupert, M. L.; Patterson, D.; Liu, C.; Galloway, M.; Stryjewski, W.; Goettert, J.; Soper, S. A. Multichannel Microchip Electrophoresis Device Fabricated in Polycarbonate with an Integrated Contact Conductivity Sensor Array. *Anal. Chem.* **2007**, *79*, 870-878.

157. Benzi, R.; Succi, S.; Vergassola, M. The lattice Boltzmann equation: theory and applications. *Phys. Rep.* **1992**, *222*, 145-197.

158. Chen, S.; Doolen, G. D. Lattice Boltzmann method for fluid flows. *Annu. Rev. Fluid Mech.* **1998**, *30*, 329-364.

159. Succi, S. *The Lattice Boltzmann Equation for Fluid Dynamics and Beyond*. Oxford University Press: New York, NY, **2001**.

160. *Lectures on Lattice Boltzmann Methods*, ed. S. Ubertini, et al. Consorzio S.C.I.R.E.: Science4 Press, **2009**.

161. Gallivan, M. A.; Noble, D. R.; Georgiadis, J. G.; Buckius, R. O. An evaluation of the bounce-back boundary condition for lattice Boltzmann simulations. *Int. J. Numer. Meth. Fluids* **1997**, *25*, 249-263.

162. Qian, Y. H.; d'Humières, D.; Lallemand, P. Lattice BGK Models for Navier-Stokes Equations. *Europhys. Lett.* **1992**, *17*, 479-484.

163. Capuani, F.; Pagonabarraga, I.; Frenkel, D. Discrete solution of the electrokinetic equations. *J. Chem. Phys.* **2004**, *121*, 973-986.

164. Bennett, J. E. Electrodes for generation of hydrogen and oxygen from seawater. *Int. J. Hydrogen Energy* **1980**, *5*, 401-408.

165. Carraway, E. R.; Demas, J. N.; DeGraff, B. A.; Bacon, J. R. Photophysics and photochemistry of oxygen sensors based on luminescent transition-metal complexes. *Anal. Chem.* **1991**, *63*, 337-342.

166. Kamholz, A. E.; Yager, P. Theoretical analysis of molecular diffusion in pressure-driven laminar flow in microfluidic channels. *Biophys. J.* **2001**, *80*, 155-160.

167. Bruus, H. *Theoretical Microfluidics*. Oxford University Press: USA, **2007**.

168. Kwak, R.; Kim, S. J.; Han, J. Continuous-Flow Biomolecule and Cell Concentrator by Ion Concentration Polarization. *Anal. Chem.* **2011**, *83*, 7348-7355.

169. Jeon, H.; Lee, H.; Kang Kwan, H.; Lim, G. Ion concentration polarization-based continuous separation device using electrical repulsion in the depletion region. *Sci. Rep.* **2013**, *3*, 3483.

170. Phan, D.-T.; Chun, Y.; Nguyen, N.-T. A continuous-flow droplet-based concentrator using ion concentration polarization. *RSC Adv.* **2015**, *5*, 44336-44341.

171. Knust, K. N.; Hlushkou, D.; Tallarek, U.; Crooks, R. M. Electrochemical Desalination for a Sustainable Water Future. *ChemElectroChem* **2014**, *1*, 850-857.

172. Amatore, C.; Belotti, M.; Chen, Y.; Roy, E.; Sella, C.; Thouin, L. Using electrochemical coupling between parallel microbands for in situ monitoring of flow rates in microfluidic channels. *J. Electroanal. Chem.* **2004**, *573*, 333-343.

173. Anderson, M. J.; Crooks, R. M. High-Efficiency Generation-Collection Microelectrochemical Platform for Interrogating Electroactive Thin Films. *Anal. Chem.* **2014**, *86*, 9962-9969.

174. Mani, A.; Bazant, M. Z. Deionization shocks in microstructures. *Phys. Rev. E Stat., Nonlinear, Soft Matter Phys.* **2011**, *84*, 061504.

175. Kinoshita, K.; Ferrier, D. R.; Stonehart, P. Effect of electrolyte environment and platinum crystallite size on hydrogen adsorption. V. *Electrochim. Acta* **1978**, *23*, 45-54.

176. Clavilier, J. The role of anion on the electrochemical behavior of a {111} platinum surface; an unusual splitting of the voltammogram in the hydrogen region. *J. Electroanal. Chem. Interfacial Electrochem.* **1980**, *107*, 211-216.

177. Conway, B. E.; Ping, G. Surface electrochemistry of the anodic chlorine evolution reaction at platinum. Influence of codeposition of surface oxide species on adsorption of the chlorine radical intermediate. *J. Chem. Soc., Faraday Trans.* **1990**, *86*, 923-930.

178. *Solubility of Selected Gases in Water*, 93rd ed.; CRC Handbook of Chemistry and Physics, ed. W.M. Haynes. CRC Press: USA, **2012**.

179. Wang, T. X.; Margerum, D. W. Kinetics of Reversible Chlorine Hydrolysis: Temperature Dependence and General-Acid/Base-Assisted Mechanisms. *Inorg. Chem.* **1994**, *33*, 1050-1055.

180. Amatore, C.; Da Mota, N.; Sella, C.; Thouin, L. Theory and Experiments of Transport at Channel Microband Electrodes under Laminar Flows. 1. Steady-State Regimes at a Single Electrode. *Anal. Chem.* **2007**, *79*, 8502-8510.

181. Debiemme-Chouvy, C.; Hua, Y.; Hui, F.; Duval, J. L.; Festy, D.; Cachet, H. Electrochemical treatments using tin oxide anode to prevent biofouling. *Electrochim. Acta* **2011**, *56*, 10364-10370.

182. Al Mamun, N. H.; Dutta, P. Patterning of platinum microelectrodes in polymeric microfluidic chips. *J. Microlithogr., Microfabr., Microsyst.* **2006**, *5*, 039701.

183. Zhou, B.; Jiang, X.; liu, Z.; Shen, R.; Rogachev, A. V. Preparation and characterization of TiO2 thin film by thermal oxidation of sputtered Ti film. *Mater. Sci. Semicond. Process.* **2013**, *16*, 513-519.

184. Ghicov, A.; Tsuchiya, H.; Macak, J. M.; Schmuki, P. Annealing effects on the photoresponse of TiO2 nanotubes. *Phys. Status Solidi A* **2006**, *203*, R28-R30.

185. Wu, Q.; Li, D.; Hou, Y.; Wu, L.; Fu, X.; Wang, X. Study of relationship between surface transient photoconductivity and liquid-phase photocatalytic activity of titanium dioxide. *Mater. Chem. Phys.* **2007**, *102*, 53-59.

186. Shang, T.; Teng, E.; Woolley, A. T.; Mazzeo, B. A.; Schultz, S. M.; Hawkins, A. R. Contactless conductivity

detection of small ions in a surface micro-machined CE chip. *Electrophoresis* **2010**, *31*, 2596-2601.

187. Linsebigler, A. L.; Lu, G.; Yates, J. T., Jr. Photocatalysis on TiO2 Surfaces: Principles, Mechanisms, and Selected Results. *Chem. Rev.* **1995**, *95*, 735-758.

188. Fujishima, A.; Honda, K. Electrochemical photolysis of water at a semiconductor electrode. *Nature* **1972**, *238*, 37-38.

189. Frank, S. N.; Bard, A. J. Semiconductor electrodes. 12. Photoassisted oxidations and photoelectrosynthesis at polycrystalline titanium dioxide electrodes. *J. Am. Chem. Soc.* **1977**, *99*, 4667-4675.

190. Fujishima, A.; Inoue, T.; Honda, K. Competitive photoelectrochemical oxidation of reducing agents at the titanium dioxide photoanode. *J. Am. Chem. Soc.* **1979**, *101*, 5582-5588.

191. Bard, A. J. Photoelectrochemistry. *Science* **1980**, *207*, 139-144.

192. Frank, S. N.; Bard, A. J. Semiconductor Electrodes. 12. Photoassisted Oxidations and Photoelectrosynthesis at Polycrystalline TiO_2 Electrodes. *J. Am. Chem. Soc.* **1977**, *99*, 4667-4675.

193. Gai, L.; Mack, J.; Liu, H.; Xu, Z.; Lu, H.; Li, Z. A BODIPY fluorescent probe with selective response for hypochlorous acid and its application in cell imaging. *Sens. Actuators, B* **2013**, *182*, 1-6.

194. Coltro, W. K. T.; Lima, R. S.; Segato, T. P.; Carrilho, E.; Pereira de Jesus, D.; Lucio do Lago, C.; Fracassi da Silva, J. A. Capacitively coupled contactless conductivity detection on microfluidic systems. Ten years of development. *Anal. Methods* **2012**, *4*, 25-33.

195. Brito-Neto, J. G. A.; Fracassi da Silva, J. A.; Blanes, L.; Lucio do Lago, C. Understanding capacitively coupled contactless conductivity detection in capillary and microchip electrophoresis. Part 1. Fundamentals. *Electroanalysis* **2005**, *17*, 1198-1206.

196. Coltro, W. K. T.; Neves, R. d. S.; Motheo, A. d. J.; Fracassi da Silva, J. A.; Carrilho, E. Microfluidic devices with integrated dual-capacitively coupled contactless conductivity detection to monitor binding events in real time. *Sens. Actuators, B* **2014**, *192*, 239-246.

197. Emaminejad, S.; Javanmard, M.; Dutton, R. W.; Davis, R. W. Microfluidic diagnostic tool for the developing world: contactless impedance flow cytometry. *Lab Chip* **2012**, *12*, 4499-4507.

198. Barhoumi, H.; Maaref, A.; Jaffrezic-Renault, N. Experimental Study of Thermodynamic Surface Characteristics and pH Sensitivity of Silicon Dioxide and Silicon Nitride. *Langmuir* **2010**, *26*, 7165-7173.

199. Guan, W.; Rajan, N. K.; Duan, X.; Reed, M. A. Quantitative probing of surface charges at dielectric-electrolyte interfaces. *Lab Chip* **2013**, *13*, 1431-1436.

200. Choi, D.-J.; You, S.-J.; Kim, J.-G. Development of an environmentally safe corrosion, scale, and microorganism inhibitor for open recirculating cooling systems. *Mater. Sci. Eng. A* **2002**, *335*, 228-235.